Guide to Using

EFrac3D

A Simulation Tool for Designing and Optimizing Energized Fracturing Treatments

License Information

This software documentation is provided for internal use only at **The University of Texas at Austin**. The license is non-exclusive, non-sublicensable, non-transferable and non-assignable.

Table of Contents

Section 1 – User Manual

CHAPTER 1: WHAT IS EFRAC3D 7

1.1 ABOUT THIS VERSION 8
1.2 CURRENT CAPABILITES 8
1.3 WHAT TO READ 8

CHAPTER 2: INSTALLING EFRAC3D 10

2.1 INSTALLATION 11
2.2 FOLDER STRUCTURE AND PERSISTENCE 11

CHAPTER 3: WORKING SCHEME OF EFRAC3D 15

3.1 LINK BETWEEN INTERFACE AND ENGINE 16

CHAPTER 4: INPUTS 18

4.1 MAIN 19
4.1.1 Geological Properties 19
4.1.1.1 Configuration 20
4.1.1.2 Layer Properties 20
4.1.2 Pumping Schedule 22
4.1.2.1 Pumping Configuration 22
4.1.2.2 Pumping Stages 23
4.1.3 Fluid and Proppant Properties for Pumping Stage: 31
4.1.4 Reservoir 32
4.1.4.1 Grid 33
4.1.4.2 Properties 34
4.1.4.3 Fractional Flow Curve 35
4.1.4.4 Flowback 35
4.1.4.5 Shut In 36
4.2 WELLBORE 36
4.2.1 Dimensions 37
4.2.2 Perforations 38
4.2.3 Thermal Properties 39
4.3 SIMULATOR SETTINGS 39

CHAPTER 5: SAVING AND LOADING DATA – FILE MENU 43

5.1 SAVING AND LOADING DATA – FILE MENU 44

CHAPTER 6: RUNNING EFRAC3D & VIEWING RESULTS 46

6.1 WELLBORE 47
6.2 FRACTURE PROPAGATION 50
6.3 PRODUCTIVITY RESULTS 53
6.4 FRACTURE CONTOUR PLOT 56
6.5 INVASION RESERVOIR PLOT 60
6.6 PRODUCTIVITY CALCULATIONS PLOT 61

CHAPTER 7: TROUBLE SHOOTING – STRANGE RESULTS 65

Section 2 – Technical Documentation

CHAPTER 1: INTRODUCTION 67

1.1 BACKGROUND 68
1.2 EFRAC3D SIMULATOR 68

CHAPTER 2: 3D COMPOSITIONAL FRACTURE MODEL 69

2.1 PROBLEM STATEMENT 70
2.1.1 Fracture Geometry 70
2.1.2 Main Variables for Fluid and Proppant 70
2.1.3 Material Balances 72
2.1.3 Main Variables for Fluid Composition 72
2.2 FLOW EQUATIONS 73
2.2.1 Slurry Flow 73
2.2.2 Proppant Flow 76
2.2.3 Fluid Flow 77
2.3 PRESSURE EQUATION (OVERALL MASS BALANCE) 78
2.4 PROPPANT TRANSPORT EQUATION 80
2.4 COMPONENT TRANSPORT EQUATION 82
2.4.1 Component Mass Fraction Formulation 82
2.4.2 Overall Component Mass Fraction Formulation 84
2.4.3 Saturation Formulation 84
2.5 ENERGY BALANCE EQUATION 86
2.5.1 Assumptions 86
2.5.2 Combined Energy Fluxes 86
2.5.3 Heat Lost due to Leak-Off 87
2.5.4 Heat Gained from the Reservoir 88
2.5.5 Energy Balance Equation 89
2.6 FRACTURE MECHANICS 90

2.6.1 Fracture Opening Equation 90
2.6.2 Criterion for Fracture Propagation 91
2.7 Overview of the Mathematical Problem 92
2.7.1 Completeness of the Mathematical Problem 92
2.7.2 Complexity of the Mathematical Problem 93
2.7.2.1 Different Classes of PDEs 93
2.7.2.2 Strong Coupling between the PDEs 94
2.7.2.3 Non Linearity 94
2.7.2.4 Moving - Boundary Problem 94
2.7.2.5 Singularities 95
Nomenclature 99
References 102

CHAPTER 3: FINITE ELEMENT FORMULATION AND SOLUTION ALGORITHM 106

3.1 Solution of the Pressure Equation 107
3.2 Solution of the Compatibility Equation 112
3.3 Solution of the Convection-Dominated Equations 113
3.4 Solution of the Pressure Opening Equation 116
3.5 Main Algorithm 117
3.5.1 Overview of the Main Algorithm 117
3.5.2 Fracture Propagation 118
3.5.3 Adaptive Fracture Front Displacement 119
3.5.4 Time Decoupling Scheme 119
3.5.5 Relaxation Process 120
3.5.6 Linear Solvers 120
3.6 Main Features of the Dynamic Unstructured Mesh 121
3.6.1 Past Developments 121
3.6.2 Mesh Structure 121
3.6.3 Elements and Shape Functions 122
3.6.4 Boundary Node Generation 123
3.6.5 Interior Node Generation 124
Nomenclature 132
References 134

CHAPTER 4: WELLBORE AND PRODUCTIVITY MODELS 135

4.1 Temperature Variation in the Wellbore 136
4.1.1 Definition and Formulation of Heat Exchanges 136
4.1.2 Energy Balance Equation along the Wellbore 138
4.2 Pressure Variation in the Wellbore 139
4.2.1 Frictional Loss 139
4.3 Near-Wellbore Frictional Loss 141
4.3.1 Perforation Frictional Loss 141

4.3.2 Tortuosity Effects 142
4.4 Interpolation Scheme between Fracture and Reservoir 143
4.4.1 Algorithm for Interpolation 143
4.4.2 Barycentric Method 144
4.5 Productivity Model for Fractured Well 145
4.5.1 Formulation of the Productivity Model 145
4.5.2 Properties of the Virgin Zone, Invaded Zone and Fracture 148
4.5.3 Determination of the Invaded Zone Length 149
4.5.4 Comments Regarding Foams 151
References 159

CHAPTER 5: PHASE BEHAVIOR, RHEOLOGY AND LEAK-OFF OF ENERGIZED FLUIDS 161

5.1 Phase Density 162
5.2 Component Solubility 163
5.3 Rheology 164
5.3.1 Base Fluid Rheology 164
5.3.2 Foam Rheology 165
5.4 Multi-Phase Leak-off Coefficients 167
5.4.1 Field Determination 168
5.4.2 Experimental Determination 169
5.4.3 Conclusions from In-House Experiments 169
References 172

CHAPTER 6: DESIGN RECOMMENDATIONS 173

CHAPTER 1: WHAT IS EFRAC3D

1.1 ABOUT THIS VERSION

EFrac3D is a PC-based simulator for designing and optimizing energized fracturing treatments. EFrac3D is developed at the University of Texas at Austin.

1.2 CURRENT CAPABILITES

The combination of the fracture, productivity, and wellbore models forms a standalone modeling tool to design and optimize energized treatments. The simulator includes the following capabilities:

1. The model allows for multi-phase, multi-component, compressible fluid flow both in the fracture and in the wellbore.
2. The model predicts variations in temperature, pressure, and fluid composition.
3. The fracture can propagate across multiple layers, where height growth is controlled by the vertical distribution of the minimum horizontal stress.
4. The model is suitable for any well configuration: vertical, deviated, or horizontal.
5. The fracture model is connected to a productivity model. The model accounts for: (i) two-phase fluid flow, (ii) damage in the invaded zone, (iii) finite fracture conductivity, (iv) mechanical skin, and (v) changes in fluid composition.
6. The model is suitable for many different applications ranging from hydraulic fracturing to long-term injections for enhanced oil recovery, well clean-up, or carbon sequestration purposes.

1.3 WHAT TO READ

This manual, which focuses on the effective use of EFrac3D, is organized as follows:

Section 1: User Guide

Section 1 is the user guide that describes how to run EFrac3D. The user guide assumes that you have a general knowledge of the Windows operating system.

- Chapter 2 covers the installation of EFrac3D
- Chapter 3 describes the general working scheme of the simulator.
- Chapter 4 covers the common input variables.
- Chapter 5 explains how to load and save data.

- Chapter 6 describes the outputs and results displayed by the simulator.
- Chapter 7 discusses common errors for troubleshooting and debugging purposes.

Section 2: Technical Documentation

Section 2 is the description of the mathematical models that are used in the simulator

- Chapter 2 covers the formulation of the 3D fracture model
- Chapter 3 presents the main algorithm and the finite element equations implemented in the model.
- Chapter 4 describes the wellbore and productivity models
- Chapter 5 covers the characterization of properties of energized fluids
- Chapter 6 discusses the design recommendation for energized fracturing treatments.

For a description of the underlying mathematical models, one can also refer to the references that are given at the end of each Chapter. In particular, the reader may refer to Ribeiro (2013) for a more comprehensive description of the model.

Key Reference:

Ribeiro, L.H. and Sharma, M.M 2013. A New 3D Compositional Model for Hydraulic Fracturing with Energized Fluids. *SPE Prod & Oper* **28**(3): 259-267. SPE 159812-PA.

CHAPTER 2: INSTALLING EFRAC3D

2.1 INSTALLATION

Requirements

These are the minimum system requirements for EFrac3D.

Platform	Minimum Version
Microsoft Windows	Windows Vista

A DirectX 9 capable graphics card is recommended for viewing plots.
EFrac3D is a 32 bit application that runs on 32 bit and 64 bit environments.

To install EFrac3D, locate the product installer that you've downloaded or received. The installer will have a name like UTEFrac3DSetup_<version>.exe. Double click this file to start the installation process. Follow the onscreen prompts to complete the installation. You will **not** have the option to change the install location, nor will you have the option to include/exclude options. Once the installer completes, you can start UTEFrac3D by clicking Start, clicking All Programs click The University of Texas at Austin, click UTEFrac3D then click the UTEFrac3D icon.

When you run EFrac3D for the first time, the application will perform an initial setup automatically:

1) It will create a folder beneath My Documents, called UTEFrac3D, which will be populated with default settings, libraries and sample files.
    a. Libraries are pre-built Proppant Types and Fluid Types.
    b. Sample files include 18 pre-build projects, with results.
    c. Settings are pre-configured Simulator settings.

2) It will install a required DirectX 9 support library called SlimDX.

2.2 FOLDER STRUCTURE AND PERSISTENCE

During the installation process, sample files are written to the install directory beneath the *SampleProjects* folder. These files are then copied to a user specific folder upon first run of UTEFrac3D.

Each user of EFrac3D on a PC will have his/her own settings, libraries and data files. Upon first run of EFrac3D by a user, the folder structure required for correct operation of EFrac3D will be created automatically, and populated with default settings, libraries and sample data files, which are copied during the install process, as noted above.

UTEFrac3D creates its default folder structure beneath each users My Documents folder as such:

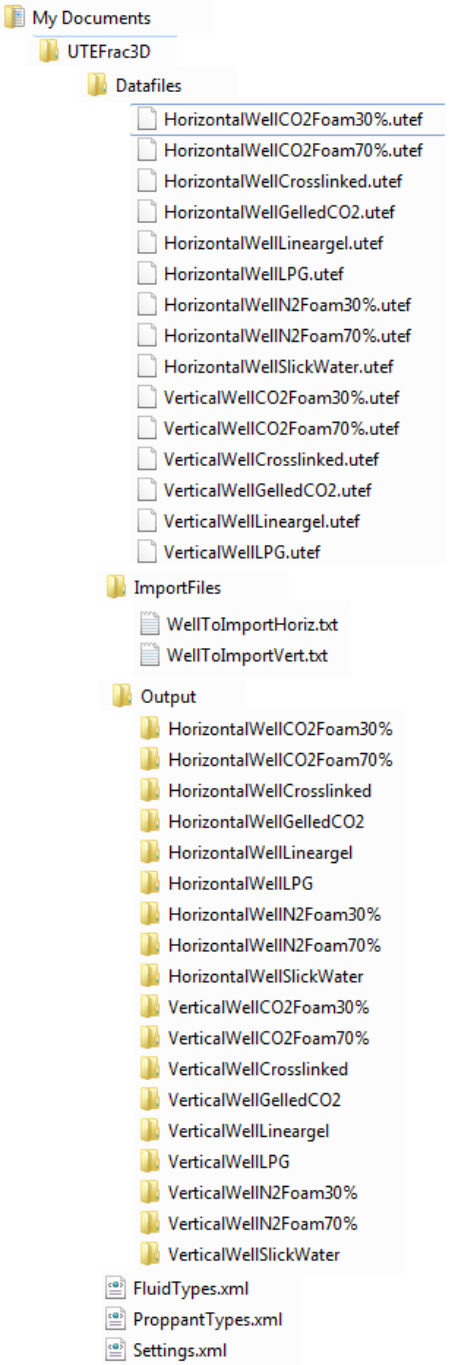
My Documents
UTEFrac3D
Datafiles
HorizontalWellCO2Foam30%.utef
HorizontalWellCO2Foam70%.utef
HorizontalWellCrosslinked.utef
HorizontalWellGelledCO2.utef
HorizontalWellLineargel.utef
HorizontalWellLPG.utef
HorizontalWellN2Foam30%.utef
HorizontalWellN2Foam70%.utef
HorizontalWellSlickWater.utef
VerticalWellCO2Foam30%.utef
VerticalWellCO2Foam70%.utef
VerticalWellCrosslinked.utef
VerticalWellGelledCO2.utef
VerticalWellLineargel.utef
VerticalWellLPG.utef
ImportFiles
WellToImportHoriz.txt
WellToImportVert.txt
Output
HorizontalWellCO2Foam30%
HorizontalWellCO2Foam70%
HorizontalWellCrosslinked
HorizontalWellGelledCO2
HorizontalWellLineargel
HorizontalWellLPG
HorizontalWellN2Foam30%
HorizontalWellN2Foam70%
HorizontalWellSlickWater
VerticalWellCO2Foam30%
VerticalWellCO2Foam70%
VerticalWellCrosslinked
VerticalWellGelledCO2
VerticalWellLineargel
VerticalWellLPG
VerticalWellN2Foam30%
VerticalWellN2Foam70%
VerticalWellSlickWater
FluidTypes.xml
ProppantTypes.xml
Settings.xml

Project data files can be saved to any location that the user has read/write rights to, however, the location where simulation result files are saved is not user selectable. Output files (.dat and .plt files) are always written to My Documents\UTEFrac3D\Output***projectFileName***, therefore, you should avoid duplicating project file names.

CHAPTER 3: WORKING SCHEME OF EFRAC3D

3.1 LINK BETWEEN INTERFACE AND ENGINE

EFrac3D refers to the combination of the simulator engine and the interface. The engine performs the simulations in the background. Its execution is commanded by the interface. The interface contains both the inputs of the program and the outputs of the simulation.

The interactions between the engine and the graphic user interface may be described as follows:

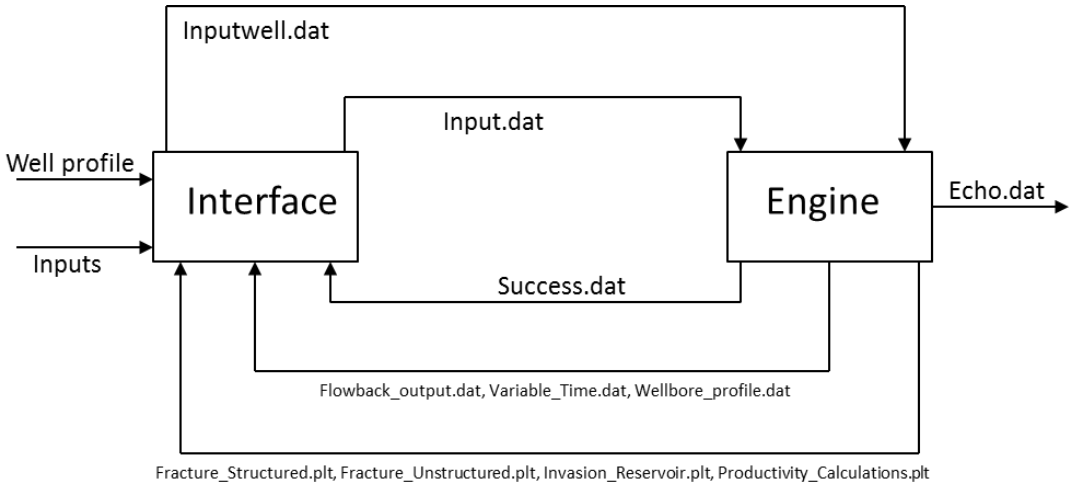

A complete simulation consists of the following steps:

1. The user uploads the well profile in the interface.
2. The user enters the various input properties through the interface.
3. The user clicks on *Run*.
4. The interface generates automatically two data files (*input.dat* and *inputwell.dat*).
5. The interface starts the engine.
6. The engine reads the inputs contained in the two input files.
7. The engine performs the simulations over time. The main outputs are displayed on the console over time. The simulation stops when the maximum pumping time is reached. The engine generates multiple output files over time.

8. At the end of the simulation, the interface reads the output files and displays the information in several charts, tables, and contour plots.

The output files generated by the engine may be viewed directly by the user:

a. Fracture_Structured.plt, Fracture_Unstructured.plt, Invasion_Reservoir.plt and Productivity_Calculations.plt can be read with TecPlot to generate contour maps over time.
b. Variable_Time.dat, Wellbore_profile.dat, and Flowback_Output.dat can be opened in MS Excel or Matlab to generate different x-y plots and tables.
c. Echo.dat is a basic data file that contains all the inputs chosen by the user. This file enables the user to double check that the engine is actually reading correctly all the values he inputted.
d. Success.dat is a basic data file generated by the engine to confirm the success of the simulation. This file contains useful information for debugging purposes.

Similarly, the input files may be generated directly by the user, i.e., without using the interface. Both the input and output files may be opened in text editors (such as Notepad).

CHAPTER 4: INPUTS

The EFrac3D input frame is organized into three tabs: (1) Main (2) Wellbore (3) Simulator Settings.

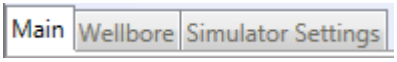

4.1 MAIN

The 'Main' input tab includes four sections: (1) Geological Properties (2) Pumping Schedule (3) Fluid and Proproppant Properties for a given Pumping Stage, and (4) Reservoir.

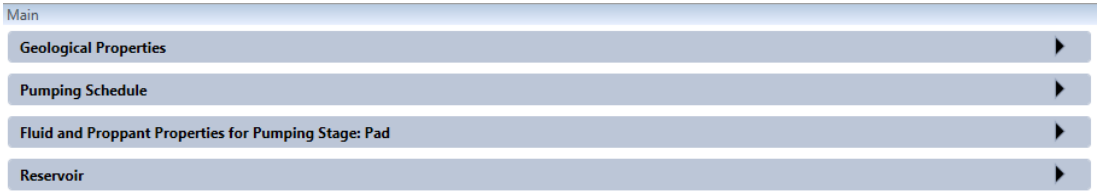

Each of them is described below.

4.1.1 Geological Properties

This section defines the reservoir layers for fracture propagation purposes. It includes the depth of the reservoir layers, the vertical distribution of the *in-situ* stress distribution, the mechanical properties of each layer, the multi-phase leak-off properties in each layer, and the length and location of the perforated interval.

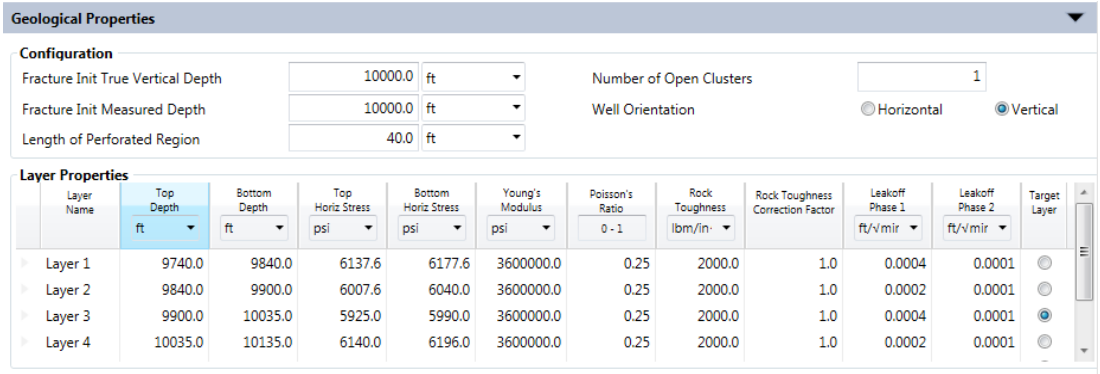

4.1.1.1 Configuration

The program allows simulations for both vertical and horizontal well orientations.

Fracture Initiation True Vertical Depth

It is the vertical depth at which the user wants to initiate the fracture. This depth corresponds to the middle of the perforated interval. Units: m or ft. 1 ft = 0.3048 m.

Fracture Initiation Measured Depth

It is the measured depth along the well at which the user wants to initiate the fracture. The measured depth will be greater than the true vertical depth for horizontal wells. The measured depth will be equal to the true vertical depth for vertical wells. Units: m or ft. 1 ft = 0.3048 m.

Length of Perforated Region

It is the length of the perforated interval (or open-hole interval) along the wellbore. Units: m or ft. 1 ft = 0.3048 m.

Number of Open Clusters

It is the number of clusters along the wellbore that are open for fracture propagation. For horizontal wells, number of open clusters is more than 1. For vertical wells, the number of open clusters is normally 1.

4.1.1.2 Layer Properties

The user can add multiple layers and the corresponding layer properties such as depth at the top and bottom of the layer, horizontal stress at the top and bottom of the layer, Young's Modulus, Poisson's Ratio, Rock Toughness and Correction Factor, Leak-off coefficients of the phases present. The appropriate unit for each of the properties can be selected from the drop down menu.

Top Depth

It is the depth at which the layer starts. Units: m or ft. 1 ft = 0.3048 m.

Bottom Depth

It is the depth at which the layer ends. Units: m or ft. 1 ft = 0.3048 m.

Top Horizontal Stress
It is the horizontal stress at the top of the layer. Units: psi or Pa. 1 psi = 6894.7572932 Pa.

Bottom Horizontal Stress
It is the horizontal stress at the bottom of the layer. Units: psi or Pa. 1 psi = 6894.7572932 Pa.

Young's Modulus
It is the Young's Modulus in that particular layer. Units: psi or Pa. 1 psi = 6894.7572932 Pa.

Poisson's Ratio
It is the Poisson's Ratio in that particular layer. Range: 0-1

Rock Toughness
It is the Rock Toughness in that particular layer. Units: $lb/in^{1.5}$ or $kg/cm^{1.5}$. 1 $lb/in^{1.5}$ = 0.112051 $kg/cm^{1.5}$

Rock Toughness Correction Factor
It is the Rock Toughness Correction Factor in that particular layer.

Leakoff Phase 1
It is the Leakoff coefficient of phase 1 in that particular layer. Phase 1 usually denotes for the base fluid. Units: ft/√min or m/√min. 1 ft/√min = 0.3048 m/√min.

Leakoff Phase 2
It is the Leakoff coefficient of phase 2 in that particular layer. If the fluid used for fracturing has only one phase then its value is 0. Units: ft/√min or m/√min. 1 ft/√min = 0.3048 m/√min.

Target Layer
It is the layer in which we are going to initiate the fracture.

4.1.2 Pumping Schedule

This section defines the desired pumping schedule over time. For each pumping stage, it contains the stage duration, injection rate, proppant loading, fluid type, and proppant type.

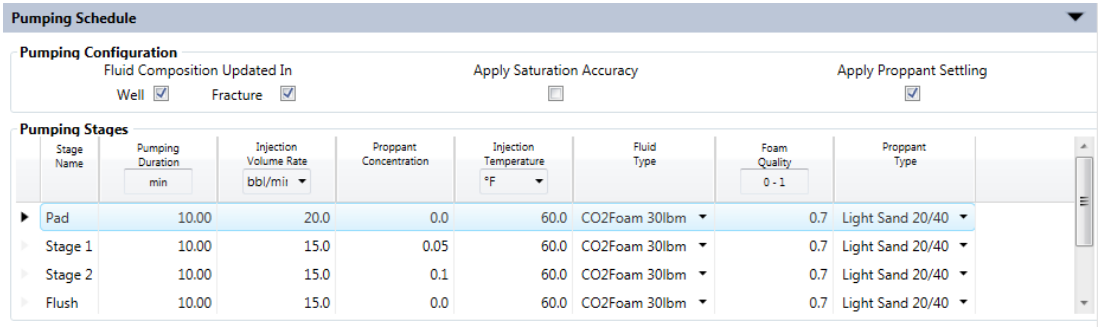

4.1.2.1 Pumping Configuration

The user has the flexibility of selecting various options.

Fluid Composition
The user may tick on the box if he/she wishes to update the composition of the fluids in the well and/or fracture.

Saturation Accuracy
This option is useful only for two-phase fluid mixtures. When this option is selected, the full component balances equations are solved in order to obtain the fluid saturation. If this option is not selected, an averaged formulation of the component balance is used to estimate the fluid saturation. This second option improves the code stability.

Proppant Settling
The user may tick on the box if he/she wishes to apply proppant settling while solving.

4.1.2.2 Pumping Stages

The first stage is usually the pad (without any proppant loading) and is followed by subsequent stages where proppant is injected. The last stage is called the flush, which basically ensures that there is no proppant left in the wellbore and all the proppant injected is in the fracture.

Pumping Duration
It is the duration of the pumping stage. Units: min.

Injection Volume Rate
It is the volumetric injection rate in that pumping stage. Units: bbl/min or m^3/min. 1 bbl/min = 0.1589873 m^3/min.

Proppant Concentration
It is the ratio of the volume of proppant injected in that particular stage to the volume of fluid injected or in other words it is the volumetric proppant concentration.

Injection Temperature
It is the temperature of the fluid injected in that particular stage. Units: ^oF or ^oC.

Foam Quality
It is the foam quality of the fluid injected in that particular stage. If a pure fluid is used then foam quality is taken as 0. Range: 0-1.

Fluid and Proppant Type
The user has various options to choose from the drop down menu.

The fluid type options available are:

a. Slick Water
b. Linear Gel 30lbm
c. X-Linked Gel 30lbm
d. CO_2Foam 30lbm 0.3Quality
e. CO_2Foam 30lbm 0.7Quality
f. N_2Foam 30lbm 0.3Quality
g. N_2Foam 30lbm 0.7Quality
h. CO_2Gelled 30lbm

i. LPG Gelled 30lbm
j. Nitrogen

The proppant type options available are:

a. Light Sand 20/40
b. Light Sand 40/70
c. Sand 20/40
d. Sand 40/70
e. UltraLight Sand 20/40
f. UltraLight Sand 40/70

If the user wishes to use fluids or proppants other than those listed above or if the user would like to modify/edit some of the values in the existing libraries, then it can be done easily in the following way:

In the menu bar, go to Tools and then select Libraries which has two options namely Fluid Types and Proppant Types. Now if the user wants to create a new fluid or proppant type click on New and enter all the values. If the user wants to modify some value than click on that fluid or proppant type and make all the necessary changes and then click Apply at the bottom

Fluid Type Library
The properties required for the fluid type are polymer loading, fluid phase properties, fluid component properties, mass fractions and viscosity in wellbore and fracture.

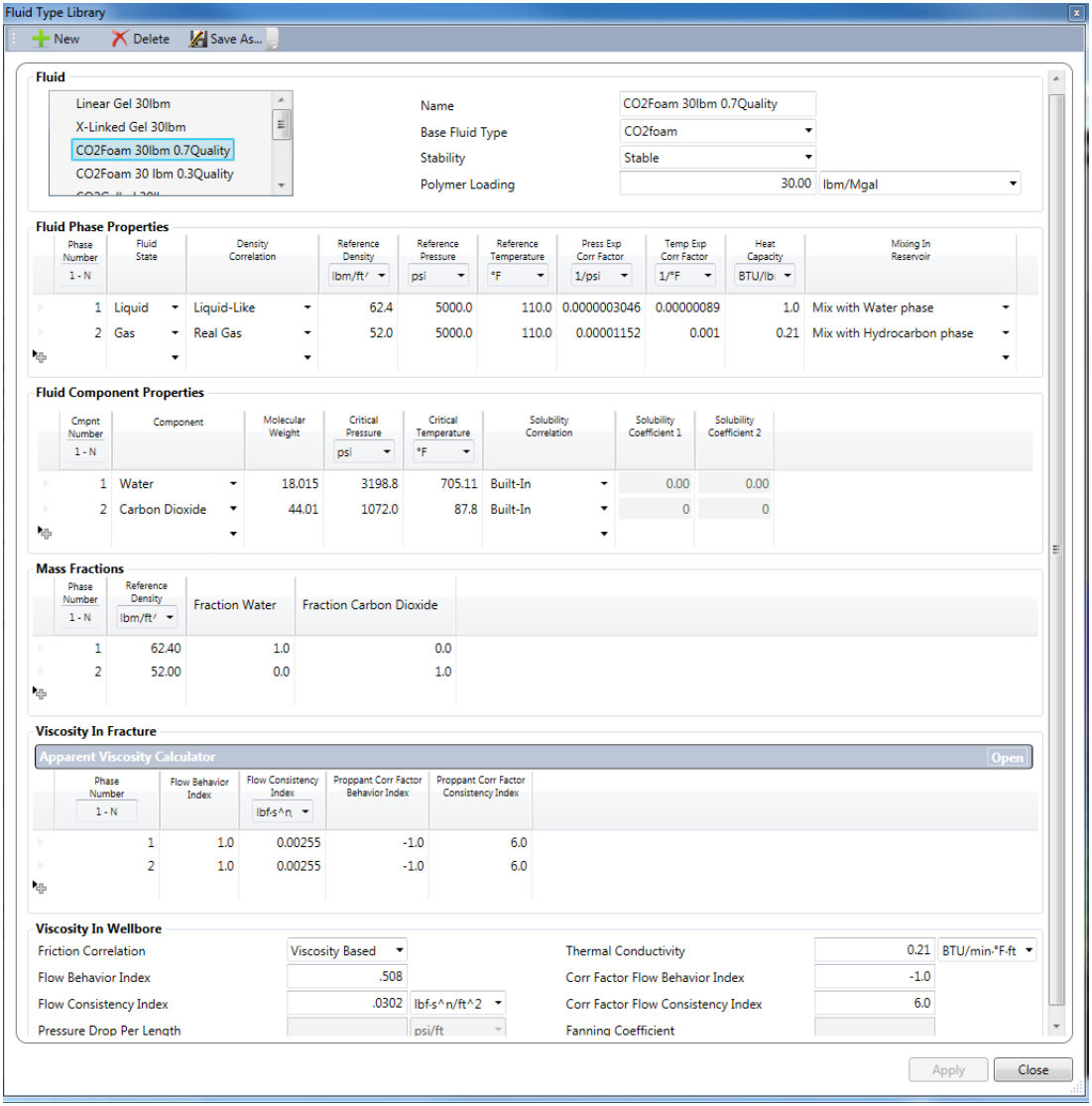

Name

It is the name that will appear in the drop-down menu.

Base Fluid Type

For example, for slick water, linear gelled and cross linked, base fluid type will be water.

Stability
If the fluid type is of foam type, then user has an option to have it as stable foam or unstable foam. However, it is recommended to run the simulator using stable foams.

Polymer Loading
It is the ratio of the amount of polymer added to the volume of fluid injected. Units: lbm/Mgal or kg/1000L. 1 lbm/Mgal = 0.119826 kg/1000L.

Fluid Phase Properties
This subsection contains properties of the entire fluid phase. The properties required here are as follows:

Phase Number
If the fluid is made up of only phase it will have "1" and if it has an additional phase than it will have "2".

Fluid State
Select the appropriate fluid state as "Gas" or "Liquid: from the drop down menu for that corresponding phase.

Density Correlation
If the fluid state is liquid, then select "Liquid-Like" from the drop down menu and if the fluid state is gas then select "Real Gas".

Reference Density
It is the density of the fluid at some reference temperature and pressure. Please refer to the inbuilt libraries for the values of reference density of various fluids. Units: lbm/ft^3 or kg/m^3. 1 lbm/ft^3 = 16.0185 kg/m^3.

Reference Pressure
Please refer to the inbuilt libraries for the values of reference pressure of various fluids. Units: psi or Pa. 1 psi = 6894.7572932 Pa.

Reference Temperature
Please refer to the inbuilt libraries for the values of reference temperature of various fluids. Units: ^oF or ^oC.

Pressure Exponential Correction Factor
It is the factor introduced to correct for pressures different from the reference pressure. Please refer to Equation 5.1 in Technical Documentation. Units: 1/psi or 1/Pa

Temperature Exponential Correction Factor
It is the factor introduced to correct for temperatures different from the reference temperature. Please refer to Equation 5.1 in Technical Documentation. Units: $1/^{o}F$ or $1/^{o}C$

Heat Capacity
It is the average value of the heat capacity. Units: BTU/lbm.^{o}F or J/kg.^{o}K. 1 BTU/lbm.^{o}F = 4186.8 J/kg.^{o}K.

Mixing in Reservoir
If the fluid is water based, then select that it mixes with water phase in the reservoir. If the fluid is hydrocarbon or CO_2 or N_2, then select that it mixes with the hydrocarbon phase.

Fluid Component Properties
This subsection contains properties of the components that are present in the fluid. The properties required here are as follows:

Component Number
If the fluid is made up of only one component it will have "1" and if it has an additional component than it will have "2" and so on.

Component
Please select the name of the component from the drop down menu.

Molecular Weight
It is the molecular weight of the corresponding component.

Critical Pressure
It is the critical pressure of the corresponding component. Units: psi or Pa. 1 psi = 6894.7572932 Pa.

Critical Temperature
It is the critical temperature of the corresponding component. Units: ^{o}F or ^{o}C.

Solubility Correlation
If the user wants to use built in solubility correlation that select that option from the drop down menu and there is no need to fill the solubility coefficients of 1 and 2. If the user selects Langmuir type solubility correlation, than he/she will have to enter the solubility coefficients 1 and 2.

Solubility Coefficient 1 and 2
These columns are activated only if the user selects Langmuir type solubility correlation. The solubility coefficient of the components has to be entered by the user.

Mass Fractions
This subsection contains mass fractions of the components that are present in the fluid phases. The properties required here are as follows:

Phase Number
If the fluid is made up of only phase it will have "1" and if it has an additional phase than it will have "2".

Reference Density
It is the density of the fluid at some reference temperature and pressure. Please refer to the inbuilt libraries for the values of reference density of various fluids. Units: lbm/ft^3 or kg/m^3. 1 lbm/ft^3 = 16.0185 kg/m^3.

Fraction "Component Name"
Based on the component name selected previously, the user needs to enter the mass fraction of the component in that corresponding phase. In the built in libraries, mass fractions have been entered as 1 for the component that is mainly making up that phase and 0 if the component is present in minor quantities. This is because the code calculates the exact values of the mass fractions based on the solubility correlation.

Viscosity in Fracture
This subsection contains viscosity properties of the phases that are present in the fluid. The properties required here are as follows:

Phase Number
If the fluid is made up of only phase it will have "1" and if it has an additional phase than it will have "2".

Flow Behavior Index

Flow Consistency Index

Proppant Correction Factor to Behavior Index

Proppant Correction Factor to Consistency Index

Please refer to the Equation 5.8 in Technical Documentation for the governing equations.

In order to confirm that the viscosity value obtained by the above viscosity parameters is reasonable, we have an inbuilt apparent viscosity calculator which can be opened by clicking on Open as shown below:



The inputs required for apparent viscosity calculator are the proppant volume fraction in the fracture and the shear rate (s^{-1}) and we get the apparent viscosity (cP or Pa.s.) as shown below:

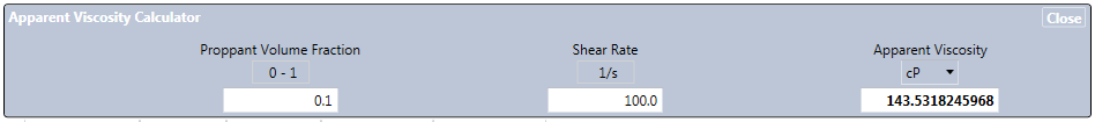

Also it allows the user to see the effect of proppant volume fraction on the apparent viscosity.

Viscosity in Wellbore
This subsection contains viscosity properties for the wellbore. The properties required here are as follows:

Friction Correlation

There are three options available in the drop down menu for predicting Pressure drop in the wellbore. They are as follows:

a. Using Pressure Drop Per Unit length (psi/ft or Pa/m)
b. Using Fanning Coefficient (f)
c. Using Viscosity Parameters

Proppant Type Library

The properties required are density, diameter of the proppant particle and heat capacity.

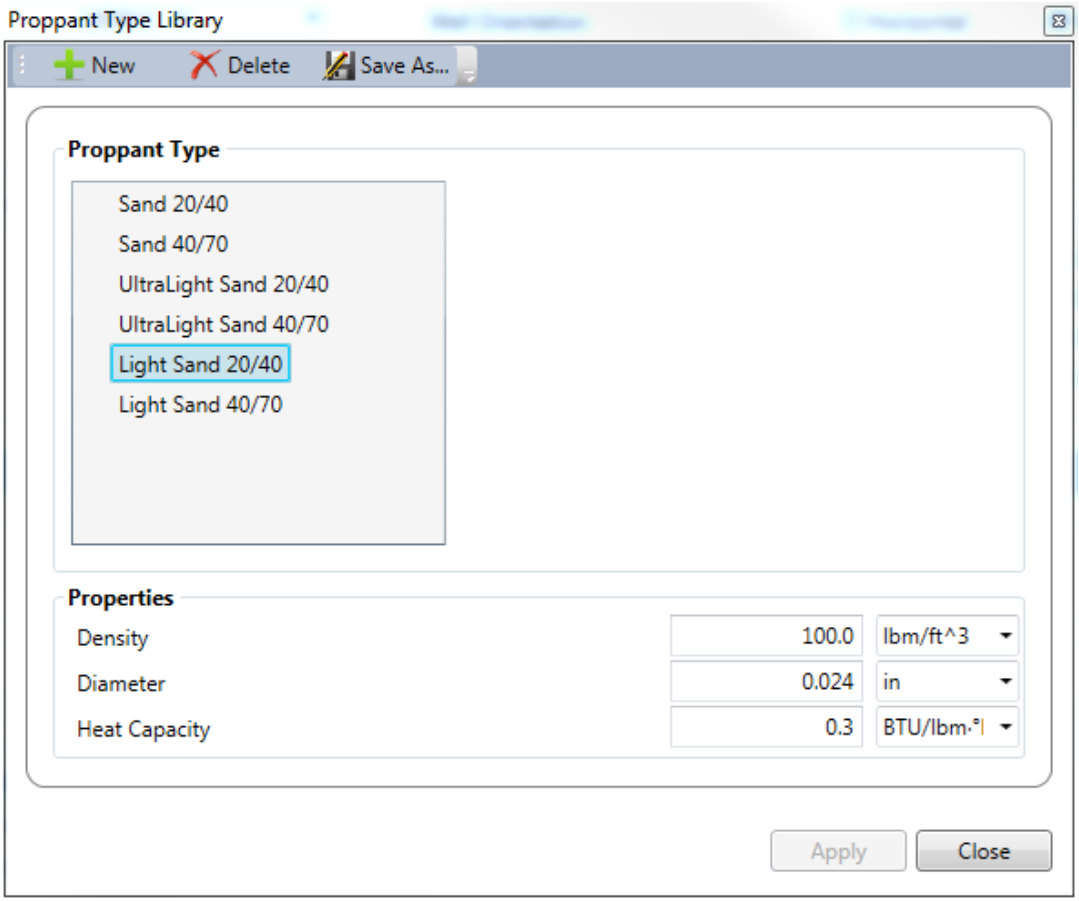

Density
It is the density of the proppant. Units: lbm/ft^3 or kg/m^3. 1 lbm/ft^3 = 16.0185 kg/m^3.

Diameter
It is the diameter of the proppant particle. Units: in or cm. 1 in = 2.54 cm.

Heat Capacity
It is the heat capacity of the proppant. Units: BTU/lbm.^oF or J/kg.^oK. 1 BTU/lbm.^oF = 4186.8 J/kg.^oK.

4.1.3 Fluid and Proppant Properties for Pumping Stage:

This section displays the fluid and proppant properties for the pumping stage selected in the above section on Pumping Schedule. It is possible for the user to edit some of the properties in this section instead of modifying them in the library. For example, in the figure below the pumping stage selected is the Pad.

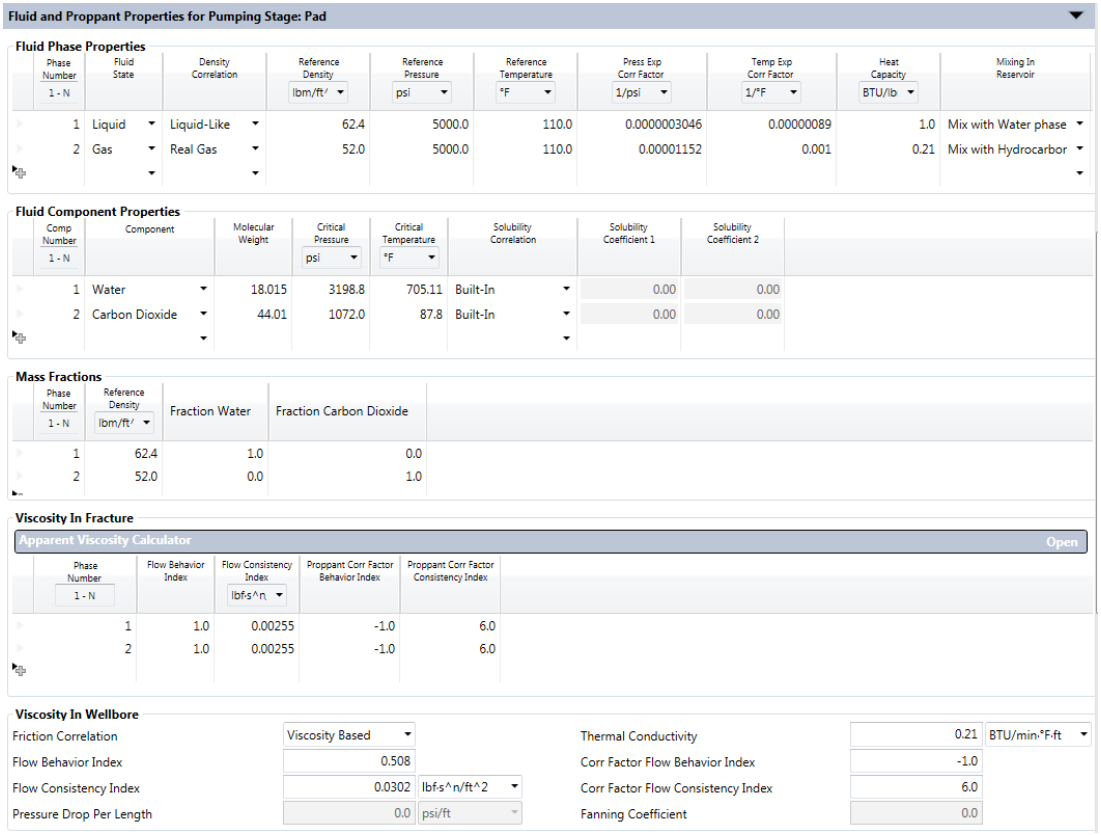

4.1.4 Reservoir

This section contains the reservoir properties used for productivity calculations. It includes the definition of the reservoir grid, the petrophysical reservoir properties, the relative permeability curve, and the fracture properties following flowback.

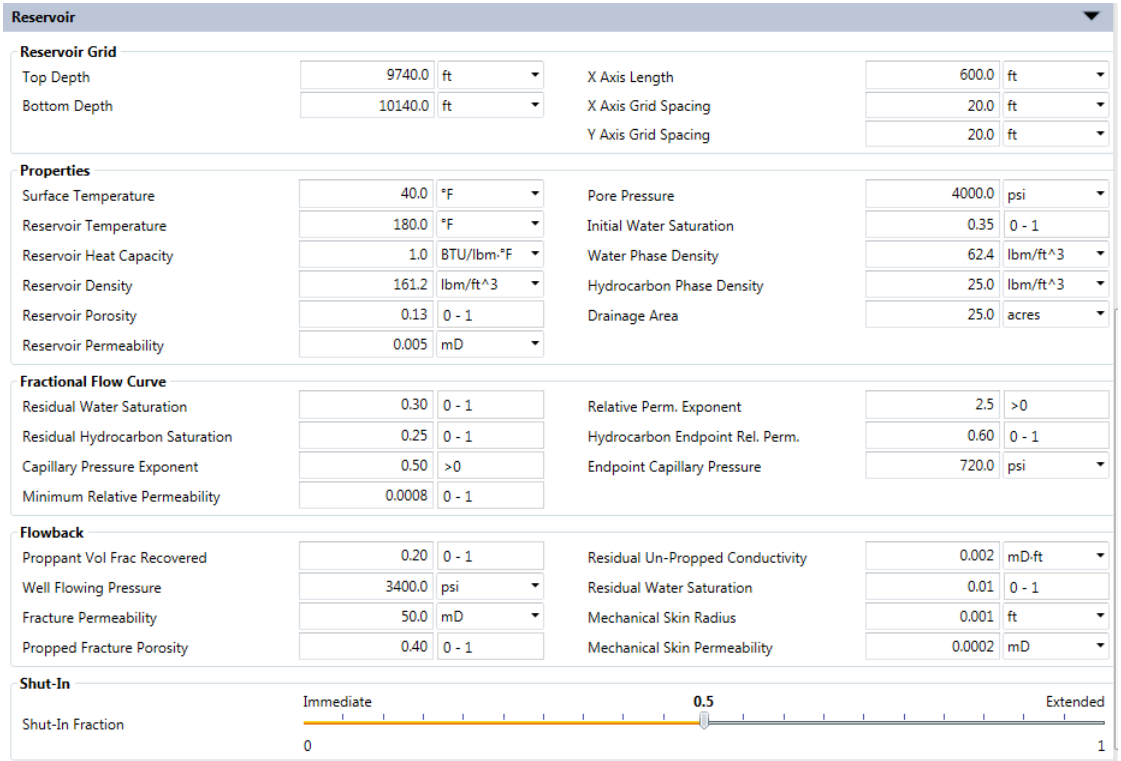

4.1.4.1 Grid

The reservoir grid is of Cartesian rectangular type.

Top Depth and Bottom Depth
They are the top and bottom depths of the reservoir. This specifies the limits for the Y-Axis. Units: m or ft. 1 ft = 0.3048 m.

X Axis Length
This specifies the limits for the X-Axis. Units: m or ft. 1 ft = 0.3048 m

X-Axis and Y-Axis Grid Spacing
They are the grid spacing on the X-Axis and Y-Axis of the rectangular grid. Units: m or ft. 1 ft = 0.3048 m.

4.1.4.2 Properties

The user needs to input various petrophysical reservoir properties.

Surface and Reservoir Temperature
They are the temperatures at the surface and inside the reservoir. Units: ^{o}F or ^{o}C.

Reservoir Heat Capacity
It is the heat capacity of the reservoir. Units: BTU/lbm.^{o}F or J/kg.^{o}K. 1 BTU/lbm.^{o}F = 4186.8 J/kg.^{o}K

Reservoir Density
It is the density of the reservoir. Units: lbm/ft^3 or kg/m^3. 1 lbm/ft^3 = 16.0185 kg/m^3.

Reservoir Porosity
It is the porosity inside the reservoir. Range: 0-1

Reservoir Permeability
It is the permeability inside the reservoir. Units: mD or µD. 1 mD = 1000 µD.

Pore Pressure
It is the pressure of fluids within the pores of the reservoir. Units: psi or Pa. 1 psi = 6894.7572932 Pa.

Initial Water Saturation
It is the initial water saturation inside the reservoir. Range: 0-1

Water and Hydrocarbon Phase Density
It is the density of the water and hydrocarbon phase inside the reservoir. Units: lbm/ft^3 or kg/m^3. 1 lbm/ft^3 = 16.0185 kg/m^3.

Drainage Area
It is the area available for drainage from that reservoir. Units: acres or m^2. 1 acre = 4046.8564224 m^2.

4.1.4.3 Fractional Flow Curve

Residual Water and Hydrocarbon Saturation
It is the residual water saturation and hydrocarbon in the reservoir. Range: 0-1

Minimum Relative Permeability
It is the minimum value of relative permeability in the reservoir. Range: 0-1

Capillary Pressure and Relative Permeability Exponent
It is the exponent obtained from the fractional flow curve.

Hydrocarbon Endpoint Relative Permeability
It is the value of the relative permeability when we have residual hydrocarbon saturation. Range: 0-1

Endpoint Capillary Pressure
This is a measure of the capillary pressure at high wetting-phase (typically water) saturation. If the region around the fracture is fully saturated with the wetting phase, this value represents the minimum drawdown that any wetting phase could be recovered from that region. Units: psi or Pa. 1 psi = 6894.7572932 Pa.

4.1.4.4 Flowback

Proppant Volume Fraction Recovered
It is the fraction of the proppant injected which flows back. Range: 0-1

Well Flowing Pressure
It is the pressure maintained at the bottomhole during flowback. Units: psi or Pa. 1 psi = 6894.7572932 Pa.

Fracture Permeability
It is the permeability inside the fracture during flowback. Units: mD or μD. 1 mD = 1000 μD.

Propped Fracture Porosity
It is the porosity inside the fracture based on the proppant placed. Range: 0-1

Residual Un-Propped Conductivity
It is the conductivity assuming no proppant is present. Units: mD or µD. 1 mD = 1000 µD.

Residual Water Saturation
It is the water saturation inside the fracture during flowback. Range: 0-1

Mechanical Skin Radius
The radius of mechanical skin is the radius of the damaged zone around the wellbore. This damage corresponds to the mechanical damage associated with mud invasion, etc. Units: m or ft. 1 ft = 0.3048 m

Mechanical Skin Permeability
It is the permeability of the damaged zone around the wellbore. Units: mD or µD. 1 mD = 1000 µD.

4.1.4.5 Shut In

A shut in fraction of 0 indicates immediate or forced flowback, whereas a shut in fraction of 1 implies extended shut in. These two are two extreme ends of the spectrum. The user has the flexibility of using any value from 0 to 1.

4.2 WELLBORE

This input tab defines the wellbore path, the tubing dimensions, the perforations, and the thermal properties of the wellbore. The wellbore path can be uploaded from a separate survey file.

Wellbore

Wellbore and Perforations

Dimensions

Tubing Inner Diameter	4.0	in	Casing Inner Diameter	5.0	in
Tubing Outer Diameter	4.5	in	Casing Outer Diameter	5.5	in
Insulation Outer Diameter	4.5001	in	Wellbore Diameter	5.6	in

Perforations

Perforation Pressure Drop Calculator — Open

Perforation Correlation Type	Discharge Coeffi		Friction Coefficient A	0.0	
Number of Open Perforations	20		Friction Coefficient B	0.0	
Perforation Diameter	0.45	in			
Discharge Coefficient	0.75	0.55 - 0.95			

Thermal Properties

	Thermal Conductivity			Annulus	
Fluid in Annulus	0.0056	BTU/min·°F·f	Fluid Density	62.4	lbm/ft^3
Tubing	0.159	BTU/min·°F·f	Fluid Viscosity	0.0000005	cP
Cement	0.0028	BTU/min·°F·f	Thermal Expansion	0.000355	°F
Insulation	0.0004	BTU/min·°F·f	Prandtl Number	2.75	
Casing	0.159	BTU/min·°F·f	Heat Exchange Correction Factor	0.25	
Rock	0.02	BTU/min·°F·f			

4.2.1 Dimensions

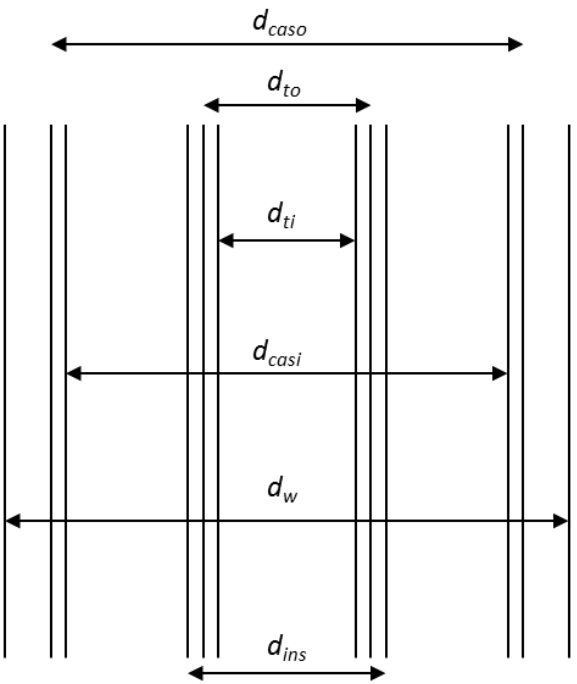

Diameters
The user needs to input inner tubing (d_{ti}), outer tubing (d_{to}), outer insulation (d_{ins}), inner casing (d_{casi}), outer casing (d_{caso}) and wellbore diameters (d_w). Units: in or cm. 1 in = 2.54 cm

4.2.2 Perforations

Perforation Diameter
This is the diameter of the perforation. It is denoted as d. Units: in or cm. 1 in = 2.54 cm.

Number of open perforations
This is the number of open perforations in the perforated region. It is denoted as N.

Perforation Pressure Drop
The user has the option of calculating the perforation pressure drop by three ways and it can be selected from the drop down menu for perforation correlation type. They are (a) Direct Correlation (b) Discharge Coefficient (c) Sand Erosion

a. Direct Correlation: The equation is given as: $\Delta P_{perf} = a_{perf} q^{b_{perf}}$ The user needs to input the values of the friction coefficients 'a' and 'b'
b. Discharge Coefficient: The equation is given as: $\Delta P_{perf} = 0.2369 \frac{\rho q^2}{d_{perf}^4 N^2 C_{disc}^2}$ The user needs to mention the value of the discharge coefficient, C_{disc}. The range is from 0.55 – 0.95.
c. Sand Erosion: The equation is similar to the one used above except that here C_{disc} is not constant. It is given by the correlation: $C_{disc} = \min\left(0.56 + 1.65 \times 10^{-4} m_{sand,cum}; 0.95\right)$ The value of $m_{sand,cum}$ and hence C_{disc} is calculated in the code.

In order to verify whether the perforation pressure drop predicted by any of the above methods matches reasonably with what the user is expecting, there is an inbuilt calculator which calculates the perforation pressure drop based on inputs such as Fluid Density and Fluid Flow Rate as shown below:

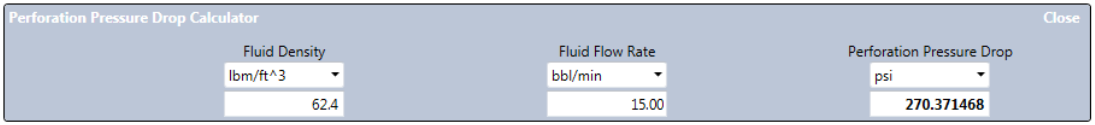

In order to use the calculator the user needs to click "Open" as shown in the following figure:



4.2.3 Thermal Properties

Thermal conductivities

The user needs to input thermal conductivities of fluid in annulus, tubing, cement, insulation, casing and rock. Units: BTU/min.^{o}F or W/^{o}K.m, 1 BTU/min.^{o}F = 103.8441 W/^{o}K.m.

Annulus

The user needs to input thermal properties of fluid in the annulus so that heat transfer coefficient in the annulus can be calculated. The inputs required are as follows:

a. Fluid Density: It is the density of the fluid in the annulus. Units: lbm/ft^3 or kg/m^3. 1 lbm/ft^3 = 16.0185 kg/m^3.
b. Fluid Viscosity: It is the viscosity of the fluid in the annulus. Units: cp or Pa.s. 1 cp = 0.001 Pa.s.
c. Fluid Expansion coefficient: It is the thermal expansion coefficient of the fluid in the annulus.
d. Prandtl Number: It is the Prandtl number (Pr) of the fluid in the annulus. It is defined as $\Pr = \frac{Cp \times \mu}{k}$ where Cp is the heat capacity of the fluid in the annulus, μ is the viscosity of the fluid in the annulus and k is the thermal conductivity of the fluid in the annulus.
e. Heat Exchange Correction Factor: The correlation used for calculating the heat transfer coefficient in the annulus overpredicts the heat transfer coefficient. Hence this factor is used. Range: Between 0 and 1

4.3 SIMULATOR SETTINGS

This input tab contains the meshing parameters, algorithm preferences, and initial grid parameters.

It is highly recommended that the user uses the default settings in running the simulator. In order to use the default settings the user has to simply click on the option “Import from Settings” and it will get populated with the default settings

Remarks on some of the numerical parameters

1) **Parameter 1 (Smooth_fac):**
This parameter controls how the rectangular elements are arranged on the boundary of the fracture. For example, with the default value of 1.5, the following arrangement of boundary nodes was seen and this poor arrangement led to a large time step jump.

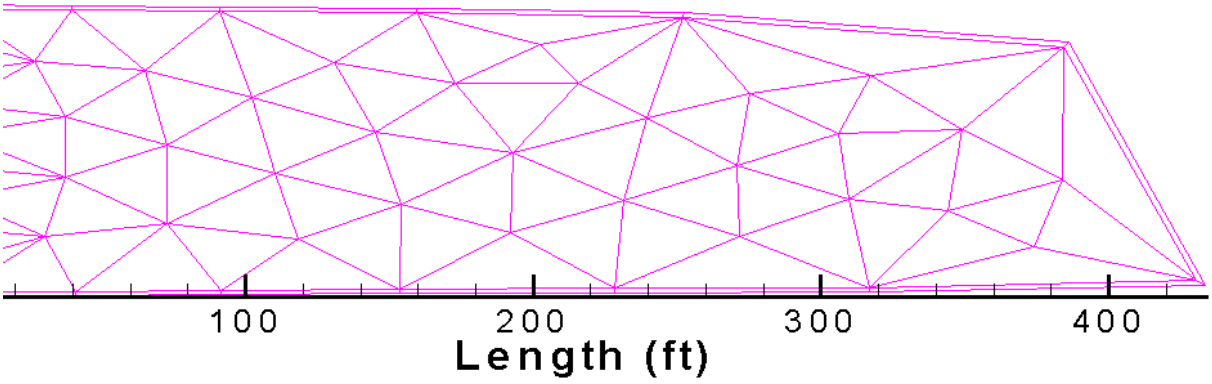

When this value was decreased to 1.1, the following arrangement of nodes was seen and now the time step jump is not observed

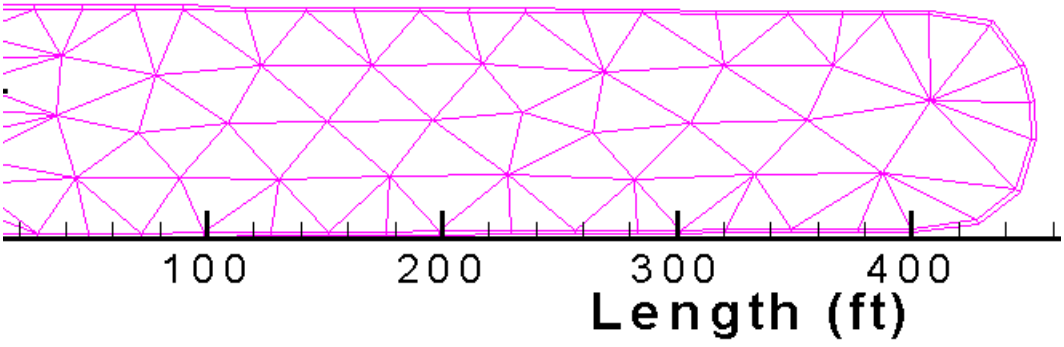

So in conclusion, if you see a large time step jump and if the mesh generated if not refined and has sharp corners, then decrease this parameter from the default value of 1.5 to 1.3 or 1.1

2) **Parameter 3 (Ralpha):**
The relaxation parameter or Ralpha controls the convergence of the iterative process. Since the problem is highly non-linear, large values of Ralpha may result in the divergence or oscillation of the iterative process. On the other hand, a low value of Ralpha slows down the computations. The default value used is 0.25. In order to obtain converging solution, restrict the value of Ralpha in the range (0.1 to 0.4)

3) **Parameter 4 (Bbl):**
This parameter controls the insertion of nodes on the boundary of fracture where there are rectangular elements. So decrease this parameter from the default value of 4 to say 1.5 in order to insert more nodes on the boundary of the fracture.

4) **Parameter 6 (Bbs):**
This parameter controls the insertion of interior nodes in the fracture where there are triangular elements. So decrease this parameter from the default value of 8 to say 2.5 in order to insert more nodes in the interior region of the fracture.

5) **Parameter 5 (Ainc):**
The default value is 3.5. Change this value to say 3.7 or 4, if you receive the error message that three nodes of the triangle element are in the same line and hence the triangle cannot be formed.

6) **Diffusion Coefficient of Proppant, Temperature and Saturation Equations**:
Oscillations are frequent when solving convection-dominated equations. We introduce a dispersion term to reduce oscillations. This term accounts for both physical diffusion (due to concentration gradients) and numerical dispersion. So if patches or unreasonable contour profiles are observed in proppant, temperature and saturation distribution inside the fracture, then increase the diffusion coefficient for the corresponding equation in order to smoothen the contour profiles. Avoid increasing the diffusion coefficient above 1000.

7) **Maximum fracture front advancement per time step:**
The default value is 3.5 and it acts like an indirect control for time step. So if you observe large time steps (say greater than 5 mins), then reduce this value to say 3 or 2.5 or 2

The following figure shows the settings that have been used in running the 70% Quality CO_2 Foam case in a vertical well.

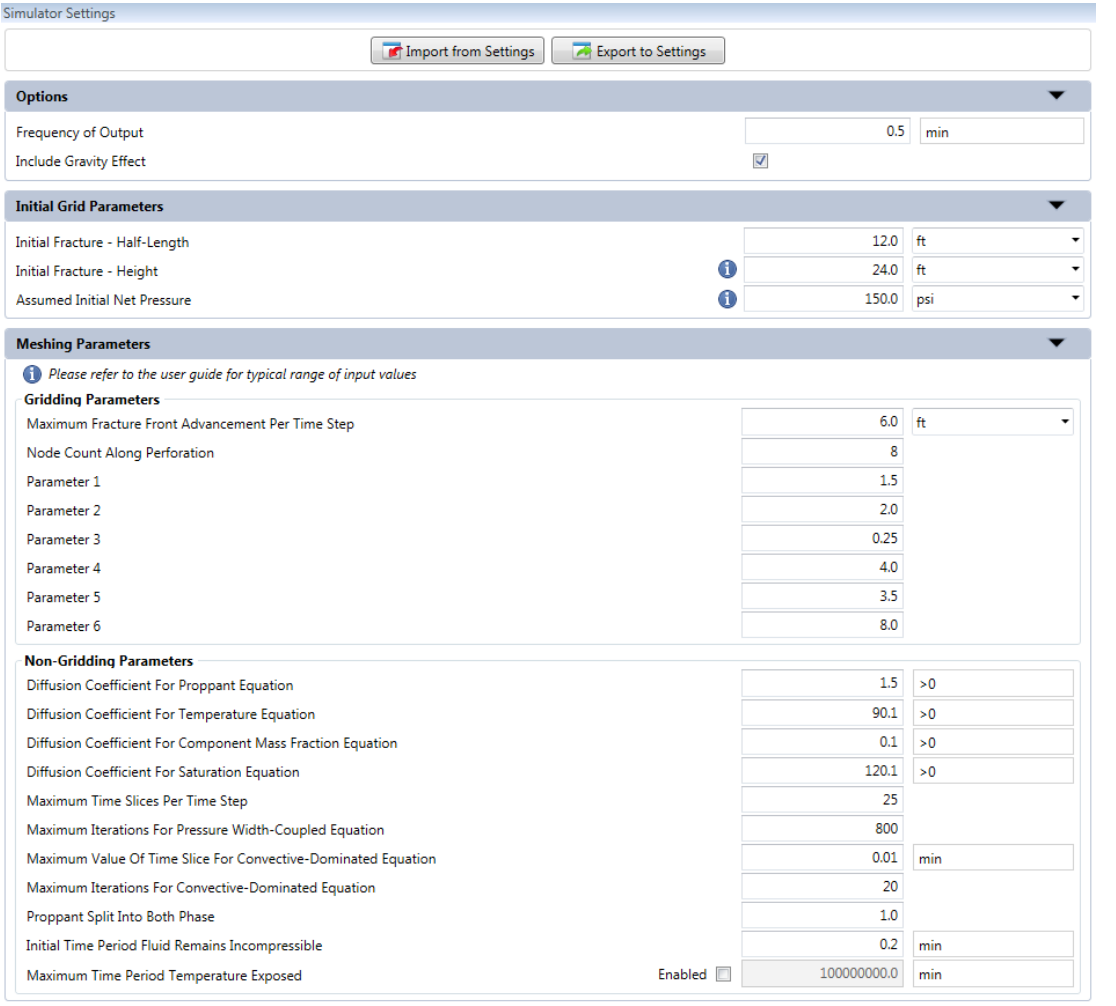

CHAPTER 5: SAVING AND LOADING DATA – FILE MENU

5.1 SAVING AND LOADING DATA – FILE MENU

The file menu in EFrac3D is similar to the file menu in most Windows applications. A description of each menu choice is given below.

New
When the user chooses New, they are presented with a New Project dialog, allowing them to create a new project based on an empty template, with the ability to select default units, SI or Field, or create a new project based on an existing project.

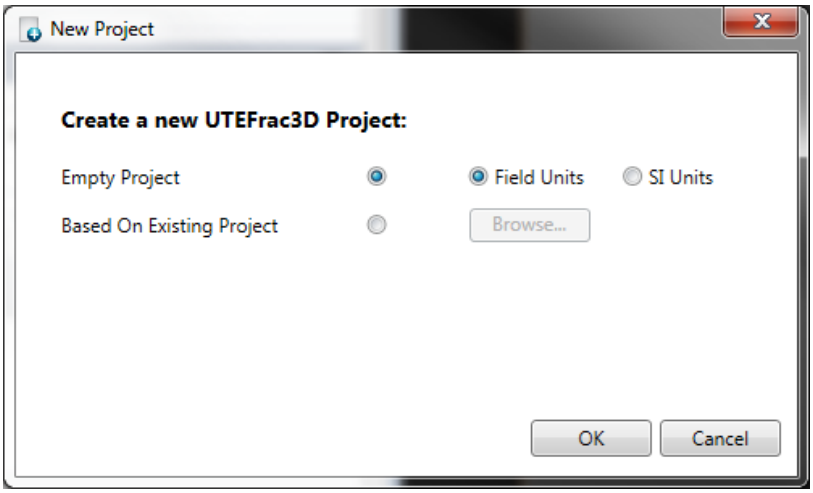

Open
When the user chooses Open, they are presented with a standard Windows File Open Dialog, allowing them to browse to and open an existing project file.

Save
When the user chooses Save, they are presented with a standard Windows File Save Dialog. If the file being saved is a New, empty file, its file name will be Untitled. You should change this to a suitable file name. Additionally, if this is the first time the user has saved a file, he/she is encouraged to navigate to *My Documents\UTEFrac3D\Datafiles* and save the file to this location.

Save As
When the user chooses Save As, he/she is for a file name and location.

Import Wellbore Profile
It allows the user to import a wellbore profile into the currently loaded project. Loading a wellbore profile will overwrite the current wellbore profile, if one exists. Upon completion of the import process, the Wellbore Pane in the graphics pane will display the 3D representation of the wellbore.

This function is always required for each new project created.

Recent Files
The file menu contains a section of recently opened files. Up to 10 files will be maintained in this list. If a file is deleted, and user chooses that file name from this list, they will be prompted to delete the file reference from the list.

Exit
It closes the application.

CHAPTER 6: RUNNING EFRAC3D & VIEWING RESULTS

The EFrac3D results frame is organized into six tabs. They are: (1) Wellbore (2) Fracture Propagation (3) Productivity Results (4) Fracture Contour Plot (5) Invasion Reservoir Plot (6) Productivity Calculations Plot

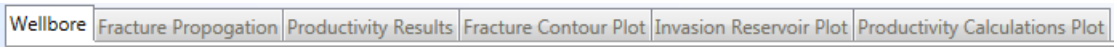

6.1 WELLBORE

This section displays the contour plots across the wellbore. The user can also see animations over the entire pumping schedule. The dropdown menu allows the user to see the following properties

Temperature
It is the temperature of the fluid inside the wellbore. Units: ^{o}F

The following figure shows the temperature contour at 0.549 min.

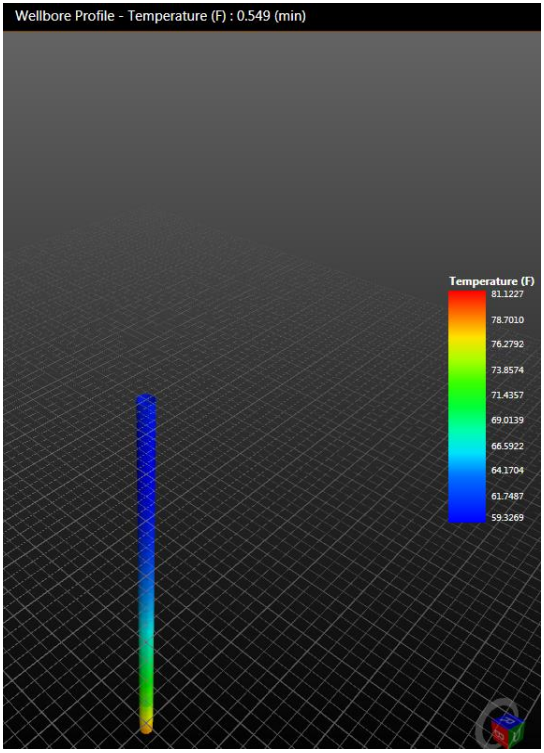

Pressure
It is the pressure of the fluid inside the wellbore. Units: psi

The following figure shows the pressure contour at 0.549 min.

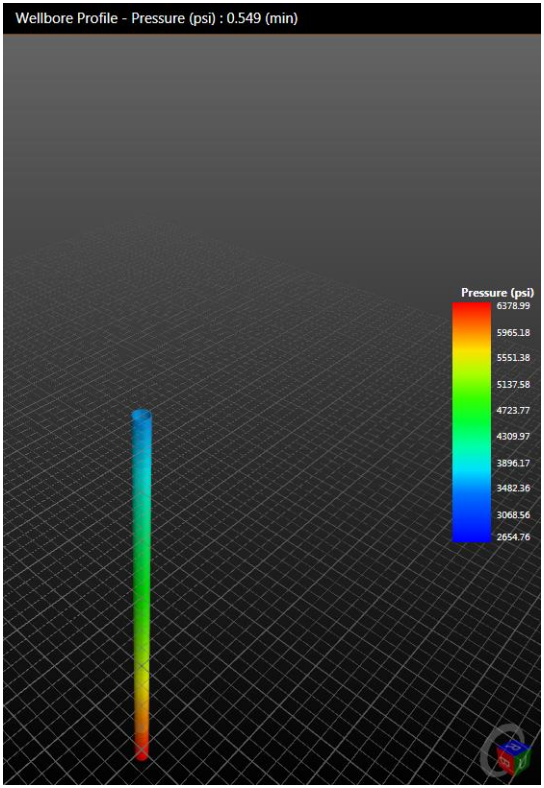

Density 1 and Density 2
They are the density of the two fluid phases respectively inside the wellbore. Units: lbm/ft^3

Density Slurry
It is the density of the slurry inside the wellbore. Units: lbm/ft^3

Saturation 1 and Saturation 2
They are saturation of the two phases respectively.

Proppant Conc
It is the proppant concentration inside the wellbore.

The following figures show the values of the proppant concentration across the wellbore at 13.941 min and 24.925 min. This illustrates that proppant injected at the well head takes certain time to reach to bottom of the well. It also shows two proppant concentrations inside the well from the two adjacent stages

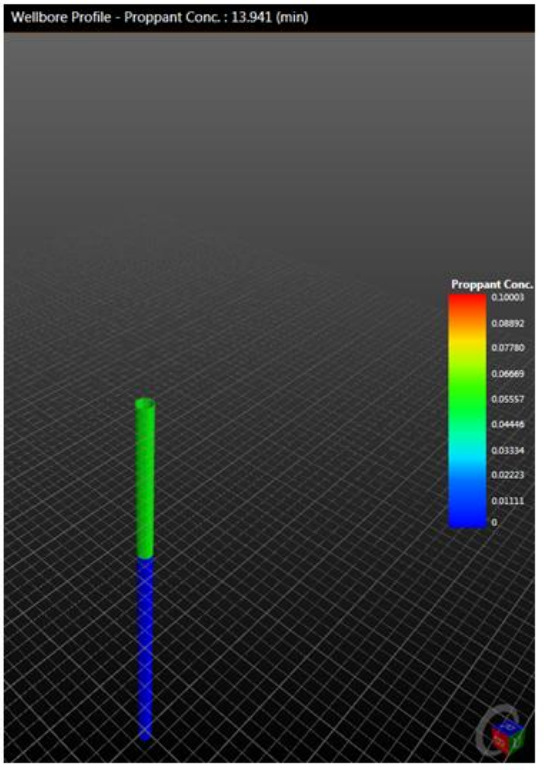

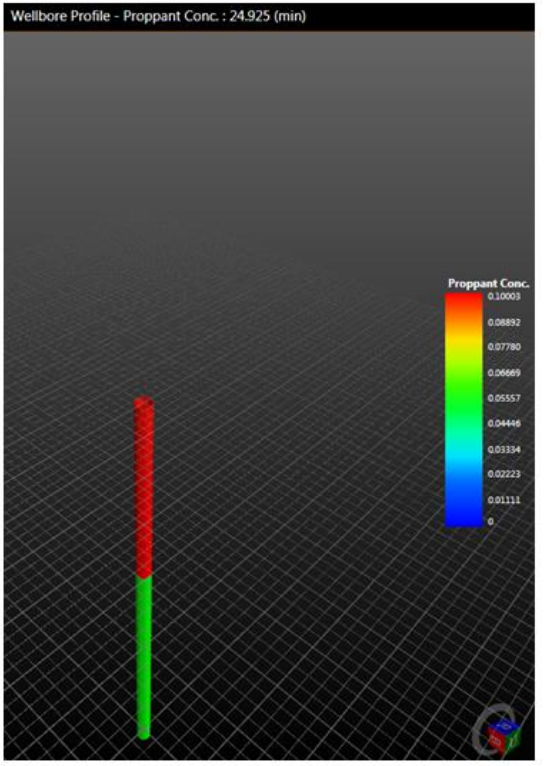

Velocity
It is the velocity of the fluid inside the wellbore. Units: ft/min

Reynolds No
It is the Reynolds Number of the fluid inside the wellbore.

Viscosity
It is the viscosity of the fluid inside the wellbore. Units: cp

Gravity DP/DL
It is the pressure drop per unit length in the wellbore due to the gravity. Units: psi/ft

Friction DP/DL
It is the pressure drop per unit length in the wellbore due to the friction. Units: psi/ft

DP/DL
It is the net pressure drop per unit length in the wellbore taking into account the contrasting effects of gravity and friction. Units: psi/ft

Liq. Comp 1 and Liq. Comp 2
They are fraction of the two components in the liquid phase respectively.

Gas Comp 1 and Gas Comp 2
They are fraction of the two components in the gas phase respectively.

Fraction Comp 1 and Fraction Comp 2
They are the overall fractions of the two components in both the phases combined.

6.2 FRACTURE PROPAGATION

This section displays variation of properties with respect to time. Again the user has option of choosing what charts to display by selecting from the dropdown menu. Also it displays four chart windows at the same time which allows the user to draw comparisons. Also if the user would hover over any point and click on the chart then it displays the exact time and the value of the property on the Y-axis. An example of the Charts window is shown below:

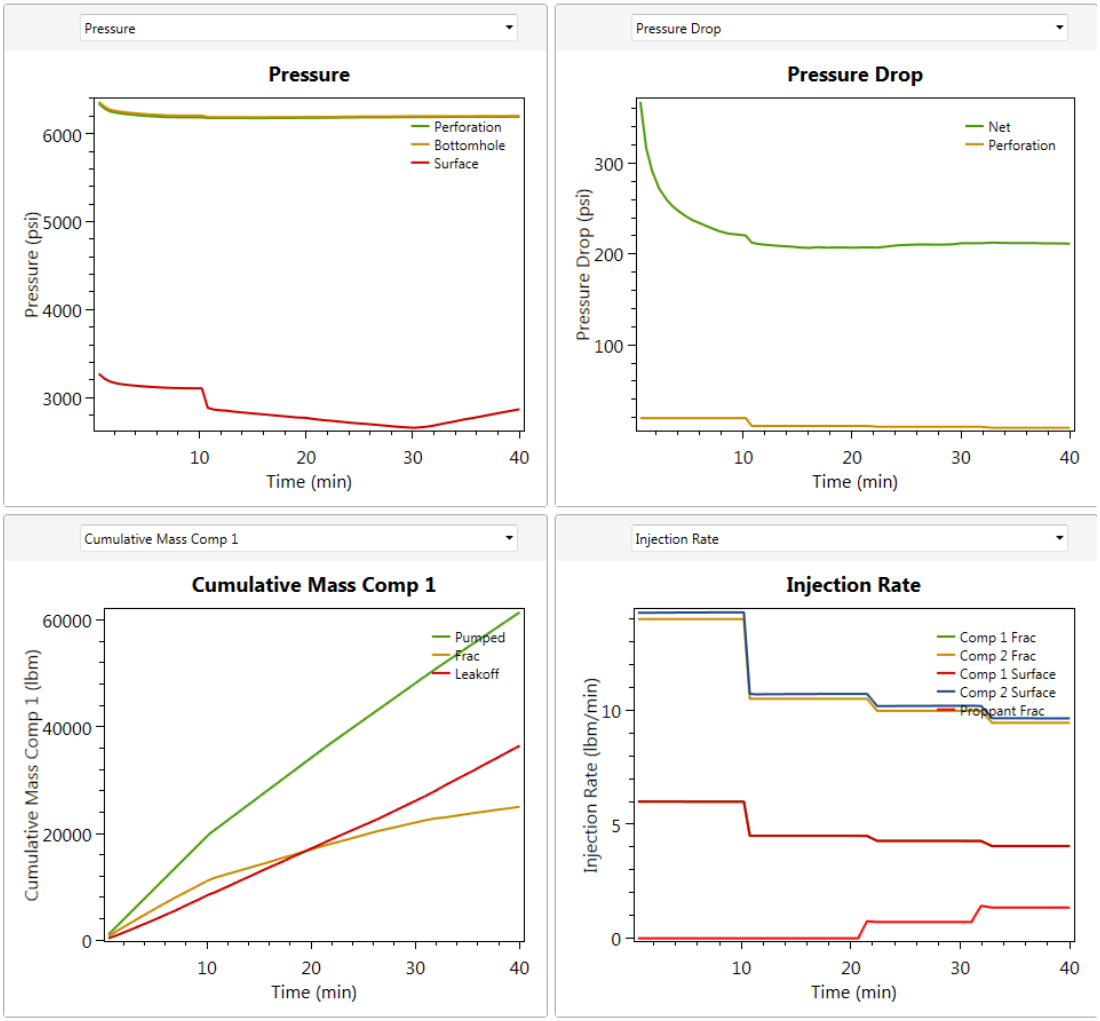

The properties available in the dropdown menu are:

Half-Length and Height

It displays both the fracture half – length (ft) and height (ft) simultaneously on the same chart over the entire pumping schedule.

Top and Bottom
It displays the True Vertical Depth (ft) above and below the injection point. TVD above the injection point is called Top and TVD below the injection point is called Bottom.

Width
It displays the maximum and the average fracture width (in) over the entire pumping schedule.

Fracture Area
It displays the fracture area (ft^2) over the entire pumping schedule.

Pressure Drop
It displays the net and the perforation pressure drop (psi) over the entire pumping schedule.

Temperature
It displays the bottomhole and the surface temperature (^oF) over the entire pumping schedule.

Volume
It displays the total injected volume (bbl), volume in the fracture, volume lost due to leak off and the volume of the proppant over the entire pumping schedule.

Efficiency
It is the ratio of volume in the fracture to the total volume injected.

Cumulative Mass Comp 1 and Comp 2
It displays the cumulative mass (lbm) of that component pumped, mass in the fracture and mass that has leaked off. Since mass is conserved, mass pumped is addition of mass in the fracture and mass leaked off and can be verified from the chart.

Cumulative Mass Proppant
It displays the cumulative mass (lbm) of proppant pumped.

Injection Rate
It displays the injection rate in lbm/min of components 1 and 2 at the surface and at the fracture and also the proppant injection rate at the fracture.

Proppant Concentration
It displays the proppant concentration in the fracture and at the surface. It is important to note there is an offset between the two

Saturation Phase 1
It displays the saturation of phase 1 in the fracture and at the surface

6.3 PRODUCTIVITY RESULTS

This section displays important productivity results related that are obtained from the simulation as shown in the figure below:

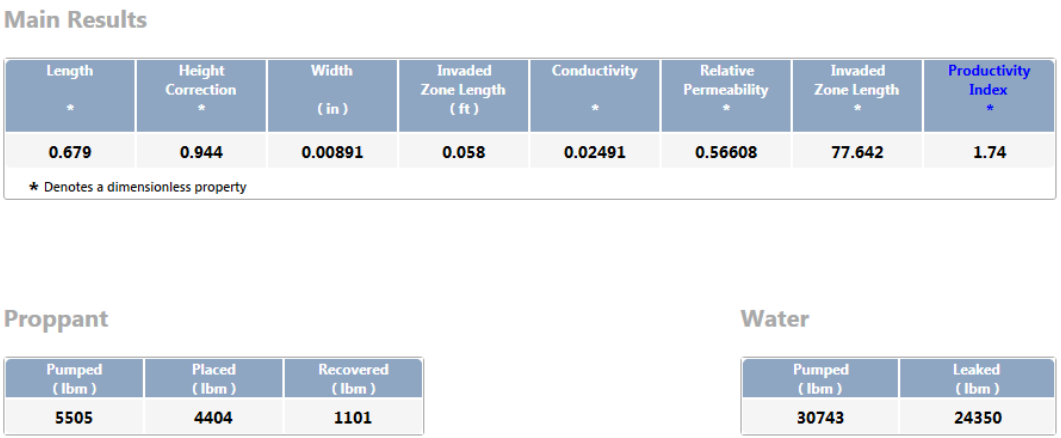

Main Results

Length *	Height Correction *	Width (in)	Invaded Zone Length (ft)	Conductivity *	Relative Permeability *	Invaded Zone Length *	Productivity Index *
0.679	0.944	0.00891	0.058	0.02491	0.56608	77.642	1.74

* Denotes a dimensionless property

Proppant

Pumped (lbm)	Placed (lbm)	Recovered (lbm)
5505	4404	1101

Water

Pumped (lbm)	Leaked (lbm)
30743	24350

Length
The dimensionless length is the productive fracture length divided by the equivalent drainage radius. The drainage radius is obtained from the value of the fracture drainage area provided by the user.

Height Correction
This coefficient expresses how much of the pay zone height is drained by the fracture. It is the ratio of the fracture height (within the pay zone) divided by the pay zone height. This ratio ranges from 0 - when the fracture is not within the payzone - to 1 – when the fracture covers the entire pay zone height (and may extend beyond).

Width
It displays the average fracture width (in).

Invaded Zone Length
It displays average invaded zone length (ft). The invaded zone length is obtained from a mass balance over the mass of fluid leaking-off and invading the reservoir.

Conductivity
The dimensionless fracture conductivity is the average fracture conductivity divided by the product of the fracture length multiplied by the permeability of the reservoir.

Relative Permeability
It is the average value of the relative permeability.

Dimensionless Invaded Zone Length
This is the average value of the invaded zone length divided by the fracture width.

Productivity Index
It is the dimensionless productivity index and is one of the important result obtained through the simulation.

Proppant Mass Distribution
It displays the mass of proppant in lbm that is pumped, placed in the fracture and that is recovered during flowback.

Water Mass Distribution
It displays the mass of water in lbm that is pumped and that has leaked outside the fracture. In the case when the fracturing fluid does not have water, then this result would not be displayed.

Also in order to analyze the results better, graphical representation of the following variables against the fracture length is made:

Fracture Drainage
This area is the maximum area of drainage allowed for a given fracture treatment. For a traditional vertical well, it corresponds to the drainage area of the well. For multi-stage horizontal wells, it corresponds to the area of drainage delimited by the spacing between consecutive stages and between adjacent wells.

Height
It displays the height of the fracture against the fracture length.

Conductive Width
It displays the conductive width of the fracture against the fracture length.

Invaded Zone Length
It displays the invaded zone length (ft) as a function of the fracture length. The invaded zone length is obtained from a mass balance over the mass of fluid leaking-off and invading the reservoir.

Invaded Zone Saturation
It is the saturation of water in the invaded zone against the length of the fracture.

Relative Permeability
It displays the relative permeability against the fracture length. It is important to observe that the relative permeability is very low when the invaded zone length is high.

Fracture DL Conductivity
The dimensionless fracture conductivity is the average fracture conductivity divided by the product of the fracture length multiplied by the permeability of the reservoir

Two variables are plotted adjacent to each other for comparison purpose.

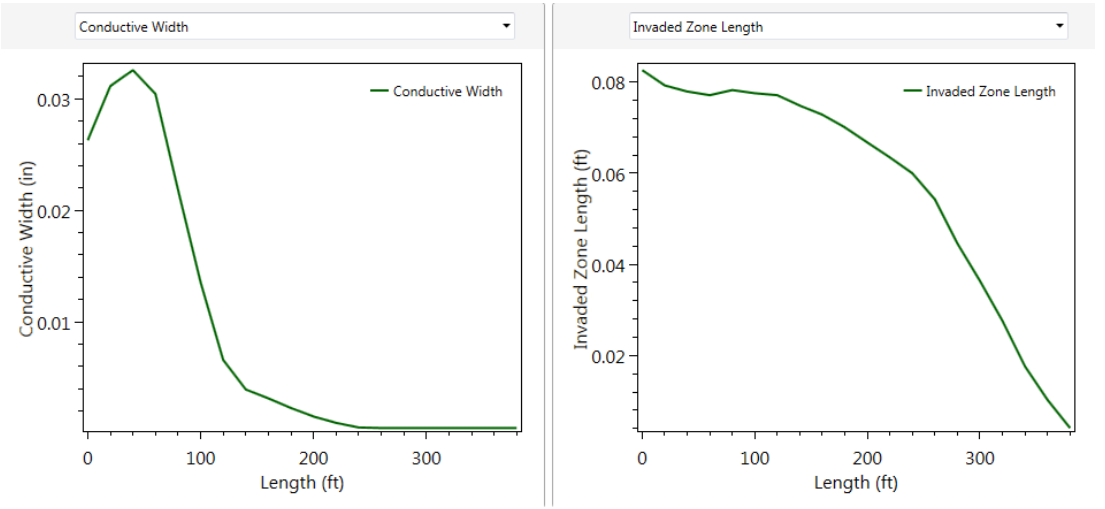

6.4 FRACTURE CONTOUR PLOT

This section displays fracture contour plots of various properties against the half length of the fracture and its animation with respect to time. The user has various display options to choose from, such as whether to include mesh or not, or what should be the fill style. The variables that the user can select from the dropdown menu are as follows:

Width
It displays the fracture width (in) contour at various times.

The following figure shows the width contour at the end of pumping

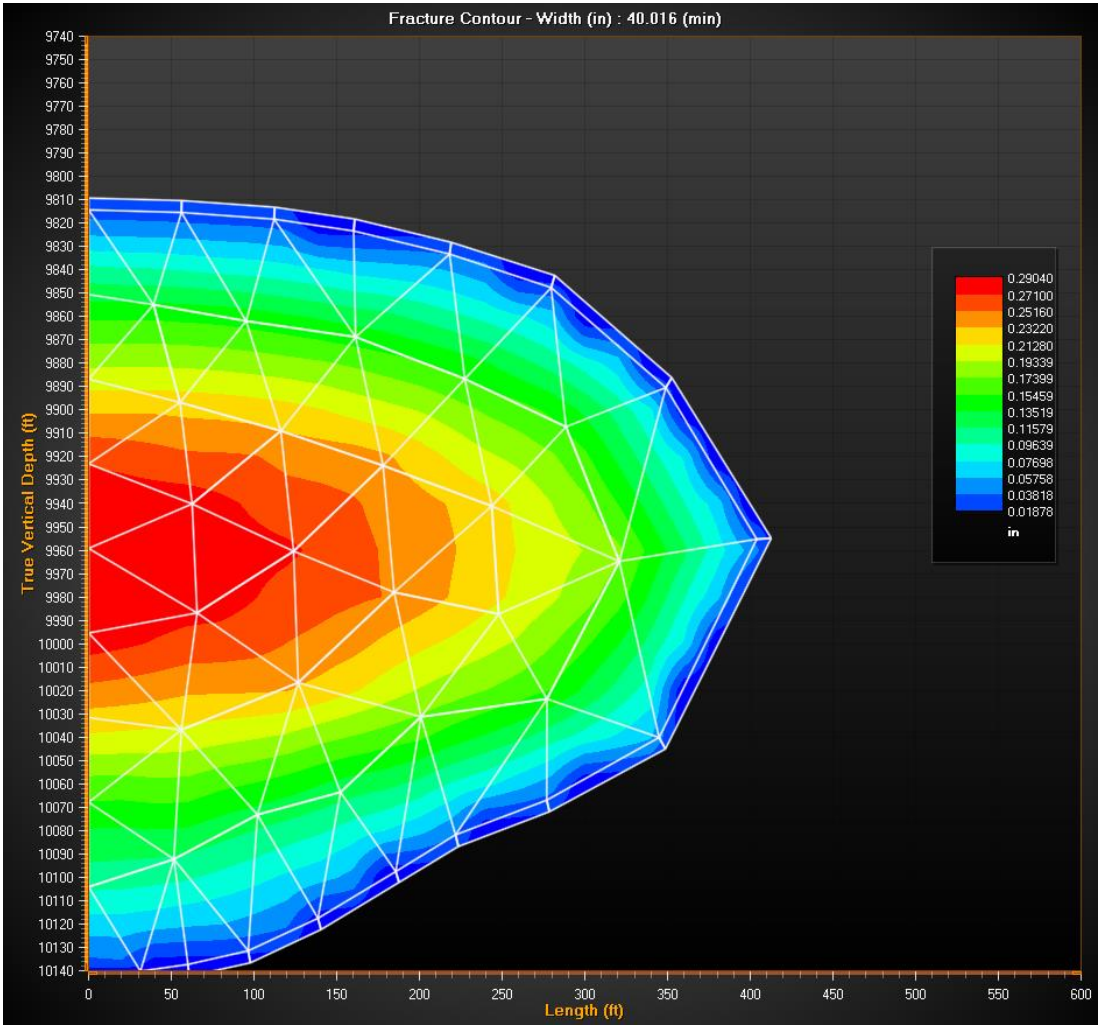

Net Pressure
It displays the net pressure (psi) inside the fracture at various times.

Volumetric and Mass Solid Concentration
It displays the concentration of solid proppant based on volumetric and mass basis inside the fracture.

Solid Mass per Area
It displays the solid proppant mass per unit area (lb/ft^2) in the fracture.

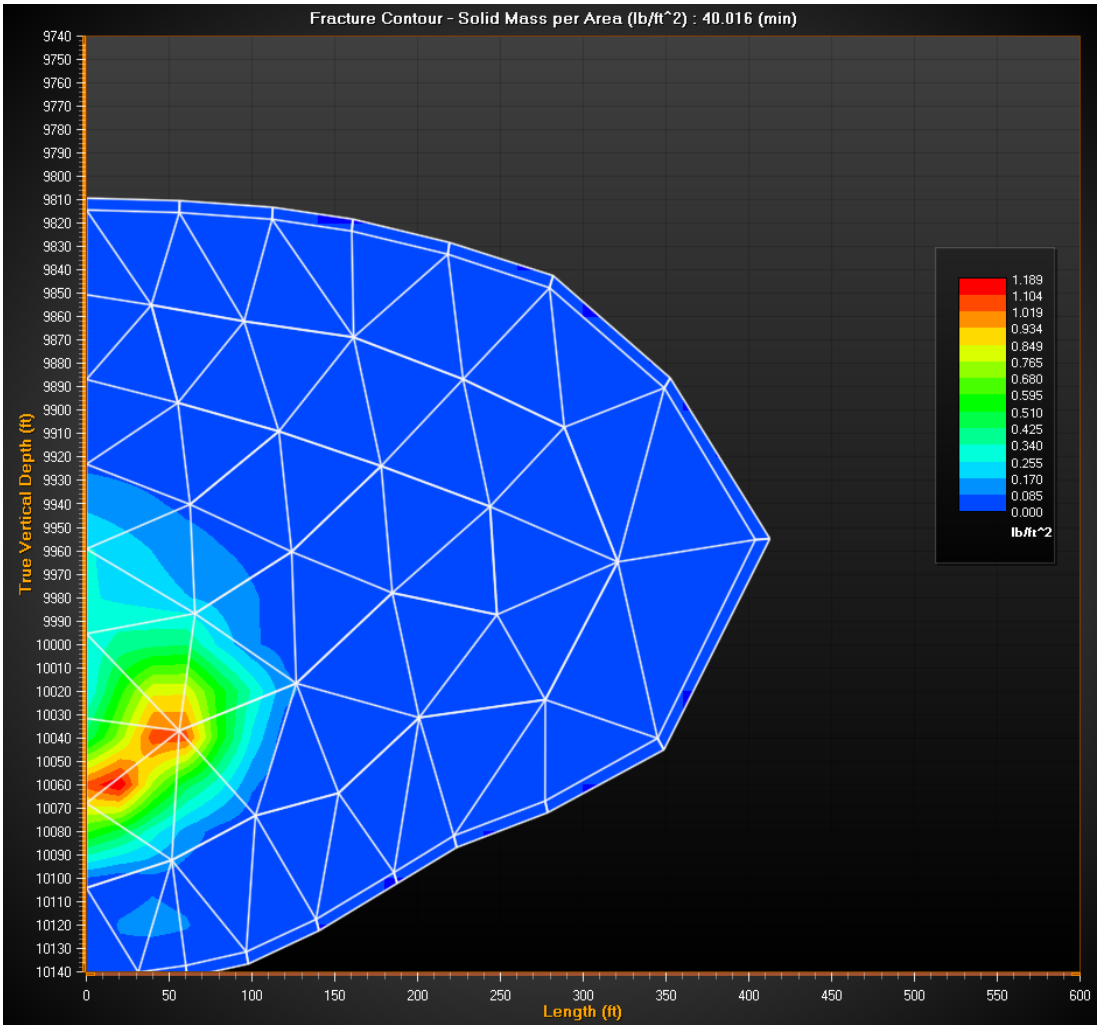

Fluid Pressure
It displays the fluid pressure (psi) inside the fracture at various times.

Temperature
It displays the fluid temperature (^{o}F) inside the fracture at various times.

Density Fluid
It displays the density of the fluid (lb/ft^3) inside the fracture at various times.

Density Phase 1 and Density Phase 2

It displays the density of the fluid phases 1 and 2 respectively (lb/ft^3) inside the fracture at various times.

Density Slurry

It displays the density of the slurry (lb/ft^3) inside the fracture at various times.

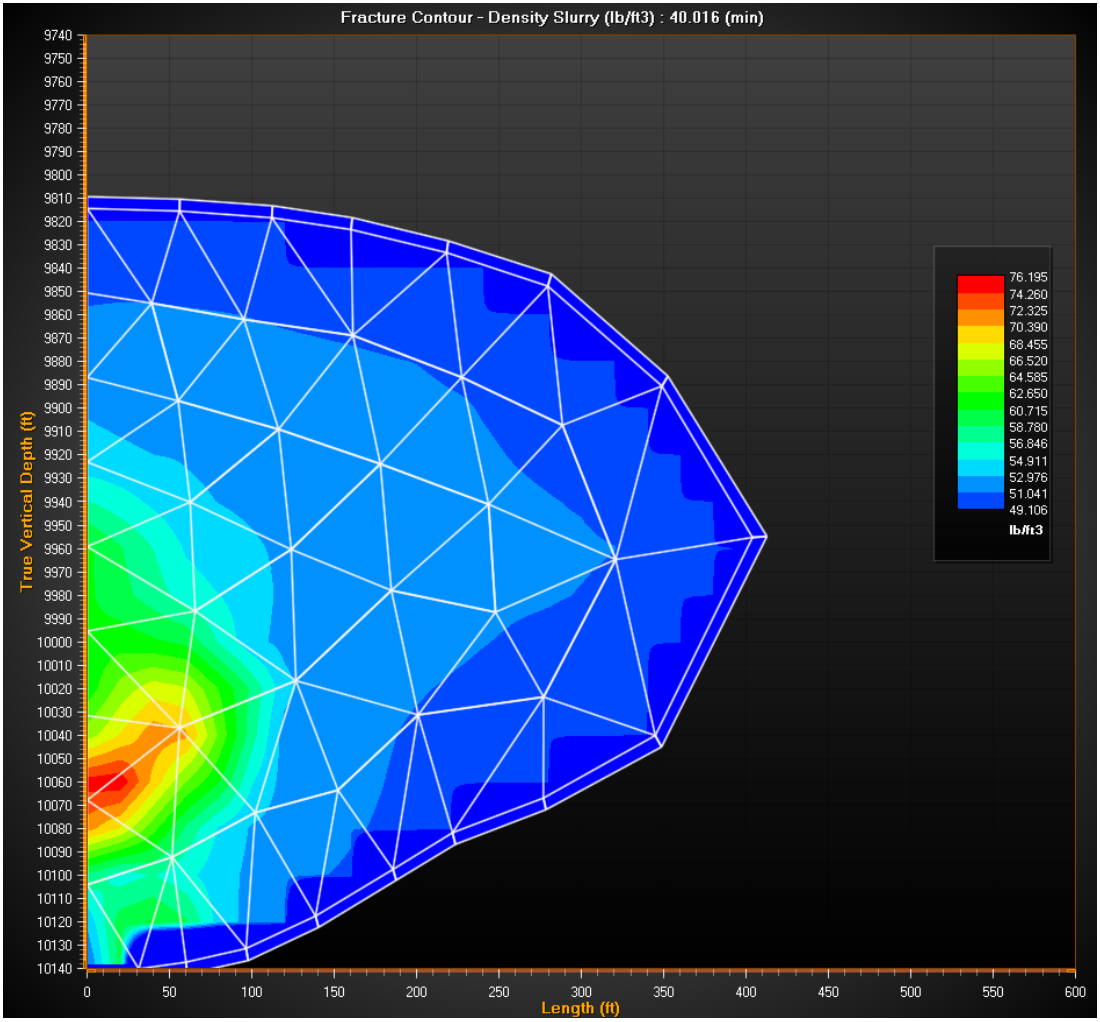

Saturation Phase 1 and Saturation Phase 2
It displays the saturation of the fluid phase 1 and 2 respectively inside the fracture at various times.

Liquid Fraction Comp 1 and 2
It displays the fraction of the two components in the liquid phase inside the fracture at various times.

Gas Fraction Comp 1 and 2
It displays the fraction of the two components in the gas phase inside the fracture at various times.

Power Law Exponent
It displays the power law exponent used in the fluid viscosity characterization inside the fracture at various times.

Consistency Index
It displays the consistency index ($lbf.s^n/ft^2$) used in the fluid viscosity characterization inside the fracture at various times.

6.5 INVASION RESERVOIR PLOT

This section gives the contour plots of the mass (lbm/ft^2) of the two components that have invaded into the reservoir due to leak-off. The reservoir grid is shown in the background.

The following figure shows the contour plot of the mass of component 1 that has invaded into the reservoir at the end of pumping.

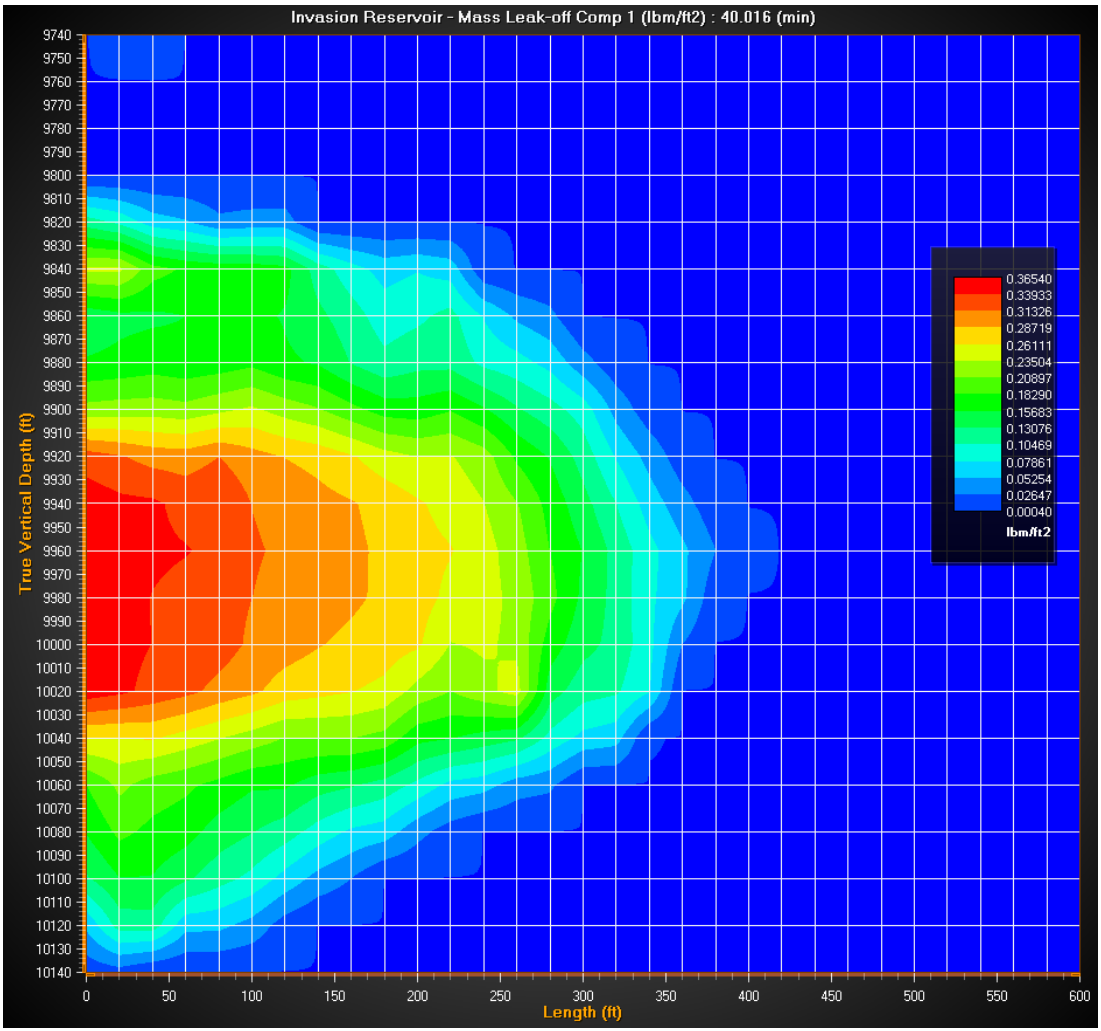

6.6 PRODUCTIVITY CALCULATIONS PLOT

This section displays the properties used for productivity calculations at 4 distinct times. The times are: 1) Initial 2) End of Pumping 3) After Shut-In 4) Flowback

The various properties which are available from the dropdown menu are as follows:

Width

It displays the width (in) at the 4 different times. The contour plots at the 4 different times are shown below.

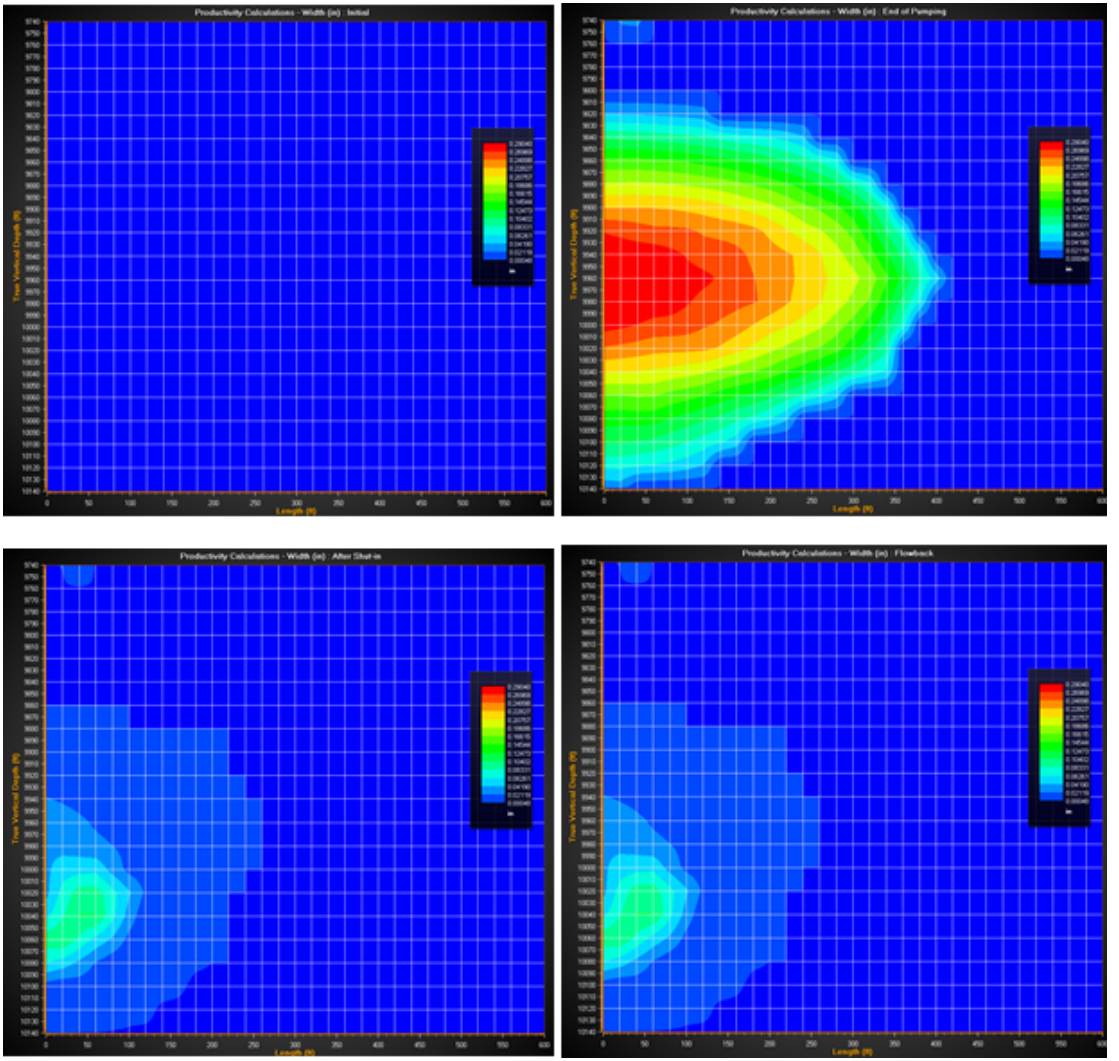

Pressure

It displays the pressure (psi) in the reservoir.

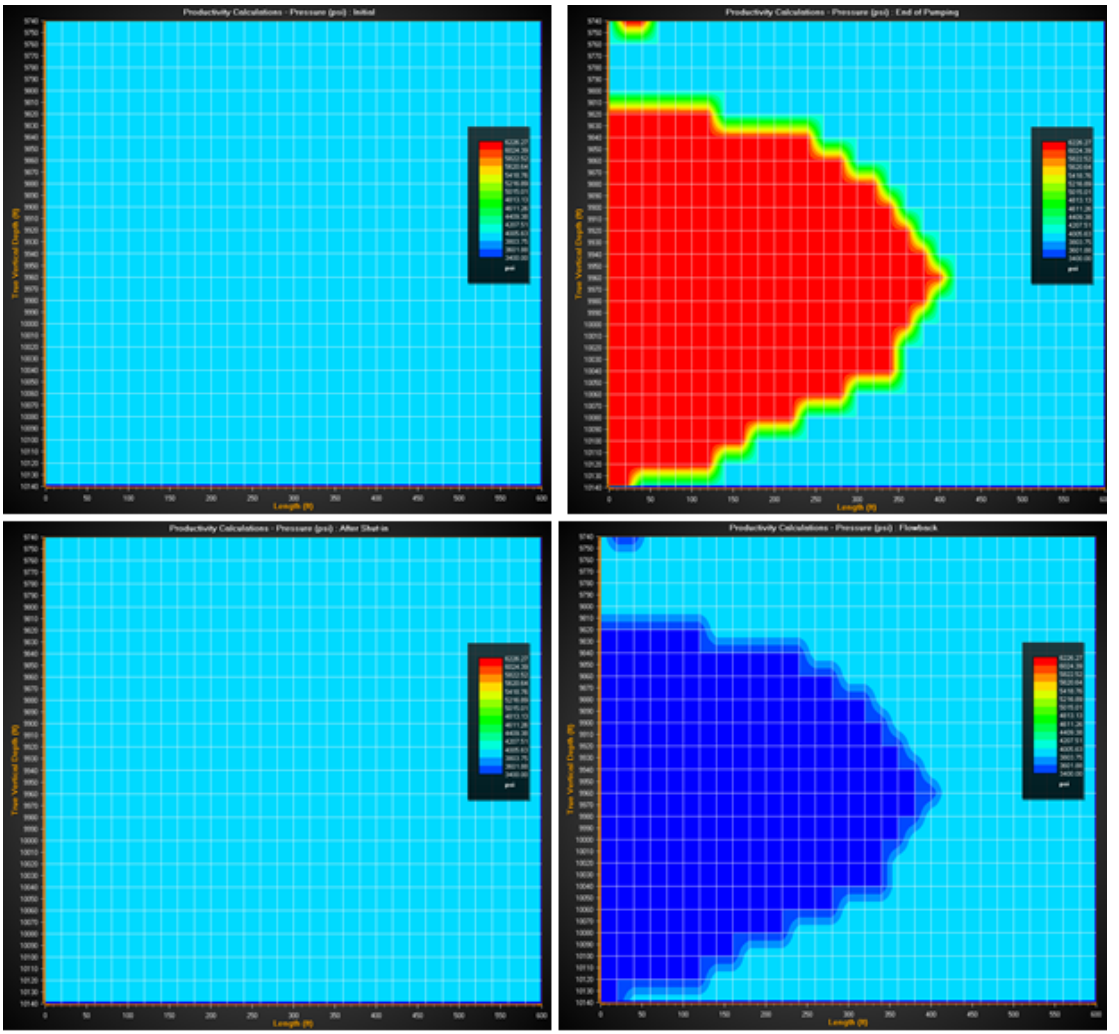

Mass Invasion in Water and HC Phase

It displays the mass of fluid (lbm/ft^2) invaded from the fracture into the water and hydrocarbon phases present in the reservoir.

Water and HC Saturation

It displays the water and hydrocarbon phase saturation inside the reservoir.

Relative Permeability to HC

It displays the relative permeability to HC of fluid that has invaded the reservoir.

Invaded Zone Length
It displays the length (ft) of the invaded zone inside the reservoir.

.

CHAPTER 7: TROUBLE SHOOTING – STRANGE RESULTS

It is not always possible that the EFrac3D simulator will run successfully in the first attempt. In the event that the simulator fails to generate any output or stops running, please refer to the following guidelines which will help in troubleshooting.

1) Make sure that all the inputs that the user wanted to enter have been entered correctly and have been saved after entering. It is possible sometimes that the user enters a value but forgets to save it.
2) Sometimes it is possible that the leak-off coefficient entered is high and all the fluid pumped gets leaked out of the fracture, so there is no fluid left for the fracture to propagate. So in that case, the leak-off coefficient will have to be decreased.
3) The best way to troubleshoot is to go to the Output Folder and open the files such as Variable_Time.dat and Wellbore_Profile.dat and look at the values in these files. It is possible that if the simulator is not running, then some of the values in them will not be practical and this will give the user an idea about where the simulator is failing
4) In the simulator settings, the only place that the user can modify in order to make the simulator run is the Gridding parameter "Maximum Fracture Front Advancement Per Time Step". Please refer to the 18 example cases for the values of this parameter that have been used.
5) Refer to example cases whenever you are faced with simulator not running or not showing outputs

EFrac3D is not completely fool-proof. Therefore, always make sure to type in reasonable values. Even for reasonable values, problems can sometimes be encountered. Please let us know of any problems you face.

CHAPTER 1: INTRODUCTION

1.1 BACKGROUND

The use of gases and foams has experienced a significant resurgence in popularity with the development of unconventional reservoirs. Current practices in energized treatments, using gases and foams, remain rudimentary in comparison to other fracturing fluid technologies. None of the available 3D fracturing models for incompressible water-based fluids have been able to capture the thermal and compositional effects that are important when using energized fluids, as their constitutive equations assume single-phase, single-component, incompressible fluid flow. These models introduce a bias in fluid selection because they do not accurately capture the unique behavior of energized fluids. The lack of modeling tools specifically suited for these fluids has hindered their design and field implementation.

1.2 EFRAC3D SIMULATOR

The simulator uses a fully compositional 3D fracturing model to answer some of the questions surrounding the design of energized treatments. The new model is capable of handling any multi-component mixture of fluids and chemicals. Changes in fluid density, composition, and temperature are predicted using an energy balance equation and an equation of state. A wellbore model, which relates the surface and bottomhole conditions, determines the pumping requirements. Fracture performance is assessed by a fractured well productivity model that accounts for damage in the invaded zone and finite fracture conductivity.

The combination of the fracture, productivity, and wellbore models forms a standalone simulator that is suitable for designing and optimizing energized treatments. The simulator offers a wide range of capabilities, making it suitable for many different applications ranging from hydraulic fracturing to long-term injections for enhanced oil recovery, well clean-up, or carbon sequestration purposes. The model is applicable to any well configuration: vertical, deviated, or horizontal. The resolution of the full 3D elasticity problem enables us to propagate the fracture across multiple layers, where height growth is controlled by the vertical distribution of the minimum horizontal stress.

CHAPTER 2: 3D COMPOSITIONAL FRACTURE MODEL

This chapter presents the theories and equations that form the basis of the first 3D compositional fracturing model. The model predicts changes in fluid temperature, density, and composition inside the fracture and along the wellbore. The objective of this chapter is to formulate a well-posed system of equations governing fracture propagation.

The formulation of the problem intends to be as general as possible. The fracturing fluid consists of multiple components (*NC*), multiple phases (*NP*), and proppant distributed within the *NP* phases. There is no assumption regarding phase behavior and fluid rheology. Any *a priori* model may be implemented to model the fluid behavior since these properties are evaluated locally at each node.

2.1 PROBLEM STATEMENT

2.1.1 Fracture Geometry

The fracture is assumed to be planar, vertical, and symmetric with respect to the wellbore (bi-wing). There is no assumption regarding the shape of the fracture, which can grow both in length and in height. Fracture width (along the *z*-axis) is negligible compared to fracture height (along the *y*-axis) and length (along the *x*-axis). The 3D fracture geometry is contained in the *x*-*y* plane, as shown in Fig. 2.1. The fracture width, which is normal to the *x*-*y* plane, is an unknown that is calculated for each node located at a given *x*- and *y*-coordinates; therefore, the 3D planar fracture model is a 2D mathematical problem. Ω is the fracture surface that is delimited by the fracture contour $\partial\Omega$. This is the domain in which we are solving the constitutive equations. $\partial\Omega_f$ is the fracture front; $\partial\Omega_p$ is the perforated interval along the wellbore; and $\partial\Omega_c$ is the non-perforated section of the wellbore that is contained in the fracture propagation plane.

2.1.2 Main Variables for Fluid and Proppant

The fracturing fluid consists of *NP* fluid phases and *NC* components distributed among these *NP* phases. Energized fluids are either single-phase or two-phase mixtures, so *NP* is equal to 1 or 2. The fracturing fluid may transport proppant, and the mixture is referred to as slurry. Fig. 2.2 shows the notation introduced for two-phase fluids carrying proppant. For fluid phases, the convention is that subscript 1 refers to the liquid phase and subscript 2 refers to the gas phase. For components, subscript 1 refers to the water component (if water is present) and the following

subscripts refer to the energized components (CO_2, N_2, MeOH, etc.). As indicated in the nomenclature, the superscript * refers to a slurry property. For example, $\rho_1{}^*$ refers to the density of slurry phase 1 (which contains fluid phase 1 and the proppant carried by fluid phase 1), whereas $\rho_1$refers to the density of fluid phase 1.To make the derivations as general as possible, we define the following volumes of fluid and proppant:

$$\begin{cases} V_j = \text{Volume of fluid phase j} \\ V_{p,j} = \text{Volume of proppant included in slurry phase j} \\ V_j^* = V_j + V_{p,j} = \text{Volume of slurry phase j (including proppant)} \\ V_{fluid} = \sum_{j=1}^{NP} V_j = \text{Total volume of fluid} \\ V_p = \sum_{j=1}^{NP} V_{p,j} = \text{Total volume of proppant} \\ V_T = \sum_{j=1}^{NP} V_j^* = V_{fluid} + V_p = \text{Total volume of fluid including proppant} \end{cases} \tag{2.1}$$

By definition, the saturations of the fluid and slurry phase *j* are given by:

$$S_j = \frac{V_j}{V_{fluid}} = \frac{V_j}{\sum_{j=1}^{NP} V_j} \quad \text{and} \quad S_j^* = \frac{V_j^*}{V_T} = \frac{V_j^*}{\sum_{j=1}^{NP} V_j^*} \tag{2.2}$$

In Eq. 2.2, S_j refers to the saturation of fluid phase *j* on a fluid volume basis, and $S_j{}^*$ refers to the saturation of slurry phase *j* on a slurry volume basis (fluid + proppant). In addition, the fracturing fluid may transport proppant. The total volume concentration of proppant is denoted by *c*, which corresponds to:

$$c = \frac{V_p}{V_T} = \frac{\sum_{j=1}^{NP} V_{p,j}}{\sum_{j=1}^{NP} V_j^*} \tag{2.3}$$

We define γ_j as the proppant concentration (volume fraction) in slurry phase j. To remain as general as possible, we assume that the proppant does not have to be uniformly distributed among the phases, and $K\gamma$ is defined as the ratio of the proppant concentration in the two phases:

$$\gamma_j = \frac{V_{p,j}}{V_j^*} \quad \text{and} \quad K_\gamma = \frac{\gamma_2^*}{\gamma_1^*} \tag{2.4}$$

2.1.3 Material Balances

Using the definitions provided in Eqs. 2.1 to 2.4, several material balances yield useful relationships that are used in the derivations of the constitutive equations. By construction, the sum of the saturations on a fluid and slurry volume basis adds up to one:

$$\sum_{j=1}^{NP} S_j = 1 \quad \text{and} \quad \sum_{j=1}^{NP} S_j^* = 1 \tag{2.5}$$

The volume concentration of proppant c is related to the proppant concentration γ_j in each slurry phase j as follows:

$$c = \frac{V_p}{V_T} = \frac{1}{V_T}\sum_{j=1}^{NP} V_{p,j} = \sum_{j=1}^{NP} \frac{V_j^*}{V_T}\frac{V_{p,j}}{V_j^*} = \sum_{j=1}^{NP} S_j^* \gamma_j^* \tag{2.6}$$

The saturation S_j^* (defined on a slurry volume basis) is related to the saturation S_j (defined on a fluid volume basis) as follows:

$$\begin{aligned} S_j^* &= \frac{V_j^*}{V_T} = \frac{V_j + V_{p,j}}{V_T} = \frac{V_j}{V_{fluid}}\frac{V_{fluid}}{V_T} + \frac{V_j^*}{V_T}\frac{V_{p,j}}{V_j^*} = S_j(1-c) + S_j^*\gamma_j \\ \Rightarrow \quad S_j^* &= S_j\left(\frac{1-c}{1-\gamma_j}\right) \end{aligned} \tag{2.7}$$

2.1.3 Main Variables for Fluid Composition

The fracturing fluid contains *NC* components that may partition in both phases, and the component split between phases is governed by local thermodynamic equilibrium. As seen in Fig. 2.2, we define ω_{ij} as the mass fraction of component *i* in phase *j*, and z_i as the overall mass fraction of component *i*. We also use the conventional notation for liquid-vapor equilibrium, in which x_i and y_i are the mass fractions of component *i* in the liquid and gas phases, respectively. For a two-phase fluid, the overall mass fraction of component *i* is given by:

$$z_i = \frac{\sum_{j=1}^{NP} \rho_j S_j \omega_{ij}}{\sum_{j=1}^{NP} \rho_j S_j} = \frac{x_i \rho_1 S_1 + y_i \rho_2 S_2}{\rho_1 S_1 + \rho_2 S_2} \tag{2.8}$$

Fig. 2.3 provides an example of compositional calculations for 0.7-quality CO_2 foam. By definition, the saturation of the gas phase is 0.7, and the saturation of the liquid phase is 0.3. The water component does not partition in the gas phase, so y_1=0; CO_2 is the only component in the gas phase, so y_2=1. Under the given conditions of pressure and temperature, the solubility of CO_2 in water is 6% by mass, so x_1=0.94 and x_2=0.06. Under these conditions, the density of the liquid and gas phases is 63 lbm/ft^3 and 51 lbm/ft^3, respectively. Using Eq. 3.8, the overall mass fraction of water is 0.325, and the overall mass fraction of CO_2 is 0.675.

2.2 FLOW EQUATIONS

The flow equations relate the flow of the fluid in the fracture to the fluid pressure gradients. The fracturing fluid is assumed to flow between essentially parallel porous walls. Fluid flow is idealized as that of 2D, laminar, compressible, power-law fluid. Each phase is assumed to behave locally as a power-law fluid with known power-law index and consistency. This assumption is not a significant limitation as different power-law parameters can be assigned at each node. These parameters are known functions of polymer loading, temperature, proppant concentration, pH, shear history, surfactant conditions, and other factors. Any *a priori* model that describes changes in *n* and *K* can easily be incorporated into the fracture model since we use the local values of *n* and *K*.

2.2.1 Slurry Flow

We first derive the velocity profile for a laminar, single-phase, compressible, power-law fluid subject to a given pressure distribution. The fluid is flowing in a pseudo steady-state manner. Because the fracture is much thinner along the *z*-axis (fracture width), the velocity gradients are negligible along the *x* and *y*-axis. The power-law fluid rheology is characterized by:

$$\mu = K\sqrt{\left(\frac{\partial v_x}{\partial z}\right)^2 + \left(\frac{\partial v_y}{\partial z}\right)^2}^{n-1} \tag{2.9}$$

We also assume that the flow is symmetric and that there is no slippage at the fracture wall. The Navier-Stokes equation governing fluid flow between two parallel plates is solved along the *x* and *y*-axis to obtain the flowrate per unit fracture height:

$$\begin{cases} q_x = -\dfrac{n}{2n+1}K^{-1/n}\left(\left(\dfrac{\partial P}{\partial x}\right)^2 + \left(\dfrac{\partial P}{\partial y} + \rho g\right)^2\right)^{\frac{1-n}{2n}}\left(\dfrac{w^{\frac{2n+1}{n}}}{2^{\frac{n+1}{n}}}\right)\times\left(\dfrac{\partial P}{\partial x}\right) \\ q_y = -\dfrac{n}{2n+1}K^{-1/n}\left(\left(\dfrac{\partial P}{\partial x}\right)^2 + \left(\dfrac{\partial P}{\partial y} + \rho g\right)^2\right)^{\frac{1-n}{2n}}\left(\dfrac{w^{\frac{2n+1}{n}}}{2^{\frac{n+1}{n}}}\right)\times\left(\dfrac{\partial P}{\partial y} + \rho g\right) \end{cases} \tag{2.10}$$

Eq. 2.10 expresses the flow rate per unit height of a compressible, single-phase, power-law fluid. For a single-phase Newtonian fluid, Eq. 2.10 reduces to the traditional equation for fluid flow in a slot of narrow width:

$$q_x = -\frac{w^3}{12\mu}\left(\frac{\partial P}{\partial x}\right) \quad ; \quad q_y = -\frac{w^3}{12\mu}\left(\frac{\partial P}{\partial y} + \rho g\right) \tag{2.11}$$

The presence of multiple phases alters the flow behavior because: (1) each phase may have a different rheology; (2) the no-slip boundary at the fracture wall is not valid at the interfaces between phases; (3) each phase does not occupy the full fracture volume; and (4) each phase may interfere with its neighbors. The rheology of each slurry phase depends on both the fluid rheology and the proppant concentration within that phase. We assume that the phases do not interfere, so each phase may be

seen as a fluid flowing in a separate conduit, of which the diameter is proportional to the phase saturation. Also, we assume that the slippage that may occur at the interfaces between phases does not significantly alter fluid flow. Under these assumptions, the flow rate of the slurry phase *j* becomes:

$$\begin{cases} q_{j,x}^{*} = -S_j^{*} \dfrac{n_j}{2n_j+1} K_j^{-1/n_j} \left(\left(\dfrac{\partial P}{\partial x} \right)^2 + \left(\dfrac{\partial P}{\partial y} + \rho_j^{*} g \right)^2 \right)^{\frac{1-n_j}{2n_j}} \left(\dfrac{w^{\frac{2n_j+1}{n_j}}}{2^{\frac{n_j+1}{n_j}}} \right) \times \left(\dfrac{\partial P}{\partial x} \right) \\ q_{j,y}^{*} = -S_j^{*} \dfrac{n_j}{2n_j+1} K_j^{-1/n_j} \left(\left(\dfrac{\partial P}{\partial x} \right)^2 + \left(\dfrac{\partial P}{\partial y} + \rho_j^{*} g \right)^2 \right)^{\frac{1-n_j}{2n_j}} \left(\dfrac{w^{\frac{2n_j+1}{n_j}}}{2^{\frac{n_j+1}{n_j}}} \right) \times \left(\dfrac{\partial P}{\partial y} + \rho_j^{*} g \right) \end{cases} \tag{2.12}$$

In Eq. 2.12, the rheology parameters *n* and *K* have subscripts *j* since each phase may have different values. The superscript * denotes a quantity proper to a slurry phase, not just to a fluid phase. Eq. 2.12 may be written in a more compact form by using the parameter A_j^{*}, which relates the flow rate per unit height of the phase *j* to the pressure gradient:

$$\begin{cases} A_j^{*} = -\dfrac{n_j}{2n_j+1} K_j^{\frac{-1}{n_j}} \left(\dfrac{w^{\frac{2n_j+1}{n_j}}}{2^{\frac{n_j+1}{n_j}}} \right) \left[\left(\dfrac{\partial P}{\partial x} \right)^2 + \left(\dfrac{\partial P}{\partial y} + \rho_j^{*} g \right)^2 \right]^{\frac{1-n_j}{2n_j}} \\ q_{j,x}^{*} = A_j^{*} S_j^{*} \left(\dfrac{\partial P}{\partial x} \right) \quad ; \quad q_{j,y}^{*} = A_j^{*} S_j^{*} \left(\dfrac{\partial P}{\partial y} + \rho_j^{*} g \right) \end{cases} \tag{2.13}$$

The total flowrate of the mixture per unit height is the sum of the contributions of the *NP* phases, as seen in Eq. 2.14:

$$\begin{cases} q_x^* = \sum_{j=1}^{NP} q_{j,x}^* = \sum_{j=1}^{NP} A_j S_j^* \dfrac{\partial P}{\partial x} \\ q_y^* = \sum_{j=1}^{NP} q_{j,y}^* = \sum_{j=1}^{NP} A_j S_j^* \left(\dfrac{\partial P}{\partial y} + \rho_j g \right) \end{cases} \tag{2.14}$$

2.2.2 Proppant Flow

Because of proppant settling (in the *y*-direction) and proppant retardation (in the *x*-direction), the fluid and proppant contained in each slurry phase may travel at different velocities. We introduce retardation factors in the *x* and *y*-directions to describe the relative motion of the proppant with respect to the slurry ($\lambda_{j,x}$ and $\lambda_{j,y}$, respectively). These retardation factors are phase-dependent. They are introduced so that proppant fluxes can be expressed in terms of slurry fluxes, as shown in Eq. 2.15:

$$\begin{cases} q_{p,j,x} = \gamma_j \lambda_{j,x} q_{j,x}^* \\ q_{p,j,y} = \gamma_j \lambda_{j,y} q_{j,y}^* \end{cases} \quad where \quad \lambda_{j,x} = k_{ret,j} \quad and \quad \lambda_{j,y} = \left(1 - \frac{V_{set} w}{q_{j,y}^*} \right) \tag{2.15}$$

Here, k_{ret} refers to the proppant retardation effect and V_{set} refers to the settling velocity. The settling is due to the density contrast between the proppant and the carrying fluid. As a first approximation, the settling velocity is calculated with Stokes' law:

$$V_{Stokes} = \frac{\left(\rho_p - \rho_f \right) g d_p^2}{18 \mu} \tag{2.16}$$

Stokes' law is valid for low Reynolds number flows in an unbounded wall. Additional corrections are needed to account for the effects of fracture walls, inertia, and proppant concentration (Gadde *et al*. 2004). We assume that these corrections are independent of each other, as seen in Eq. 2.17:

$$V_{set} = V_{Stokes} \times f(\mathrm{Re})\, f(c)\, f(w) \quad \begin{cases} f(\mathrm{Re}) = \dfrac{0.3736\mu^{0.57}}{\rho_f^{0.29}\left(\rho_p - \rho_f\right)^{0.29} d_p^{0.86}} \\ f(c) = 1 - 4.8c + 8.8c^2 - 5.9c^3 \\ f(w) = 1 - 1.563\left(\dfrac{d_p}{w}\right) + 0.563\left(\dfrac{d_p}{w}\right)^2 \end{cases} \tag{2.17}$$

Additionally, the proppant may experience a velocity reduction in the *x*-direction. Gadde *et al*. (2004) and Liu (2006) proposed correlations accounting for the effect of fracture walls and proppant concentration on proppant retardation:

$$\begin{cases} \dfrac{1}{w_c^2} = 1.411\left(\dfrac{1}{d_p^2} - \dfrac{1}{w^2}\right) c^{0.8} \\ k_{ret} = 1 + \left(\dfrac{d_p}{w_c}\right) - 2.02\left(\dfrac{d_p}{w_c}\right)^2 \end{cases} \tag{2.18}$$

2.2.3 Fluid Flow

Because of proppant settling and retardation, the fluid phase has a different velocity than its slurry counterpart. The mass flux of slurry phase *j* is equal to the sum of the associated fluid and proppant mass fluxes:

$$\rho_j^* q_{j,x}^* = \rho_j q_{j,x} + \rho_p q_{p,j,x} \quad \Rightarrow \quad q_{j,x} = q_{j,x}^* \left(\frac{\rho_j^*}{\rho_j} - \frac{\rho_p}{\rho_j} \gamma_j \lambda_{j,x} \right) \tag{2.19}$$

Similar derivations may be performed in the *y*-direction to define the fluid fluxes in terms of slurry fluxes:

$$\begin{cases} q_{j,x} = q_{j,x}^* \left(\left(1 - \gamma_j\right) + \dfrac{\rho_p}{\rho_j} \gamma_j \left(1 - \lambda_{j,x}\right) \right) \\ q_{j,y} = q_{j,y}^* \left(\left(1 - \gamma_j\right) + \dfrac{\rho_p}{\rho_j} \gamma_j \left(1 - \lambda_{j,y}\right) \right) \end{cases} \tag{2.20}$$

The fluid flow properties of the slurry, proppant, and fluid phases have now been derived, and will be used in the subsequent derivations of the transport equations. Table 2.1 shows how the different properties are related. Specifically, the proppant and fluid fluxes are expressed in terms of the slurry fluxes.

2.3 PRESSURE EQUATION (OVERALL MASS BALANCE)

The pressure equation is an overall continuity equation that expresses the conservation of mass for compressible, multi-phase, slurry mixtures. The overall mass flux is the sum of the contributions of the *NP* slurry phases. Assuming that these contributions are linearly independent, the continuity equation is given by:

$$\frac{\partial}{\partial t}\left(w\bar{m}_T\right)+\nabla.\left(\sum_{j=1}^{NP}\vec{q}_j^{\,*}\rho_j^*\right)+\sum_{j=1}^{NP}q_{L,j}\rho_j=0 \tag{2.21}$$

In Eq. 2.21, the accumulation term includes the total slurry mass flowing through the fracture on a total volume basis, which is given by:

$$\bar{m}_T=\frac{m_T^*}{V_T}=\frac{m_p+m_f}{V_T}=\rho_p c+\left(1-c\right)\sum_{j=1}^{NP}\rho_j S_j \tag{2.22}$$

The total slurry mass flowing through the fracture on a total volume basis equals the density of the slurry mixture; hence, Eq. 2.22 may be expressed as:

$$\bar{m}_T=\rho_T^*=\sum_{j=1}^{NP}\rho_j^* S_j^* \tag{2.23}$$

In addition, we assume that the fluid-loss rate is phase-dependent and follows Carter's filtration model (Carter 1957). Inserting Eqs. 2.13 and 2.23 into Eq. 2.21, the pressure equation takes the form of a diffusivity equation:

$$\frac{\partial}{\partial t}\left\{w\left(\sum_{j=1}^{NP}\rho_j^* S_j^*\right)\right\}+\frac{\partial}{\partial x}\left\{\left(\sum_{j=1}^{NP}\rho_j^* A_j^* S_j^*\right)\frac{\partial P}{\partial x}\right\}+\frac{\partial}{\partial y}\left\{\left(\sum_{j=1}^{NP}\rho_j^* A_j^* S_j^*\right)\frac{\partial P}{\partial y}\right\}$$
$$+\frac{\partial}{\partial y}\left\{\left(\sum_{j=1}^{NP}\rho_j^{*2} A_j^* S_j^*\right)g\right\}+\sum_{j=1}^{NP}\frac{2C_{w,j}\rho_j}{\sqrt{t-\tau}}=0 \qquad (2.24)$$

In Eq. 2.24, the first term is the accumulation term; the second is the convective flux along the *x*-direction; the third is the convective flux along the *y*-direction; the fourth is the gravity contribution; and the fifth is the fluid-loss rate to the rock formation. In our definition of the fluid-loss rate, the leak-off coefficient is phase-dependent ($C_{w,j}$). This coefficient is a function of the fluid saturation, but it does not have to be proportional to the fluid saturation. Because of this assumption, the fluid saturation does not appear in the fluid-loss term, contrary to the model proposed by Friehauf and Sharma (2009). Any *a priori* model that describes changes in $C_{w,j}$ can easily be incorporated into the fracture model since we use local values at each node.

Initial conditions (ICs) and boundary conditions (BCs) are required to solve this partial differential equation (PDE). Initially, the fluid pressure is equal to the fracture initiation pressure, which is slightly higher than the minimum horizontal stress. For the BCs, the pumping rate per unit height is specified along the perforated interval ($\partial\Omega_p$). No fluid flows out of the fracture front ($\partial\Omega_f$) or from the non-perforated section of the wellbore ($\partial\Omega_c$); thus, we use no-flow BCs along these intervals:

$$\underline{ICs}: P=\sigma_{h\min}+\Delta P_{toughness} \quad over\ \Omega \qquad (2.25)$$

$$\underline{BCs}: \begin{cases} A^*\dfrac{\partial P}{\partial n}=A^*\dfrac{\partial P}{\partial x}=\left(q_x\right)_{inj} & on\ \partial\Omega_p \\ \dfrac{\partial P}{\partial n}=0 & on\ \partial\Omega_f\ and\ \partial\Omega_c \end{cases} \qquad (2.26)$$

Because only natural (Neumann) BCs are specified and because the pressure equation only involves pressure gradients, the equation is singular and the solution is determined within a constant. In other words, a solution of Eq. 2.24 plus an arbitrary constant is also a solution of that equation. The arbitrary constant is determined from the requirement that the fracture propagates at each time step. The net pressure at the perforations is adjusted so that the fluid pressure, and therefore the stress intensity

factor, is high enough to overcome a critical value (fracture toughness) somewhere along the fracture tip. This method is significantly different from 2D and pseudo 3D fracturing models, which essentially prescribe that the net pressure is zero at a pre-defined location along the tip.

The increase in fracture mass must equal the mass of fluid pumped minus the mass of fluid that leaked off. This overall conservation of mass is enforced by a so-called compatibility equation. The time step (Δt^n) used for solving Eq. 2.24 is calculated from this condition. Eq. 2.27 is a necessary condition to the existence of a solution:

$$\Delta t^n = \frac{\Delta m_{fracture} + \Delta m_{leakoff}}{\dot{m}_{pumped}} \tag{2.27}$$

Δt^n denotes the time step increment; $\Delta m_{fracture}$ is the change in fracturing fluid mass during Δt^n; $\Delta m_{leakoff}$ is the mass of fluid that leaked off during Δt^n; and $\dot{m}_{pumped}$ is the mass flow rate imposed at the perforations. A similar compatibility condition was derived for incompressible fluids by Gu (1987) and Yew (1997) to ensure that the overall volume conservation was satisfied. Because the fracturing fluid is now compressible, the new time step requirement is derived from the overall mass conservation.

2.4 PROPPANT TRANSPORT EQUATION

Similarly to the derivation of the pressure equation, the derivation of the proppant transport equation intends to be as general as possible. No assumption is made regarding the proppant distribution within the two phases. The proppant remains incompressible, but the fluid transporting the proppant is compressible. We also assume that the proppant does not leak-off into the rock formation because of size exclusion. The continuity equation with respect to proppant is given by:

$$\frac{\partial}{\partial t}\left(w\bar{m}_p\right) + \nabla.\left(\sum_{j=1}^{NP}\rho_p\vec{q}_{p,j}\right) = 0 \tag{2.28}$$

In Eq. 2.28, the accumulation term includes the mass of proppant flowing through the fracture on a total volume basis, which is given by:

$$\bar{m}_p = \frac{m_p}{V_T} = \sum_{j=1}^{NP} S_j^* \bar{m}_{p,j} = \rho_p \left(\sum_{j=1}^{NP} S_j^* \gamma_j \right) = \rho_p c \tag{2.29}$$

Inserting Eqs. 2.15 and 2.29 into Eq. 2.28, the proppant transport equation takes the form of a convective-dominated equation:

$$\frac{\partial}{\partial t}(wc) + \frac{\partial}{\partial x}\left(\sum_{j=1}^{NP} \gamma_j \lambda_{j,x} A_j^* S_j^* \left(\frac{\partial P}{\partial x} \right) \right) + \frac{\partial}{\partial y}\left(\sum_{j=1}^{NP} \gamma_j \lambda_{j,x} A_j^* S_j^* \left(\frac{\partial P}{\partial y} + \rho_j^* g \right) \right) = 0 \tag{2.30}$$

Eq. 2.30 is not practical to solve for the proppant concentration c. A more useful formulation is obtained when expressing the convective terms as a function of the proppant concentration c. To do so, we assume that the proppant split K_γ is a known function, which is not limiting our model since we use the local value of K_γ at each node. Eq. 2.30 can be re-arranged as:

$$\frac{\partial}{\partial t}(wc) + \frac{\partial}{\partial x}\left(c\left(\frac{\lambda_{1,x} q_{1,x}^* + K_\gamma \lambda_{2,x} q_{2,x}^*}{K_\gamma + S_1^* (1 - K_\gamma)} \right) \right) + \frac{\partial}{\partial y}\left(c\left(\frac{\lambda_{1,y} q_{1,y}^* + K_\gamma \lambda_{2,y} q_{2,y}^*}{K_\gamma + S_1^* (1 - K_\gamma)} \right) \right) = 0 \tag{2.31}$$

If the proppant is uniformly distributed within the two phases, Eq. 2.31 becomes:

$$\frac{\partial}{\partial t}(wc) + \frac{\partial}{\partial x}\left(c\left(\lambda_{1,x} q_{1,x}^* + \lambda_{2,x} q_{2,x}^* \right) \right) + \frac{\partial}{\partial y}\left(c\left(\lambda_{1,y} q_{1,y}^* + \lambda_{2,y} q_{2,y}^* \right) \right) = 0 \tag{2.32}$$

Initially, the proppant concentration is zero. For the BCs, we assume that the proppant concentration at the perforations is equal to the injected concentration (along $\partial\Omega_p$). No proppant flows out of the fracture front ($\partial\Omega_f$) or from the non-perforated section of the wellbore ($\partial\Omega_c$):

$$\underline{ICs}: c = 0 \quad over\ \Omega \tag{2.33}$$

$$\underline{BCs}: \begin{cases} c = c_{inj} & on\ \partial\Omega_p \\ \dfrac{\partial c}{\partial n} = 0 & on\ \partial\Omega_f\ and\ \partial\Omega_c \end{cases} \tag{2.34}$$

In addition, we assume that the proppant is made of rigid spheres of equal diameter; therefore, the proppant concentration cannot exceed the maximum packing of spheres of equal diameter (0.52). This additional restriction is enforced numerically by locally spreading the excess proppant when the calculated concentration reaches the maximum value.

Although the derivations of the pressure and proppant transport equations both start from a continuity equation and share some similarities, the resulting equations differ fundamentally. The pressure equation is a diffusivity equation, which is an elliptic PDE, while the proppant transport equation is a convection-dominated equation, which combines parabolic and hyperbolic PDEs. The behavior, smoothness, and mathematical resolution of these equations are dramatically different. This is discussed in greater detail in Chapter 3.

2.4 COMPONENT TRANSPORT EQUATION

For single-phase fluids, no additional PDE is required to track the changes in fluid composition. The leak-off rate is phase-dependent, rather than component-dependent; therefore, the composition of a single-phase mixture of components remains uniform, and the solution of the component transport equations is trivial. However, the density, viscosity, and leak-off coefficient of the fluid changes over time and location, due to changes in pressure and temperature.

For multi-phase mixtures, each component can be transported by fluid phases flowing at different velocities. The fluid phase itself has a different velocity than its slurry counterpart because of proppant settling and retardation. As the proppant is slowing down, the fluid is accelerating with respect to the slurry. Also, the rate of fluid-loss may be different for each component depending on the component split between the two phases. The resolution of the component transport equations is thus required when using two-phase fluids. Because there are *NC* components, there are *NC* mass component transport equations. These equations may be written in terms of the mass fraction of each component (ω_{ij}), the overall mass fraction of each component (z_i), or the fluid saturation (S_1). These fundamental formulations are derived in this section.

2.4.1 Component Mass Fraction Formulation

The derivation of the component transport equation is mathematically similar to the derivation of the proppant transport equation. In fact, the proppant may be seen as an

additional component except the proppant is not subject to the thermodynamic equilibrium requirements. No assumption is made regarding the split of each component within the two phases. The split may be obtained from empirical data, known equilibrium values (also known as *K*-values), or from an equation of state. We assume that the leak-off coefficients are only phase-dependent, so each component is leaking off with its associated phase(s). Assuming that the fluxes are linearly independent, the continuity equation for component *i* is given by:

$$\frac{\partial}{\partial t}\left(w\bar{m}_i\right)+\nabla.\left(\sum_{j=1}^{NP}\vec{q}_j\bar{m}_{i,j}\right)+\sum_{j=1}^{NP}q_{L,i}\bar{m}_{i,j}=0 \tag{2.35}$$

In Eq. 2.35, the accumulation term includes the mass of component *i* flowing through the fracture on a total volume basis, which is given by:

$$\bar{m}_i=\sum_{j=1}^{NP}\bar{m}_{i,j}=\frac{1}{V_T}\sum_{j=1}^{NP}\omega_{ij}\rho_j V_j=\sum_{j=1}^{NP}\omega_{ij}\rho_j\left(1-\gamma_j\right)S_j^*=\left(1-c\right)\sum_{j=1}^{NP}\omega_{ij}\rho_j S_j \tag{2.36}$$

Inserting Eqs. 2.20 and 2.36 into Eq. 2.35, the component transport equation takes the form of a convection-dominated equation:

$$\begin{aligned}&\frac{\partial}{\partial t}\left(w\left(1-c\right)\left(\sum_{j=1}^{NP}\omega_{ij}\rho_j S_j\right)\right)+\frac{\partial}{\partial x}\left(\sum_{j=1}^{NP}\omega_{ij}\rho_j q_{j,x}\right)+\frac{\partial}{\partial y}\left(\sum_{j=1}^{NP}\omega_{ij}\rho_j q_{j,y}\right)\\&+\frac{2}{\sqrt{t-\tau}}\sum_{j=1}^{NP}C_{w,j}\omega_{ij}\rho_j=0\end{aligned} \tag{2.37}$$

Initially, the mass fraction of each component is uniform inside the fracture. The composition is governed by the initial conditions of pressure and temperature. Dirichlet BCs are imposed at the perforations and no-flux Neumann BCs are imposed everywhere else:

$$\underline{ICs}:\omega_{ij}=\omega_{ij}\left(P(t=0),T(t=0)\right)\quad over\ \Omega \tag{2.38}$$

$$\underline{BCs}: \begin{cases} \omega_{ij} = \omega_{ij,inj} & on\ \partial\Omega_p \\ \dfrac{\partial \omega_{ij}}{\partial n} = 0 & on\ \partial\Omega_f\ and\ \partial\Omega_c \end{cases} \tag{2.39}$$

2.4.2 Overall Component Mass Fraction Formulation

Using Eq. 2.37 to solve for the mass fraction ω_{ij} is not practical, as the summation over the multiple flux contributions prevents a direct time resolution of the equation. Moreover, flash calculations require knowledge of the overall mass fraction of each component in order to estimate the split within each phase. A more useful formulation is obtained when expressing the accumulation term in terms of the overall mass fraction z_i:

$$\begin{aligned} &\frac{\partial}{\partial t}\left(w(1-c)\left(\sum_{j=1}^{NP} \rho_j S_j \right) z_i \right) + \frac{\partial}{\partial x}\left(\sum_{j=1}^{NP} \omega_{ij} \rho_j q_{j,x} \right) + \frac{\partial}{\partial y}\left(\sum_{j=1}^{NP} \omega_{ij} \rho_j q_{j,y} \right) \\ &+ \frac{2}{\sqrt{t-\tau}} \sum_{j=1}^{NP} C_{w,j} \omega_{ij} \rho_j = 0 \end{aligned} \tag{2.40}$$

The ICs and BCs are similar to the ones introduced in the previous formulation:

$$\underline{ICs}: z_i = z_i(t=0) \quad over\ \Omega \tag{2.41}$$

$$\underline{BCs}: \begin{cases} z_{ij} = z_{i,inj} & on\ \partial\Omega_p \\ \dfrac{\partial z_i}{\partial n} = 0 & on\ \partial\Omega_f\ and\ \partial\Omega_c \end{cases} \tag{2.42}$$

The formulation given in Eq. 2.40 is particularly useful when using a time-explicit scheme. In that case, the new overall mass fraction may be used to perform flash calculations at the new conditions of pressure and temperature in order to estimate the component split between phases.

2.4.3 Saturation Formulation

The overall mass fraction formulation remains impractical when a time-implicit scheme is used. As discussed in Chapter 3, a time-implicit scheme is preferred to

solve transport equations, which are convection-diffusion PDEs. Eq. 2.40 may still be used with a time-implicit scheme, but a more stable formulation is obtained when solving for the fluid saturation. The convective fluxes are proportional to the fluid saturation, so solving for this variable tends to improve numerical stability. If there are more than two components, the first transport equation is solved in terms of S_1, and the subsequent transport equations are solved in terms of z_i or ω_{ij}.

Typically, foams are made of water and a second (energized) component, such as CO_2 and N_2 foams; and the water component does not partition in the gas phase. For N_2 foams, the liquid phase only contains water, and the gas phase only contains nitrogen. For CO_2 foams, the liquid phase contains water and some soluble CO_2, and the gas phase only contains CO_2. The amount of soluble CO_2 is predicted by the *K*-value K_2, which is the mass fraction of CO_2 in the gas phase divided by the mass fraction of CO_2 in the liquid phase. For N_2 foams, $1/K_2$ is equal to 0. Only one equation is thus required to know the fluid composition. Eq. 2.40 may be written in terms of the saturation S_1 as follows:

$$\frac{\partial}{\partial t}\left\{S_1 w(1-c)\left(1-\frac{1}{K_2}\right)\rho_1\right\}+\frac{\partial}{\partial x}\left\{S_1(1-c)\rho_1 A_1^* \alpha_{1,x}\left(1-\frac{1}{K_2}\right)\left(\frac{\partial P}{\partial x}\right)\right\}$$
$$+\frac{\partial}{\partial y}\left\{S_1(1-c)\rho_1 A_1^* \alpha_{1,y}\left(1-\frac{1}{K_2}\right)\left(\frac{\partial P}{\partial y}+\rho_1^* g\right)\right\}+\frac{2}{\sqrt{t-\tau}}\left\{\rho_1 C_{w,1}\left(1-\frac{1}{K_2}\right)\right\}=0 \qquad (2.43)$$
$$where\ \alpha_{j,x}=1+\frac{\rho_p}{\rho_j}\frac{\gamma_j}{1-\gamma_j}\left(1-\lambda_{j,x}\right)$$

The associated ICs and BCs are given by:

$$\underline{ICs}: S_1 = S_1(t=0) \quad over\ \Omega \qquad (2.44)$$

$$\underline{BCs}: \begin{cases} S_1 = S_{1,inj} & on\ \partial\Omega_p \\ \dfrac{\partial S_1}{\partial n}=0 & on\ \partial\Omega_f\ and\ \partial\Omega_c \end{cases} \qquad (2.45)$$

The mathematical solution of the component transport equations is similar to the solution of the proppant transport equation.

2.5 ENERGY BALANCE EQUATION

An energy balance equation models the heat transfers occurring between the fracturing fluid and the reservoir. A rigorous treatment of heat transfers becomes important, as changes in temperature affect the fracturing fluid's composition, density, and rheology. The derivation of the energy balance equation requires additional assumptions, which are given below.

2.5.1 Assumptions

The additional assumptions required to derive the energy balance equation are:

- The fluid and proppant temperatures are the same.
- The injection temperature is known over time.
- The temperature does not vary along the fracture width (z-axis).
- The axial conduction in the fluid is negligible when compared to the forced convection in both the x and y directions.
- The kinetic and viscous effects are negligible as compared to forced convection.
- The enthalpy of a fluid phase is only temperature-dependent.
- The heat capacity of each phase is constant.
- The reservoir fluid(s) and the rock have the same temperature.
- The heat capacity of the reservoir is constant and refers to the heat capacity of the fluid-filled reservoir.
- Heat is transferred between the reservoir and the slurry by conduction at the fracture walls. The conduction is affected by fluid leak-off.
- Heat is lost by convection at the fracture walls due to fluid leak-off.
- The contributions of each fluid phase and proppant can be summed up linearly.

These assumptions are also mentioned later, as they are needed in the subsequent derivations.

2.5.2 Combined Energy Fluxes

The combined energy flux encompasses the convective energy flux, the molecular heat flux, and the viscous heat flux. Axial conduction is negligible compared to convection in the x- and y-directions. Also, the slurry flow rate is small enough that

the heat dissipated by the viscous stresses and the kinetic energy is negligible; therefore, the combined energy flux of a given fluid becomes:

$$\vec{e} = \vec{q}_c + \left[\tilde{\tau}.\vec{q}\right]_x + \left(\frac{1}{2}\rho v^2 + \rho H\right)\vec{q} = \rho H\vec{q} \tag{2.46}$$

We assume that the enthalpy of a given fluid is not pressure-dependent and only temperature-dependent. Assuming that the heat capacity of the fluid remains constant, the change in enthalpy is given by:

$$H - H^0 = \int_{T^0}^{T} C_p dT + \int_{T^0}^{T}\left[V - T\left(\frac{\partial V}{\partial T}\right)_P\right]dP = \int_{T^0}^{T} C_p dT = C_p\left(T - T^0\right) \tag{2.47}$$

Using an adequate enthalpy reference, the combined energy flux becomes:

$$\vec{e} = \rho C_p T\vec{q} \tag{2.48}$$

We now assume that the slurry is composed of *NP* phases containing proppant. The proppant and the fluid are assumed to be at the same temperature. They form a pseudo single phase, whose thermal properties depend on both the proppant and the fluid thermal properties. We define an equivalent heat capacity for each slurry phase ($C^*_{p,j}$) as the weighted average of the slurry properties:

$$C^*_{p,j} = \frac{(1-c)C_{p,j}\rho_j + cC_{p,p}\rho_p}{(1-c)\rho_j + c\rho_p} = \frac{(1-c)C_{p,j}\rho_j + cC_{p,p}\rho_p}{\rho^*_j} \tag{2.49}$$

The total energy flux is the sum of the contributions of the *NP* slurry phases. Assuming that these contributions are independent, the combined energy flux becomes:

$$\vec{e} = \sum_{j=1}^{NP}\left(\rho H\vec{q}\right)_j = T\sum_{j=1}^{NP}\left(\rho^*_j C^*_{p,j}\vec{q}^*_j\right) \tag{2.50}$$

2.5.3 Heat Lost due to Leak-Off

Heat is lost to the rock formation through the fracture walls as the fluid leaks off. We assume that the conduction, the viscous effects and the kinetic effects are negligible compared to the convective heat transfers. The combined energy flux for a single-phase fluid leaking-off is defined in the direction normal to the fracture face as:

$$e_l = q_{c,l} + \left[\tau.q_l\right]_z + \left(\tfrac{1}{2}\rho v^2 + \rho H\right)q_l = \rho H q_l = \rho C_p T q_l \tag{2.51}$$

The fluid-loss rate follows Carter's model (1957). The total energy flux is the sum of the contributions of the *NP* slurry phases. Assuming that these contributions are independent, the energy flux for a multi-phase fluid leaking-off is given by:

$$e_l = \frac{2}{\sqrt{t-\tau}} T\left(\sum_{j=1}^{NP} \rho_j C_{p,j} C_j\right) \tag{2.52}$$

2.5.4 Heat Gained from the Reservoir

The reservoir formation heats the fluid by conduction. Conversely, the reservoir placed in contact with the fracture cools down over time. In some cases, this is precisely the objective of the stimulation treatment. As the reservoir cools down, the rock shrinks and becomes more brittle. This effect, referred to as *thermally-induced fracturing*, promotes fracture propagation.

Since the fracture is very narrow, we assume that the surface heat transfers only occur along the *z*-axis, which is normal to the fracture face. We also assume that there is no heat transfer occurring along the *y*-axis. This reduces the transient heat transfer problem to a pseudo 1D transient problem for each horizontal slice of the reservoir. The undisturbed reservoir temperature is a known function of depth, so the heat conduction flux remains dependent on depth. Fig. 2.4 shows a simplified schematic of the pseudo 1D problem. The undisturbed reservoir temperature is the temperature of the reservoir far away from the fracture. Mathematically, it is the temperature for *z* going to infinity.

If we neglect the convective effect of the fluid loss into the formation, the energy balance reduces to the transient 1D heat equation along the *z*-axis. This well-known problem has been solved analytically by many authors, including Carslaw and Jaeger (1959), and Hasan and Kabir (2002). The conductive heat flux is proportional to the

temperature difference between the undisturbed reservoir temperature and the temperature of the rock directly in contact with the fracture. The conductive heat flux per unit height is given by:

$$Q_{cond}(x,y,t) = 2\sqrt{\frac{K_R \rho_R C_{pR}}{\pi t}}\left(T_f(x,y,t) - T_R(y)\right) \tag{2.53}$$

Eq. 2.53 is valid for a purely conductive problem. This is not the case here because some of the fracturing fluid leaks off into the rock formation. Additional correction factors have been identified to model the reduction of heat conduction associated with leak-off (Meyer 1989). This correction, referred to as heat blockage, encompasses both the cooling of the reservoir due to fluid leak-off and the additional thermal resistance offered by the fluid that has invaded the formation:

$$Q_{cond}(x,y,t) = 2\sqrt{\frac{K_R \rho_R C_{pR}}{\pi t}}\left(T_f(x,y,t) - T_R(y)\right)\psi(C)\Phi(C) \tag{2.54}$$

The two correction terms are time-dependent. They have been identified by Meyer (1989) as:

$$\begin{cases} \psi(C) = \exp(-\lambda^2) - \sqrt{\pi}\lambda erfc(\lambda) \\ \Phi(C) = \sqrt{\pi}\beta \exp(\beta^2) erfc(\beta) \end{cases} \quad where \quad \begin{cases} \lambda = \dfrac{C}{2\sqrt{\alpha_R}} \dfrac{(\rho Cp)_{fL}}{(\rho Cp)_R} \dfrac{\rho_f}{\rho_{fL}} \\ \beta = \dfrac{\beta_o \sqrt{1 - t/\tau}}{w / w_{\max}} \\ \beta_o = \dfrac{Nuk_f \sqrt{\alpha_R t}}{wk_R \Psi(\lambda)} \end{cases} \tag{2.55}$$

2.5.5 Energy Balance Equation

The general expression of the unsteady energy balance equation is given by:

$$\frac{\partial}{\partial t}\left(w\left(\rho H\right)_T\right) + \nabla.\left(\vec{e}\right) + e_l - Q_{cond} = 0 \tag{2.56}$$

For a multi-phase slurry mixture, the accumulation term is defined as a linear combination of enthalpy terms:

$$w(\rho H)_T = Tw\left(\sum_{j=1}^{NP} S_j^* \rho_j^* C_{p,j}^*\right) \tag{2.57}$$

Inserting Eqs. 2.50, 2.52, 2.54, and 2.57 into Eq. 2.56, the unsteady energy balance equation takes the form of a convective-dominated equation:

$$\begin{aligned}&\frac{\partial}{\partial t}\left\{Tw\left(\sum_{j=1}^{NP} S_j^* \rho_j^* C_{p,j}^*\right)\right\} + \frac{\partial}{\partial x}\left\{T\left(\sum_{j=1}^{NP} q_{j,x}^* \rho_j^* C_{p,j}^*\right)\right\} + \frac{\partial}{\partial y}\left\{T\left(\sum_{j=1}^{NP} q_{j,y}^* \rho_j^* C_{p,j}^*\right)\right\} \\ &+ \frac{2}{\sqrt{t-\tau}}\left\{T\left(\sum_{j=1}^{NP} \rho_j C_{p,j} C_{w,j}\right)\right\} + \frac{2}{\sqrt{t-\tau}}\sqrt{\frac{K_R \rho_R C_{p,R}}{\pi}}\psi(C)\Phi(C)\left(T - T_R\right) = 0\end{aligned} \tag{2.58}$$

Initially, the temperature equals the temperature of the fluid injected at the perforations. As for the proppant transport equation, Dirichlet BCs are imposed at the perforations and no-flux Neumann BCs are imposed everywhere else:

$$\underline{ICs}: T = T_{inj}\left(t = 0\right) \quad over\ \Omega \tag{2.59}$$

$$\underline{BCs}: \begin{cases} T = T_{inj} & on\ \partial\Omega_p \\ \dfrac{\partial T}{\partial n} = 0 & on\ \partial\Omega_f\ and\ \partial\Omega_c \end{cases} \tag{2.60}$$

2.6 FRACTURE MECHANICS

2.6.1 Fracture Opening Equation

Assuming an isotropic, homogeneous, elastic medium, the 3D elasticity problem is essentially the Navier-Cauchy problem relating strains to applied stresses. Under these assumptions, the problem reduces to the tensile mode-I fracture opening equation. For planar fractures, the fracture opening equation is a boundary integral equation that relates the pressure on the crack faces to the crack opening. A boundary integral formulation is required since a local stress applied at a given location

deforms the entire surface of the elastic body. The integral equation was derived independently by Kossecka (1971), Bui (1977), and Weaver (1977):

$$-P(x,y)+\sigma_{h\min}(x,y)=\frac{G}{4\pi(1-\nu)}\int_{\Omega}\left[\frac{\partial}{\partial x}\left(\frac{1}{r}\right)\frac{\partial w(x,y)}{\partial x'}+\frac{\partial}{\partial y}\left(\frac{1}{r}\right)\frac{\partial w(x,y)}{\partial y'}\right]d\Omega \quad \text{where } r=\sqrt{\left(x'-x\right)^2+\left(y'-y\right)^2} \tag{2.61}$$

Eq. 2.61 gives the width of the fracture for a known load distribution. The load is defined locally as the difference between the fluid pressure in the fracture and the minimum horizontal stress acting on the fracture face. Additionally, the fracture width is zero along the fracture front:

$$\underline{BC}: w=0 \quad on\ \partial\Omega_f \tag{2.62}$$

2.6.2 Criterion for Fracture Propagation

The fracture propagation criterion follows the theory of linear elasticity for a brittle material subject to tensile (mode-I) opening. The theory involves the computation of the mode-I stress intensity factor (K_I), which is used to predict the stress stare (or "stress intensity") near the tip of the crack caused by a remote load. The expression of the stress intensity factor depends on the mode of failure and the geometry of the problem. For mode-I opening of a 3D planar crack, K_I is given by:

$$K_I(x,y)=\frac{G}{4(1-\nu)}\sqrt{\frac{2\pi}{r_{tip}(x,y)}}w(x,y) \tag{2.63}$$

In Eq. 2.63, $r_{tip}(x,y)$ is the minimum distance between the node of interest located at (x, y) and the fracture front. A fracture propagation criterion controls the advance of the crack front, by relating the intensity of the stress state ahead of the crack to the critical intensity necessary for tensile opening of the rock. Front propagation is proportional to the difference between K_I and the rock toughness (K_{IC}), as established by Mastrojannis *et al.* (1979). The criterion for fracture propagation is applied locally as:

$$\Delta d = \max\left(\Delta d_{\max} \left(\frac{K_I - K_{IC}}{K_{IC}} \right); 0 \right) \tag{2.64}$$

Eq. 2.64 ensures that a given location along the fracture boundary is not propagating artificially if the local stress intensity factor does not exceed the critical value. The direction of displacement is not prescribed in advance, and the fracture shape evolves freely in all the directions contained in the propagation plane. This 3D formulation significantly differs from 2D mechanical models, which require that the fracture boundary in the plane of propagation be specified in advance.

2.7 OVERVIEW OF THE MATHEMATICAL PROBLEM

The system of PDEs presented in this chapter constitutes the core of this research work. This section addresses the completeness of the mathematical problem and the main complexities associated with the resolution of the fundamental system of PDEs.

2.7.1 Completeness of the Mathematical Problem

Before attempting to solve the mathematical problem, it is critical to ensure that the problem is well-posed. This is (usually) the case when the number of independent variables equals the number of independent equations. At a given time, the fracture problem is fully solved if we can compute the fracture geometry, fluid composition, fluid temperature, fluid pressure, and proppant distribution. The fluid composition is characterized by the saturation, density, and component mass fraction(s) in each phase. As seen on the left side of Table 2.2, the number of independent variables equal (4+3*NP*+*NC***NP*) for a fluid containing *NC* components distributed in *NP* phases. Additional variables are dependent variables that are directly defined from this set of independent unknowns. For example, the overall mass fraction of each component (z_i) is a dependent variable defined by Eq. 2.8.

Thus far, we have derived five different PDEs governing pressure, proppant distribution, component mass fraction, temperature, and fracture width. In addition, the local thermodynamic equations consist of: (1) *NP* equations of states governing the density of each fluid phase, (2) *NC**(*NP*-1) fugacity equations ensuring thermodynamic equilibrium for each component, and (3) *NP* continuity equations ensuring that the sum of the mass fractions in a given phase equals one. For some of these equations, we presented multiple formulations. For example, Section 2.4

presented equations that may be solved for the mass fraction of each component in each phase (ω_{ij}), for the overall mass fraction of each component (z_i), or for the fluid saturation (S_1). In fact, there is infinity of dependent equations that could be derived from the above equations. For instance, the pressure equation is simply the sum of all the component mass fractions equations and the proppant transport equation.
As seen on the right side of Table 2.2, the degree of freedom of the equations equals (4+3*NP*+*NC***NP*) for a fluid containing *NC* components distributed in *NP* phases.

The set of equations presented here constitutes a complete set of independent equations, for which the number of independent equations equals the number of independent variables. The compositional fracture problem is well-posed and a numerical solution is possible.

2.7.2 Complexity of the Mathematical Problem

Solving this set of PDEs is a challenging task for five main reasons:

- The PDEs are of different classes (elliptic versus parabolic-hyperbolic);
- There is a strong coupling between the PDEs;
- Several of the PDEs are non-linear;
- This is a moving-boundary problem; and
- The fracture opening equation is singular.

These complexities have hindered the development of fracturing codes for many years, and they still represent a challenging task today.

2.7.2.1 Different Classes of PDEs

A PDE's class plays a fundamental role in the behavior of the solutions, particularly in determining the smoothness of the solutions. The nature of the appropriate initial and boundary conditions depend on the PDE's class. Typically, solutions of elliptic PDEs are as smooth as the coefficients allow. For example, solutions of Laplace's equation are analytic within the domain where they are defined, but solutions may assume boundary values that are not smooth. The pressure equation is an elliptic PDE. The dominant term is the spatial derivative of second order, which smoothes out the solution within the interior of the domain. The variable of interest (pressure) does not appear in the accumulation term, which is viewed as a source term.

Alternatively, the accumulation term plays a critical role in parabolic PDEs. Solutions of parabolic PDEs smooth out as the time variable increases. The absence of a dominant diffusion term promotes the formation of sharp fronts and discontinuities, which may cause the solution to oscillate. The proppant transport, component transport, and temperature equations are convection-dominated PDEs; therefore, they are more prone to oscillations. In general, spatial derivatives of even order (2nd order in our case) dampen oscillations while derivatives of odd order (1st order in our case) promote oscillations. The numerical treatment of these equations is significantly different.

2.7.2.2 Strong Coupling between the PDEs

The numerous inter-dependences between the PDEs further complicate the resolution of the set of PDEs. For instance, the pressure equation and the fracture opening equation are tightly coupled. The presence of the $1/w^3$ term in the pressure equation makes the equation highly sensitive to changes in fracture width. As discussed in Chapter 3, a complex iterative scheme is required to solve these coupled equations.

2.7.2.3 Non Linearity

Several of the constitutive PDEs are nonlinear. The convective term in the pressure equation involves the square of the pressure gradient, which introduces a non-linearity. Similarly, the convective flux in the proppant transport equation is also a function of the proppant concentration. The non-linearity is more subtle in the energy balance equation, as the density is itself a function of temperature. The use of iterative schemes reduces some of the numerical instabilities associated with the non-linearity of the PDEs.

2.7.2.4 Moving - Boundary Problem

Perhaps the most defining feature of the fracture propagation problem is that it is a moving-boundary problem. This characteristic is highly unusual in most engineering disciplines. In mathematics, a moving-boundary (or "free-boundary") problem is a PDE to be solved for both an unknown function and an unknown domain Ω. The segment $\partial\Omega$ of the boundary of Ω which is not known at the outset of the problem is the free boundary.

The classic example is the melting of ice. Given a block of ice, we can solve the heat equation given appropriate initial and boundary conditions to determine its temperature. However, if in any region the temperature is greater than the melting point of ice, this domain will be occupied by liquid water instead. This problem is the classical Stefan problem, which aims to describe the temperature distribution in a homogeneous medium undergoing a phase change. This is accomplished by solving the heat equation imposing the initial temperature distribution on the whole medium, and a particular boundary condition, the Stefan condition, on the evolving boundary between its two phases. The location of the ice/liquid interface is controlled dynamically by the solution of the PDE. This evolving boundary is an unknown surface that constitutes a fundamental part of the solution. Similarly, the fracture propagation problem is a moving-boundary problem, and the primary objective of the model is to track the evolution of the boundary (fracture shape) over time.

2.7.2.5 Singularities

Finally, the fracture opening equation becomes singular as r converges to zero, and thus $1/r$ diverges to infinity. As discussed by Yew (1997), this boundary integral equation is weakly singular, and it converges only in a Cauchy principal value sense. The singularity is overcome by using an appropriate coordinate transformation in the finite element formulation of the problem and by using specific elements along the fracture tip. However, the use of specific elements to perform the stress-intensity calculations makes the propagation criterion intrinsically grid-dependent (Economides and Nolte 2000). The methods used to overcome these singularities are addressed in Chapter 3.

Table 2.1: Main properties defining slurry, proppant, and fluid phases.

Properties	Slurry Phase	Proppant Phase	Fluid Phase
Density	$\rho_j^* = \rho_p \gamma_j + \rho_j \left(1-\gamma_j\right)$	ρ_p	ρ_j
Saturation	S_j^*	γ_j	$S_j = S_j^* \left(\frac{1-\gamma_j}{1-c}\right)$
Flux (*x*-axis)	$q_{j,x}^* = A_j^* S_j^* \left(\frac{\partial P}{\partial x}\right)$	$q_{p,j,x} = q_{j,x}^* \gamma_j \lambda_{j,x}$	$q_{j,x} = q_{j,x}^* \left(\left(1-\gamma_j\right) + \frac{\rho_p}{\rho_j}\gamma_j\left(1-\lambda_{j,x}\right)\right)$
Flux (*y*-axis)	$q_{j,y}^* = A_j^* S_j^* \left(\frac{\partial P}{\partial y} + \rho_j^* g\right)$	$q_{p,j,y} = q_{j,y}^* \gamma_j \lambda_{j,y}$	$q_{j,y} = q_{j,y}^* \left(\left(1-\gamma_j\right) + \frac{\rho_p}{\rho_j}\gamma_j\left(1-\lambda_{j,y}\right)\right)$

Table 2.2: List of independent variables and equations. The problem is well-posed, as the number of independent equations equals the number of independent variables.

Unknowns	Number of Independent Variables	Equations	Degree of Freedom
w	1	Fracture Mechanics	1
c	1	Proppant Transport	1
T	1	Energy Balance	1
F_j^*	*NP*	Flow Equations	*NP*
ρ_j	*NP*	Equation of State	*NP*
P	1	$\Sigma S_j=1$	1
S_j	*NP*	$\Sigma x_{ij}=1$	*NP*
ω_{ij}	*NC*NP*	Fugacity Equations	*NC**(*NP*-1)
Total	***4+3NP+NC*NP***	**Total**	***4+3NP+NC*NP***

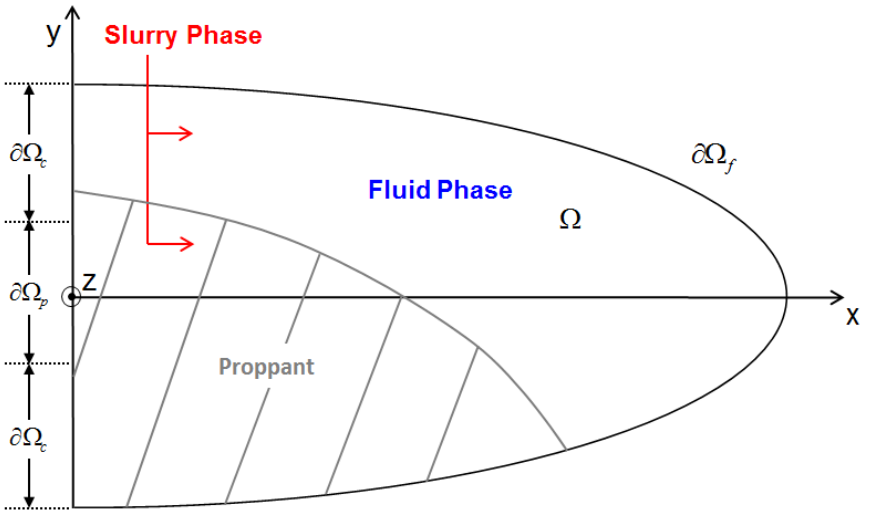

Figure 2.1: Representation of the fracture domain (Ω). The boundary of the domain ($\partial\Omega$) consists of the fracture front ($\partial\Omega_f$), the perforated interval along the wellbore ($\partial\Omega_p$), and the non-perforated section of the wellbore ($\partial\Omega_c$).

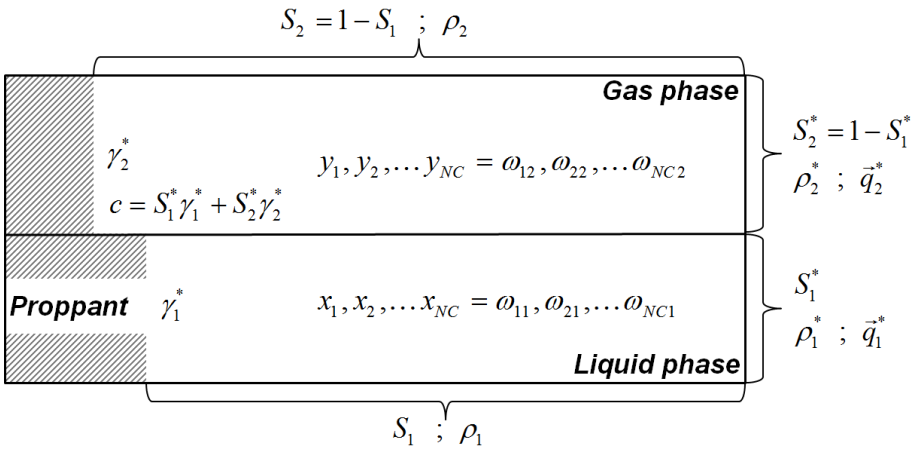

Figure 2.2: Representation of the main variables characterizing a two-phase slurry mixture. These variables are defined in the nomenclature.

Gas phase

$$\begin{cases} y_1 = 0 \\ y_2 = 1 \end{cases};\ S_2 = 0.7;\ \rho_2 = 51\frac{lbm}{ft^3}$$

$$\begin{cases} x_1 = 0.94 \\ x_2 = 0.06 \end{cases};\ S_1 = 0.3;\ \rho_1 = 63\frac{lbm}{ft^3}$$

Liquid phase

$$\begin{cases} z_1 = \dfrac{0.94\times0.3\times63 + 0\times0.7\times51}{0.3\times63 + 0.7\times51} \approx 0.325 \\ z_2 = \dfrac{0.06\times0.3\times63 + 1\times0.7\times51}{0.3\times63 + 0.7\times51} \approx 0.675 \end{cases}$$

Figure 2.3: Example of compositional calculations for 0.7-quality CO_2 foam.

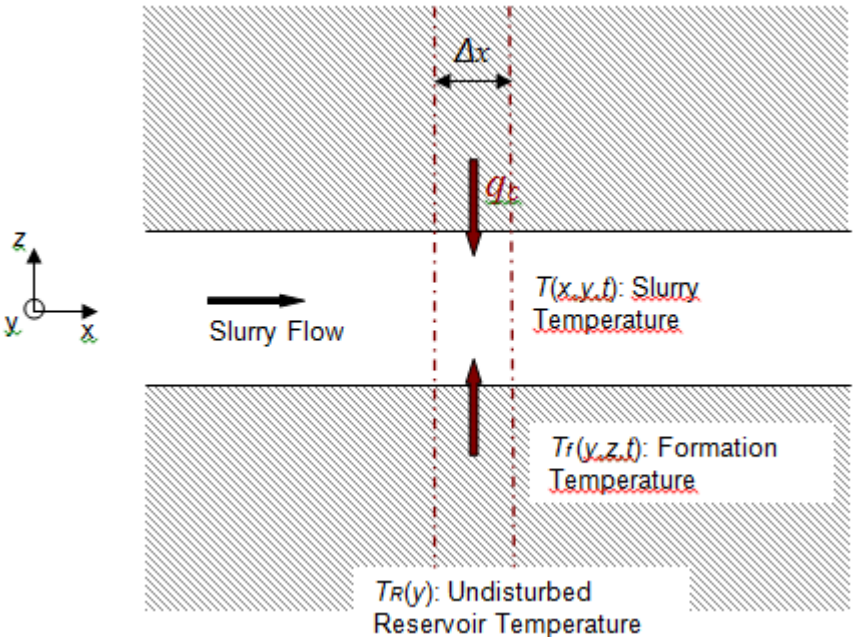

Figure 2.4: Pseudo 1D transient heat transfer between the fracture and the reservoir (top view).

Nomenclature

A_j^* = intermediate variable defined by Eq. 2.13, ft^5/(lbf-min)
c = proppant concentration (volume fraction)
$C_{p,j}$ = heat capacity of fluid phase j, BTU/(lbm-°F)
$C^*_{p,j}$ = heat capacity of slurry phase j, BTU/(lbm-°F)
$C_{w,j}$ = leakoff coefficient of fluid phase j, ft/√min
g = gravity of earth, ft/s^2
G = shear modulus of the rock, psi
H = enthalpy, psi.ft^3
K_j = flow consistency index of slurry phase j, lbm-min^n/ft^2
$k_{ret,j}$ = retardation factor for slurry phase j in the horizontal direction
K_i = K-value for component i
K_I = stress intensity factor, psi-√in
K_{IC} = fracture toughness, psi-√in
K_R = thermal conductivity of rock, BTU/(min-ft-°F)
K_γ = proppant split between two phases (γ_2/γ_1)
$q_{j,x}$ = flowrate per unit height of fluid phase j in the horizontal direction, ft^2/min
$q_{j,y}$ = flowrate per unit height of fluid phase j in the vertical direction, ft^2/min
$q^*_{j,x}$ = flowrate per unit height of slurry phase j in the horizontal direction, ft^2/min
$q^*_{j,y}$ = flowrate per unit height of slurry phase j in the vertical direction, ft^2/min
$q^*_{L,j}$ = fluid loss flowrate per unit height of fluid phase j, ft/min
$q^*_{p,j,x}$ = flowrate per unit height of proppant in phase j in the horizontal direction, ft^2/min
$q^*_{p,j,y}$ = flowrate per unit height of proppant in phase j in the vertical direction, ft^2/min
m_{pumped} = mass rate imposed at the perforations, lbm/min
M_w = molecular weight, atomic mass unit
n = normal direction
n_j = flow behavior index of slurry phase j
NC = number of components
NP = number of phases
P = fluid pressure, psi
P_c = critical pressure, psi
P_r = reduced pressure (P/P_c)
P_0 = reference pressure, psi
r = distance between the source and the field point in Eq. 2.61, ft
r_{tip} = distance to the fracture tip, ft
R = gas constant, ft-lbf/(lbm-°R)
S_j = saturation of fluid phase j
S_j^* = saturation of slurry phase j
t = time, min
T = fluid temperature, °F

T_c = critical temperature, °F
T_r = reduced temperature (T/T_c)
T_R = reservoir temperature, °F
T_0 = reference temperature, °F
V_{fluid} = total volume offluid, ft^3
V_j = volume of fluid phase j, ft^3
V^*_j = volume of slurry phase j, ft^3
V_P = total volume of proppant, ft^3
$V_{P,j}$ = volume of proppant in slurry phase j, ft^3
V_{set} = settling velocity, ft/min
V_{stokes} = Stokes settling velocity, ft/min
V_T = total slurry volume, ft^3
w = fracture width, ft
x = horizontal location, ft
y = vertical location, ft
Z = compressibility factor

Subscripts

i =component i
inj =boundary conditions at the perforations
j =phase j
$p/prop$ =proppant
R =reservoir
T = total

Superscripts

n =time step n
* =slurry property
$'$ =field point in Eq. 2.66

Greek Symbols

α_T = thermal expansion, 1/°F
β_P = isothermal compressibility, 1/psi
γ_j = proppant concentration (volume fraction) in slurry phase j
Δd = displacement of the fracture front in the normal direction, ft
Δd_{max} = maximum displacement of the fracture front, ft
$\partial\Omega$ = boundary of the fracture domain
$\partial\Omega_c$ = non-perforated portion along the wellbore
$\partial\Omega_f$ = fracture front

$\partial\Omega_p$ = perforated interval along the wellbore

$\Delta m_{fracture}$= change in fracturing fluid mass during Δt^n, lbm
$\Delta m_{leakoff}$ = mass of fluid that leaked off during Δt^n, lbm
$\Delta P_{toughness}$= initiation net pressure, psi
Δt^n = time step increment, min
$\lambda_{j,x}$, $\lambda_{j,y}$ = retardation factor for proppant in phase j in the horizontal and vertical direction
μ = fluid viscosity, cp
ρ_j = density of fluid phase j, lbm/ft^3
ρ_j^* = density of slurry phase j, lbm/ft^3
ρ_p = density of proppant, lbm/ft^3
ρ_R = density of reservoir rock, lbm/ft^3
ρ_T^* = density of slurry, lbm/ft^3
ρ_0 = density of reference at (P_0, T_0), lbm/ft^3
σ_{hmin} = *in-situ* minimum horizontal stress, psi
τ = retardation factor, min
v = Poisson's ratio of the rock
ω_{ij} = mass fraction of component i in phase j
Ω = fracture domain

References

Abou-Sayed, A.S, Sinha, K.P., and Clifton, R.J 1984. Evaluation of the Influence of *In-Situ* Reservoir Conditions on the Geometry of Hydraulic Fractures Using a 3-D Simulator: Part 1–Technical Approach, Paper SPE/DOE/GRI 12877, Unconventional Gas Recovery Symposium, Pittsburg, Pennsylvania, 13-15 May.

Adachi, J.I, Siebrits, E., Peirce, A., and Desroches, J. 2007. Computer Simulation of Hydraulic Fractures, *Int. J. Rock Mech. and Min. Sci. & Geomech.***44**: 739-757.

Barree, R.D. 1983. A Practical Numerical Simulator for Three-Dimensional Hydraulic Fracture Propagation in Heterogeneous Media. Paper SPE 12273 presented at the SPE Symposium on Reservoir Simulation, San Francisco, California, 15-18 November.

Bui, H.1977. An Integral Equations Method for Solving the Problem of a Plane Crack of Arbitrary Shape. *J. Mech. Phys. Solids***25**: 29-39.

Carslaw, H.S. and Jaeger, J.C. 1959,*Conduction of Heat in Solids*, 2nd edition, Clarendon Press, Oxford, UK.

Carter, R.D. 1957. Derivation of the general equation for estimating the extent of the fractured area, Appendix to *Optimum Fluid Characteristics for Fracture Extension*, by Howard, G.C. and Fast, C.R., *Drilling and Production Practices*, API: 261-270.

Cleary, M.P., Kawadas, M., and Lam, K.Y. 1983. Development of a Fully Three-Dimensional Simulator for Analysis and Design of Hydraulic Fracturing. Paper SPE 11631presented at the Symposium on Low-Permeability Gas Reservoirs, 14-16 March 1983, Denver, Colorado.

Clifton, R.J. and Abou-Sayed, A.S. 1981. A Variational Approach to the Prediction of the Three-Dimensional Geometry of Hydraulic Fractures. Paper SPE 9879 presented at the SPE/DOE Low Permeability Gas Reservoirs Symposium, Denver, Colorado, 27-29 May.

Economides, M. and Nolte, K.G. 2000, *Reservoir Stimulation, Third Edition*, John Wiley and Sons, New York City, New York.

Friehauf, K.E. 2009. Simulation and Design of Energized Hydraulic Fractures. Ph.D. Dissertation, The University of Texas at Austin, Austin, Texas (August 2009).

Friehauf, K.E. and Sharma, M.M. 2009. A New Compositional Model for Hydraulic Fracturing With Energized Fluids. *SPE Prod &Oper***24**(4): 562-572. SPE 115750-PA.

Gadde P. B., Liu Y., Norman J., Bonnecaze, R. and Sharma, M. M. 2004. Modeling Proppant Settling in Water-Fracs. Paper SPE 89875 presented at the SPE Annual Technical Conference and Exhibition, Houston, Texas, 26-29 September.

Gu, H. 1987. A Study of Propagation of Hydraulically Induced Fractures, Ph.D. Dissertation, The University of Texas at Austin, Austin, Texas (December 1987).

Hasan, A. and Kabir, S. 2002,*Fluid Flow and Heat Transfer in Wellbores*, Society of Petroleum Engineers, 2002.

Khade, K. and Shah, S. 2004. New Rheological Correlations for Guar Foam Fluids. *SPE Prod & Fac***19**(2): 77-85. SPE 88032-PA.

Kossecka, E. 1971. Defects as Surface Distribution of Double Forces. *Arch. Mech*. **23**: 481-494.

Liu, Y. 2006. Settling and Hydrodynamic Retardation of Proppants in Hydraulic Fractures, Ph.D. Dissertation. The University of Texas at Austin, Austin, Texas (May 2006).

Mastrojannis, E.N., Keer, L.M., and Mura, T. 1979. Stress Intensity Factor for a Plane Crack under Normal Pressure. *Int. J.Fracture***15**: 247-258.

Meyer, B.R. 1989. Heat Transfer in Hydraulic Fracturing. *SPE Prod Eng***4:** 423-429. SPE 17041-PA.

Ouyang, S. 1994. Propagation of Hydraulically Induced Fractures with Proppant Transport, Ph.D. Dissertation. The University of Texas at Austin, Austin, Texas (May 1994).

Reidenbach, V.G., Harris, P.C., Lee, Y.N, and Lord, D.L. 1986. Rheological Study of Foam Fracturing Fluids using Nitrogen and Carbon Dioxide. *SPE Prod Eng***1**(1): 31-41. SPE 12026-PA.

Ribeiro, L.H. and Sharma, M.M 2013. A New 3D Compositional Model for Hydraulic Fracturing with Energized Fluids. *SPE Prod &Oper***28**(3):259-267. SPE 159812-PA.

Settari, A. and Cleary, M.P. 1984. Three-Dimensional Simulation of Hydraulic Fracturing. *J. Pet Tech***36**(7): 1177-1190. SPE 10504-PA.

Standing, M.B. and Katz, D.L. 1942. Density of Natural Gases. *Trans. AIME***146**(1): 140-149. SPE 942140-G.

Valkó, P. and Economides, M.J. 1997. Foam-Proppant Transport. *SPE Prod & Fac***12**(4): 244-249. SPE 27897-PA.

Weaver, J. 1977. Three-Dimensional Crack Analysis. *Int. J. Solids Structures***13**: 321-330.

Yew, C.H. 1997, *Mechanics of Hydraulic Fracturing*, Gulf Publishing Company, Houston, Texas.

CHAPTER 3: FINITE ELEMENT FORMULATION AND SOLUTION ALGORITHM

The objective of Chapter 3 is to derive a finite-element formulation of the compositional fracturing problem presented in Chapter 2. The problem encompasses five non-linear, time-dependent, moving-boundary, partial differential equations (PDEs) that govern pressure, proppant concentration, component mass fractions, temperature, and fracture width. The numerical solution is complicated by the fact that three different classes of equations need to be solved: an elliptic diffusivity equation, a parabolic-hyperbolic convection-dominated equation, and a singular boundary integral equation.

The strong coupling between the equations makes the numerical solution cumbersome. To ease this process, we propose an iterative procedure and a time-step decoupling scheme to solve the system of equations simultaneously. First, we compute fracture width and pressure using a relaxation iterative procedure. Then, we solve the transport equations using a time-forward loop. The two loops constitute an essential part of the main algorithm implemented in the computer program.
In order to ensure the accuracy of the computations, a grid generation scheme is incorporated into the program. The meshing scheme consists of a dynamic unstructured 2D mesh that is suitable for all of the equations. Complex algorithms are used to efficiently re-generate the mesh as the fracture propagates. The gridding scheme encompasses unstructured Delaunay triangulation with the convection, insertion, and redistribution of nodal points. The construction of a smooth and efficient grid plays a critical role in the stability of the calculations.

3.1 SOLUTION OF THE PRESSURE EQUATION

In this chapter, we follow the nomenclature typically used in numerical methods: subscripts *i* and *j* refer to the nodal numbering; *N* refers to the total number of nodes; and the superscript *n* refers to the time step number. The component and phase numbers are now referred to by the subscripts *I* and *J*, respectively. The derivations presented in this chapter follow the general methods presented in the finite-element textbook written by Becker, Carey, and Oden (1981).

The pressure equation derived in Chapter 2 has the form of a diffusivity equation:

$$\frac{\partial}{\partial t}\left\{w\left(\sum_{j=1}^{NP}\rho_j^* S_j^*\right)\right\}+\frac{\partial}{\partial x}\left\{\left(\sum_{j=1}^{NP}\rho_j^* A_j^* S_j^*\right)\frac{\partial P}{\partial x}\right\}+\frac{\partial}{\partial y}\left\{\left(\sum_{j=1}^{NP}\rho_j^* A_j^* S_j^*\right)\frac{\partial P}{\partial y}\right\}$$
$$+\frac{\partial}{\partial y}\left\{\left(\sum_{j=1}^{NP}\rho_j^{*2} A_j^* S_j^*\right)g\right\}+\sum_{j=1}^{NP}\frac{2C_{w,j}\rho_j}{\sqrt{t-\tau}}=0 \qquad (3.1)$$
$$\underline{BCs}:\begin{cases}A^*\dfrac{\partial P}{\partial n}=(q_x)_{inj} & on\ \partial\Omega_p\\ \dfrac{\partial P}{\partial n}=0 & on\ \partial\Omega_f\ and\ \partial\Omega_c\end{cases}$$

To make the derivations more compact, Eq. 3.1 is replaced by a generic diffusivity equation that has the same type of boundary conditions (BCs). The generic equation reduces to the pressure equation with a proper choice of coefficients. The unknown is a smooth function $u(x,y,t)$, which is a function of time and location.

$$\frac{\partial\alpha}{\partial t}+\nabla.\vec{q}+\frac{2}{\sqrt{t-\tau}}q_L=0 \quad where \quad \vec{q}=\beta\vec{\nabla}u+\gamma\vec{n}_y \qquad (3.2)$$
$$\underline{BCs}:\begin{cases}\vec{q}=q_{inj}\vec{n} & on\ \partial\Omega_p\\ \vec{q}=0 & on\ \partial\Omega_f\ and\ \partial\Omega_c\end{cases}$$

A weak formulation of the problem defined in Eq. 3.2 requires the introduction of a test function $v(x,y)$.We multiply the PDE defined in Eq. 3.2 by the test function v, and integrate the equation over the domain Ω:

$$\int_\Omega v\frac{\partial\alpha}{\partial t}d\Omega+\int_\Omega v(\nabla.\vec{q})d\Omega+\int_\Omega v\frac{2}{\sqrt{t-\tau}}q_L d\Omega=0 \qquad (3.3)$$

Eq. 3.3 is integrated by parts:

$$\int_\Omega v\frac{\partial\alpha}{\partial t}d\Omega+\int_\Omega\nabla.(v\vec{q})d\Omega-\int_\Omega(\vec{\nabla}v.\vec{q})d\Omega+\int_\Omega v\frac{2}{\sqrt{t-\tau}}q_L d\Omega=0 \qquad (3.4)$$

The divergence theorem (also known as Gauss theorem) transforms the surface integral to a line integral:

$$\int_\Omega\nabla.(v\vec{q})d\Omega=\int_{\partial\Omega}v(\vec{q}.\vec{n})ds \qquad (3.5)$$

The domain boundary $\partial\Omega$ is the summation of the sub-regions $\partial\Omega_p$, $\partial\Omega_f$, and $\partial\Omega_c$. The flux along $\partial\Omega_f$, and $\partial\Omega_c$ is zero, so the line integral is zero along these sub-regions. The flux along $\partial\Omega_p$ is prescribed as a BC, and the line integral becomes:

$$\int_{\partial\Omega} v\left(\vec{q}.\vec{n}\right)ds = \int_{\partial\Omega_p} vq_{inj}ds \text{ since } \begin{cases}\vec{q} = q_{inj}\vec{n} & on\ \partial\Omega_p \\ \vec{q} = 0 & on\ \partial\Omega_f \text{ and } \partial\Omega_c\end{cases} \tag{3.6}$$

Using Eqs. 3.5 and 3.6, Eq. 3.4 reduces to:

$$\int_{\Omega} v\frac{\partial\alpha}{\partial t}d\Omega + \int_{\partial\Omega_p} vq_{inj}ds - \int_{\Omega}\left(\vec{\nabla}v.\vec{q}\right)d\Omega + \frac{2}{\sqrt{t-\tau}}\int_{\Omega} vq_L d\Omega = 0 \tag{3.7}$$

The flux is now expressed in terms of the gradient of the function of interest u:

$$\int_{\Omega} v\frac{\partial\alpha}{\partial t}d\Omega + \int_{\partial\Omega_p} vq_{inj}ds - \int_{\Omega}\gamma\left(\vec{\nabla}v.\vec{n}_y\right)d\Omega - \int_{\Omega}\beta\left(\vec{\nabla}v.\vec{\nabla}u\right)d\Omega + \frac{2}{\sqrt{t-\tau}}\int_{\Omega} vq_L d\Omega = 0 \tag{3.8}$$

Eq. 3.8 constitutes a variational statement of the problem defined in Eq. 3.2. Our goal is to find the function u such that the PDE, together with the BCs, are satisfied in the sense of weighted averages. To do so, we determine approximate solutions of Eq. 3.8 over subsets of Ω. The domain Ω is divided in N sub-domains, and we introduce N basis functions $\{\phi_1(x,y),\phi_2(x,y),...,\phi_N(x,y)\}$ that define an N-dimensional subspace covering the domain. The unknown function u and the test function v are continuous functions that can be represented by a linear combination of the N basis functions. u_N and v_N are the so-called Galerkin approximations of the functions u and v:

$$\begin{aligned} u(x,y,t) &\approx u_N(x,y,t) = \sum_{j=1}^{N} u_j(t)\phi_j(x,y) \\ v(x,y) &\approx v_N(x,y) = \sum_{i=1}^{N} v_i\phi_i(x,y) \end{aligned} \tag{3.9}$$

Since the N basis functions are known, the function u is completely determined at a given time t once the N coefficients $u_j(t)$ are determined. These coefficients are referred to as the degrees of freedom of the approximation. Inserting the Galerkin approximations of functions u and v in the variational statement of the problem, we obtain N independent equations:

$$\int_{\Omega}\frac{\partial\alpha}{\partial t}\phi_i d\Omega+\int_{\partial\Omega_p} q_{inj}\phi_i ds-\int_{\Omega}\gamma\frac{\partial\phi_i}{\partial y}d\Omega-\sum_{j=1}^{N}\int_{\Omega}\beta\left(\frac{\partial\phi_i}{\partial x}\frac{\partial\phi_j}{\partial x}+\frac{\partial\phi_i}{\partial y}\frac{\partial\phi_j}{\partial y}\right)u_j d\Omega$$
$$+\frac{2}{\sqrt{t-\tau}}\int_{\Omega} q_L\phi_i d\Omega+=0 \quad ;\ i=1...N \tag{3.10}$$

The first term of Eq. 3.10 includes a time derivative, and the fifth term includes a time-dependent leak-off rate. The time derivative for an arbitrary function f between t^n and $t^n+\Delta t^n$ is given by:

$$\left.\frac{\partial f(x,y,t)}{\partial t}\right|_{t^n+\Delta t^n}=\frac{1}{\Delta t^n}\left[\, f\left(x,y,t^n+\Delta t^n\right)-f\left(x,y,t^n\right)\right] \tag{3.11}$$

The fluid-loss term involves the inverse of the square root of time. The average rate between t^n and $t^n+\Delta t^n$ is approximated by the following time integration:

$$\int_{t^n}^{t^n+\Delta t^n}\frac{f(x,y,t)}{\sqrt{t-\tau}}dt=\frac{2}{\Delta t^n}\, f\left(x,y,t^n\right)\left(\sqrt{t^n+\Delta t^n-\tau}-\sqrt{t^n-\tau}\right) \tag{3.12}$$

Inserting Eqs. 3.11 and 3.12 in Eq. 3.10, we obtain:

$$\frac{1}{\Delta t^n}\int_{\Omega}\left(\alpha^{n+1}-\alpha^n\right)\phi_i d\Omega+\int_{\partial\Omega_p} q_{inj}\phi_i ds-\int_{\Omega}\gamma\frac{\partial\phi_i}{\partial y}d\Omega-\sum_{j=1}^{N}\int_{\Omega}\beta\left(\frac{\partial\phi_i}{\partial x}\frac{\partial\phi_j}{\partial x}+\frac{\partial\phi_i}{\partial y}\frac{\partial\phi_j}{\partial y}\right)u_j d\Omega$$
$$+\frac{4}{\Delta t^n}\left(\sqrt{t^n+\Delta t^n-\tau}-\sqrt{t^n-\tau}\right)\int_{\Omega} q_L^n\phi_i d\Omega+=0 \quad ;\ i=1...N \tag{3.13}$$

The structure of Eq. 3.13 is most easily seen by isolating the N unknowns u_j, and by rewriting the equation in the more compact form:

$$\sum_{j=1}^{N} K_{ij} u_j = \frac{1}{\Delta t^n}\left(f_{w,i}^{n+1} - f_{w,i}^{n} \right) + f_{inj,i} - f_{g,i} + \frac{1}{\Delta t^n} f_{L,i}^{n \to n+1} \quad ; \; i = 1...N$$

$$K_{ij} = \int_{\Omega} \beta \left(\frac{\partial \phi_i}{\partial x}\frac{\partial \phi_j}{\partial x} + \frac{\partial \phi_i}{\partial y}\frac{\partial \phi_j}{\partial y} \right) d\Omega \quad ; \quad \begin{cases} f_{w,i}^{n+1} = \int_{\Omega} \alpha^{n+1} \phi_i d\Omega \quad ; \quad f_{w,i}^{n} = \int_{\Omega} \alpha^{n} \phi_i d\Omega \\ f_{inj,i} = \int_{\partial\Omega_p} q_{inj} \phi_i ds \\ f_{g,i} = \int_{\Omega} \gamma \frac{\partial \phi_i}{\partial y} d\Omega \\ f_{L,i}^{n \to n+1} = 4\left(\sqrt{t^n + \Delta t^n - \tau} - \sqrt{t^n - \tau} \right) \int_{\Omega} \phi_i q_L d\Omega \end{cases} \tag{3.14}$$

The *N*x*N* rectangular array of components K_{ij} constitutes a matrix *K* commonly referred to as a *stiffness* matrix. The right side of Eq. 3.14 forms an *N* x 1 vector of components f_i, which is commonly referred to as *load* vector *F*. The unknown is the vector *U* made of *N* components u_j:

$$\bar{K}.\tilde{U} = \tilde{F} \tag{3.15}$$

The pressure equation may be obtained from the generic equation defined in Eq. 3.2 by using the following coefficients:

$$\begin{cases} \alpha = w\left(\sum_{J=1}^{NP} \rho_J^* S_J^* \right) \\ \beta = \left(\sum_{J=1}^{NP} A_J^* \rho_J^* S_J^* \right) \\ \gamma = g\left(\sum_{J=1}^{NP} \left(\rho_J^* \right)^2 A_J^* S_J^* \right) \end{cases} \quad ; \quad \begin{cases} q_L = \sum_{J=1}^{NP} C_{w,J} \rho_J \\ q_{inj} = \sum_{J=1}^{NP} \left(\rho_J^* q_J^* \right)_{inj} \end{cases} \tag{3.16}$$

Inserting Eq. 3.16 into Eq. 3.14, the discretized finite-element formulation of the pressure equation is given in a matrix form as:

$$\bar{K}.\tilde{P} = \tilde{F} \quad or \quad \sum_{j=1}^{N} K_{p,ij} P_j = \frac{1}{\Delta t^n}\left(f_{w,i}^{n+1} - f_{w,i}^{n} \right) + f_{inj,i} - f_{g,i} \frac{1}{\Delta t^n} f_{L,i}^{n \to n+1} \quad ; \; i = 1...N$$

$$K_{p,ij} = \int_{\Omega} \left(\sum_{J=1}^{NP} A_J^* \rho_J^* S_J^* \right) \left(\frac{\partial \phi_j}{\partial x} \frac{\partial \phi_i}{\partial x} + \frac{\partial \phi_j}{\partial y} \frac{\partial \phi_i}{\partial y} \right) d\Omega$$

$$\begin{cases} f_{w,i}^{n+1} = \int_{\Omega} \left\{ w \left(\sum_{J=1}^{NP} \rho_J^* S_J^* \right) \right\}^{n+1} \phi_i d\Omega \quad ; \quad f_{w,i}^{n} = \int_{\Omega} \left\{ w \left(\sum_{J=1}^{NP} \rho_J^* S_J^* \right) \right\}^{n} \phi_i d\Omega \\ f_{inj,i} = \int_{\partial\Omega_p} \left(\sum_{J=1}^{NP} \rho_J^* q_J^* \right)_{inj} \phi_i ds \\ f_{g,i} = \int_{\Omega} g \left(\sum_{J=1}^{NP} \left(\rho_J^* \right)^2 A_J^* S_J^* \right) \frac{\partial \phi_i}{\partial y} d\Omega \\ f_{L,i}^{n \to n+1} = 4 \left(\sqrt{t^n + \Delta t^n - \tau} - \sqrt{t^n - \tau} \right) \int_{\Omega} \left(\sum_{J=1}^{NP} C_{w,J} \rho_J \right) \phi_i d\Omega \end{cases} \tag{3.17}$$

3.2 SOLUTION OF THE COMPATIBILITY EQUATION

As discussed in Chapter 2, satisfying the compatibility equation is a necessary condition for the existence of a solution to the pressure equation. The increase in fracture mass must equal the mass of fluid pumped minus the mass of fluid that leaked off. This requirement yields the following time step increment:

$$\Delta t^n = \frac{\Delta m_{fracture} + \Delta m_{leakoff}}{\dot{m}_{pumped}} \tag{3.18}$$

The derivation of Eq. 3.18 is similar to the derivation used for the pressure equation. The overall conservation of mass ensures that the summation of the accumulation, injection, and fluid-loss terms is zero on a global basis. Using Eq. 3.13 as the starting point for the derivations of the compatibility equation, the overall mass balance is given in a discrete form by:

$$\begin{aligned} &\sum_{i=1}^{N} \frac{1}{\Delta t^n} \int_{\Omega} \left(\alpha^{n+1} - \alpha^n \right) \phi_i d\Omega + \sum_{i=1}^{N} \int_{\partial\Omega_p} q_{inj} \phi_i ds + \\ &\sum_{i=1}^{N} \frac{4}{\Delta t^n} \left(\sqrt{t^n + \Delta t^n - \tau} - \sqrt{t^n - \tau} \right) \int_{\Omega} q_L^n \phi_i d\Omega + = 0 \end{aligned} \tag{3.19}$$

Eq. 3.19 may be rewritten as:

$$\Delta t^n = \frac{\sum_{i=1}^{N}\int_{\Omega}\left(\alpha^{n+1}-\alpha^n\right)\phi_i d\Omega + \frac{4}{\Delta t^n}\left(\sqrt{t^n+\Delta t^n-\tau}-\sqrt{t^n-\tau}\right)\sum_{i=1}^{N}\int_{\Omega} q_L^n\phi_i d\Omega}{\sum_{i=1}^{N}\int_{\partial\Omega_p}\left|q_{inj}\right|\phi_i ds} \tag{3.20}$$

Using the coefficients defined in Eq. 3.16, we can rewrite the compatibility condition as:

$$\Delta t^n = \frac{\sum_{i=1}^{N} f_{w,i}^{n+1} - \sum_{i=1}^{N} f_{w,i}^{n} + \sum_{i=1}^{N} f_{L,i}^{n\to n+1}}{\sum_{i=1}^{N} f_{inj,i}}$$

$$\begin{cases} f_{w,i}^{n+1} = \int_{\Omega}\left\{w\left(\sum_{J=1}^{NP}\rho_J^* S_J^*\right)\right\}^{n+1}\phi_i d\Omega \;;\quad f_{w,i}^{n} = \int_{\Omega}\left\{w\left(\sum_{J=1}^{NP}\rho_J^* S_J^*\right)\right\}^{n}\phi_i d\Omega \\ f_{inj,i} = \int_{\partial\Omega_p}\left(\sum_{J=1}^{NP}\rho_J^* q_J^*\right)_{inj}\phi_i ds \\ f_{L,i}^{n\to n+1} = 4\left(\sqrt{t^n+\Delta t^n-\tau}-\sqrt{t^n-\tau}\right)\int_{\Omega}\left(\sum_{J=1}^{NP} C_{w,J}\rho_J\right)\phi_i d\Omega \end{cases} \tag{3.21}$$

The fluid-loss term in Eq. 3.21 is itself a function of the time increment; therefore, an iterative scheme is used to solve this convoluted problem. The time increment for the new iteration k+1 is given by:

$$\left(\Delta t^n\right)_{k+1} = \left(\frac{\sum_{i=1}^{N} f_{w,i}^{n+1} - \sum_{i=1}^{N} f_{w,i}^{n} + \sum_{i=1}^{N} f_{L,i}^{n\to n+1}}{\sum_{i=1}^{N} f_{inj,i}}\right)_k \tag{3.22}$$

When this value of the time increment is used in solving the pressure equation, the compatibility condition is automatically satisfied.

3.3 SOLUTION OF THE CONVECTION-DOMINATED EQUATIONS

The proppant transport, component transport, and temperature equations are convection-dominated equations of the same mathematical form. The BCs are similar, and these problems are different formulations of the same generic problem (as seen in Table 3.1); therefore, these equations are solved in a similar fashion.

Convection-dominated equations often lead to oscillations even when the analytical solution is smooth and monotonic. Several approaches have been used to treat this problem.

In this work, we introduce a dispersion term to reduce oscillations. This term accounts for both physical diffusion (due to concentration gradients) and numerical dispersion. Moreover, the temperature equation is rewritten in a dimensionless form to dampen oscillations. The dimensionless temperature is introduced as:

$$T_D = \frac{T - T_{inj}}{T_R - T_{inj}} \tag{3.23}$$

By definition, T_D is between 0 and 1; and the new BC along the perforations is T_D=0. To make the derivations more compact, the three convection-dominated problems are replaced by the generic problem given in Eq. 3.24. The unknown is a smooth function $u(x,y,t)$, which is a function of time and location.

$$\begin{aligned} &\frac{\partial}{\partial t}(\alpha u) + \nabla.(\vec{q}u) - \nabla.\left(w\varepsilon_d \vec{\nabla} u\right) + \frac{2}{\sqrt{t-\tau}}(q_L + q_{cond})u = f_R \\ &\underline{BCs}: \begin{cases} u = u_{inj} & on\ \partial\Omega_p \\ \vec{q} = 0 & on\ \partial\Omega_f\ and\ \partial\Omega_c \end{cases} \end{aligned} \tag{3.24}$$

Introducing the test function $v(x,y)$, and integrating the PDE over the domain Ω gives:

$$\begin{aligned} &\int_\Omega v\frac{\partial}{\partial t}(\alpha u)d\Omega + \int_\Omega v\nabla.(\vec{q}u)d\Omega - \int_\Omega v\nabla.\left(w\varepsilon_d\vec{\nabla}u\right)d\Omega \\ &+\int_\Omega v\frac{2}{\sqrt{t-\tau}}(q_L + q_{cond})ud\Omega = \int_\Omega vf_R d\Omega \end{aligned} \tag{3.25}$$

Eq. 3.25 is integrated by parts:

$$\begin{aligned} &\int_\Omega v\alpha\frac{\partial u}{\partial t}d\Omega + \int_\Omega vu\frac{\partial \alpha}{\partial t}d\Omega + \int_\Omega \nabla.(uv\vec{q})d\Omega - \int_\Omega u\left(\vec{\nabla}v.\vec{q}\right)d\Omega - \int_\Omega \nabla.\left(w\varepsilon_d v\vec{\nabla}u\right)d\Omega \\ &+\int_\Omega w\varepsilon_d\left(\vec{\nabla}v.\vec{\nabla}u\right)d\Omega + \int_\Omega v\frac{2}{\sqrt{t-\tau}}(q_L + q_{cond})ud\Omega = \int_\Omega vf_R d\Omega \end{aligned} \tag{3.26}$$

The divergence theorem transforms the surface integrals to line integrals:

$$\int_{\Omega} \nabla.\left(uv\vec{q}\right) d\Omega = \int_{\partial\Omega} vu\left(\vec{n}.\vec{q}\right) ds$$
$$\int_{\Omega} \nabla.\left(w\varepsilon_d v\vec{\nabla}u\right) d\Omega = \int_{\partial\Omega} vw\varepsilon_d \frac{\partial u}{\partial n} ds \tag{3.27}$$

The flux along $\partial\Omega_f$, and $\partial\Omega_c$ is zero, so the line integral is zero along these sub-regions. Dirichlet BCs are prescribed along $\partial\Omega_p$, so the test function equals zero over this sub-domain:

$$\begin{cases} \int_{\partial\Omega} vw\varepsilon_d \frac{\partial u}{\partial n} ds = 0 \\ \int_{\partial\Omega} vu\left(\vec{n}.\vec{q}\right) ds = 0 \end{cases} \quad \text{since} \quad \begin{cases} u = u_{inj} \Rightarrow v = 0 \; on \; \partial\Omega_p \\ \frac{\partial u}{\partial n} = 0 \quad and \quad \vec{n}.\vec{q} = 0 \; on \; \partial\Omega_f \; and \; \partial\Omega_c \end{cases} \tag{3.28}$$

Using Eqs. 3.27 and 3.28, Eq. 3.26 reduces to:

$$\int_{\Omega} v\alpha \frac{\partial u}{\partial t} d\Omega + \int_{\Omega} vu \frac{\partial \alpha}{\partial t} d\Omega - \int_{\Omega} u\left(\vec{\nabla}v.\vec{q}\right) d\Omega + \int_{\Omega} w\varepsilon_d \left(\vec{\nabla}v.\vec{\nabla}u\right) d\Omega$$
$$+ \frac{2}{\sqrt{t-\tau}} \int_{\Omega} v\left(q_L + q_{cond}\right) u d\Omega = \int_{\Omega} v f_R d\Omega \tag{3.29}$$

Using the Galerkin discretization introduced in section 3.1, we obtain a discretized finite-element formulation of the convection-dominated problem:

$$\sum_{j=1}^{N} \int_{\Omega} \alpha\phi_i\phi_j \frac{du_j}{dt} d\Omega + \sum_{j=1}^{N} \int_{\Omega} \frac{\partial\alpha}{\partial t} \phi_i\phi_j u_j d\Omega - \sum_{j=1}^{N} \int_{\Omega} \left(q_x \frac{\partial\phi_i}{\partial x} + q_y \frac{\partial\phi_i}{\partial y} \right) \phi_j u_j d\Omega$$
$$+ \varepsilon_d \sum_{j=1}^{N} \int_{\Omega} \left(\frac{\partial\phi_j}{\partial x}\frac{\partial\phi_i}{\partial x} + \frac{\partial\phi_j}{\partial y}\frac{\partial\phi_i}{\partial y} \right) w u_j d\Omega + \frac{2}{\sqrt{t-\tau}} \sum_{j=1}^{N} \int_{\Omega} \left(q_L + q_{cond}\right) \phi_i\phi_j u_j d\Omega \tag{3.30}$$
$$= \int_{\Omega} \phi_i f_R d\Omega \quad ; \; i = 1...N$$

The N independent equations may be rewritten in a more compact form:

$$\sum_{j=1}^{N} A_{ij}\frac{du_j}{dt}+\sum_{j=1}^{N}\left(B_{1,ij}+B_{2,ij}+B_{3,ij}+B_{4,ij}+B_{5,ij}\right)u_j=C_i \quad ;\ i=1...N$$

$$\begin{cases} A_{ij}=\int_{\Omega}\alpha\phi_i\phi_j d\Omega \\ B_{1,ij}=\int_{\Omega}\frac{\partial\alpha}{\partial t}\phi_i\phi_j d\Omega \\ B_{2,ij}=-\int_{\Omega}\left(q_x\frac{\partial\phi_i}{\partial x}+q_y\frac{\partial\phi_i}{\partial y}\right)\phi_j d\Omega \\ B_{3,ij}=\varepsilon_d\int_{\Omega}\left(\frac{\partial\phi_j}{\partial x}\frac{\partial\phi_i}{\partial x}+\frac{\partial\phi_j}{\partial y}\frac{\partial\phi_i}{\partial y}\right)w d\Omega \end{cases} ; \begin{cases} B_{4,ij}=\frac{2}{\sqrt{t-\tau}}\int_{\Omega}q_L\phi_i\phi_j d\Omega \\ B_{5,ij}=\frac{2}{\sqrt{t-\tau}}\int_{\Omega}q_{cond}\phi_i\phi_j d\Omega \\ C_i=\int_{\Omega}\phi_i f_R d\Omega \end{cases} \tag{3.31}$$

Using an implicit time scheme discretization, Eq. 3.31 becomes:

$$\sum_{j=1}^{N} A_{ij}\frac{u_j^{n+1}-u_j^n}{\Delta t^n}+\sum_{j=1}^{N}\left(B_{1,ij}+B_{2,ij}+B_{3,ij}+B_{4,ij}+B_{5,ij}\right)^{n+1}u_j^{n+1}=C_i^{n+1} \quad ;\ i=1...N \tag{3.32}$$

The *N* independent equations may be written in a typical matrix form with the following choice of coefficients:

$$\bar{K}.\tilde{U}=\tilde{F} \quad or \quad \sum_{j=1}^{N}K_{ij}u_j^{n+1}=F_i \quad ;\ i=1...N$$

$$where \quad \begin{cases} K_{ij}=A_{ij}+\Delta t^n\left(B_{1,ij}+B_{2,ij}+B_{3,ij}+B_{4,ij}+B_{5,ij}\right) \\ F_i=C_i+\sum_{j=1}^{N}A_{ij}u_j^n \end{cases} \tag{3.33}$$

Eq. 3.33 is a finite-element matrix formulation of the generic problem defined in Eq. 3.24. The corresponding finite-element formulations of the proppant, component, and temperature equations are obtained using the coefficients given in Table 3.2. The corresponding matrix equations are given in Table 3.3.

3.4 SOLUTION OF THE PRESSURE OPENING EQUATION

The fracture opening equation relates the net pressure and the fracture opening displacement. Along the fracture edge, the fracture opening is zero. The strong form of the problem is given by:

$$
\begin{aligned}
&-P(x,y)+\sigma_{h\min}(x,y)=\frac{G}{4\pi(1-\nu)}\int_{\Omega}\left[\frac{\partial}{\partial x}\left(\frac{1}{r}\right)\frac{\partial w(x,y)}{\partial x'}+\frac{\partial}{\partial y}\left(\frac{1}{r}\right)\frac{\partial w(x,y)}{\partial y'}\right]d\Omega \\
&\text{where } r=\sqrt{\left(x'-x\right)^2+\left(y'-y\right)^2} \\
&\underline{BC}: w=0 \quad \text{on } \partial\Omega_f
\end{aligned}
\tag{3.34}
$$

This boundary integral equation is singular, and its solution requires complex numerical techniques. We refer here to the work of Gu (1987), who solved the equation by forming a weak formulation of the equation in which the differentiation of the singular term (1/*r*) is transferred to the test function *v*. The derivations of the finite-element formulation of the problem are included in Gu (1987). The fracture width *w* is approximated by a finite number *N* of terms using a Galerkin approximation:

$$
w(x,y,t)\approx w_N(x,y,t)=\sum_{j=1}^{N}w_j(t)\phi_j(x,y) \tag{3.35}
$$

The matrix form of the weak formulation is given by:

$$
\begin{aligned}
&\bar{K}.\tilde{W}=\tilde{F} \quad or \quad \sum_{j=1}^{N}K_{w,ij}w_j=-f_{p,i}+f_{\sigma,i} \quad ; i=1...N \\
&\begin{cases}
K_{w,ij}=\dfrac{G}{4\pi(1-\nu)}\displaystyle\int_{\Omega}\int_{\Omega'}\left(\frac{1}{r}\right)\left(\frac{\partial\phi_i}{\partial x}\frac{\partial\phi_j}{\partial x'}+\frac{\partial\phi_i}{\partial y}\frac{\partial\phi_j}{\partial y'}\right)d\Omega' d\Omega \\
f_{p,i}=\displaystyle\int_{\Omega}\phi_i P\,d\Omega \\
f_{\sigma,i}=\displaystyle\int_{\Omega}\phi_i\sigma_{h\min}d\Omega
\end{cases}
\end{aligned}
\tag{3.36}
$$

Eq. 3.36 requires a double integration over the fracture domain; one integral comes from the strong form of the equation (since the equation is a boundary integral equation), and the second integral appears during the formulation of the weak statement of the problem.

3.5 MAIN ALGORITHM

3.5.1 Overview of the Main Algorithm

Fig. 3.1 shows a simplified version of the main algorithm implemented in *EFRAC-3D*. The algorithm shows the main interactions between the different equations presented thus far. The algorithm also includes a wellbore model, which relates the surface and bottomhole conditions, and a productivity model, which assesses the productivity of the

fractured well during flowback. The wellbore and productivity models are described in Chapter 4.

As seen in Fig. 3.1, the main algorithm solves the pressure and fracture opening equations together using an iterative scheme. This choice is motivated by the strong coupling between these equations, as the presence of the $1/w^3$ term in the pressure equation makes this equation highly sensitive to changes in fracture width. The simultaneous resolution of the compatibility condition is also required because it is a necessary condition to the existence of a solution for the pressure equation. The iterative scheme is shown on the left side of Fig. 3.2, which is a more detailed version of the simplified algorithm presented in Fig. 3.1. As seen on the right side of Fig. 3.2, we use a second algorithm to solve the transport equations separately. The main features of the main algorithm are discussed in the following sections.

3.5.2 Fracture Propagation

An incremental process approximates fracture propagation. For a short period of time, the fracture remains stationary. The fracture front is temporarily arrested by the fracture toughness or by the *in-situ* stress contrast. During this time, fluid is pumped into the fracture causing an increase of fluid pressure, fracture width, and stress intensity factor at the fracture front. When the stress intensity factor exceeds the fracture toughness, the fracture front propagates. The maximum displacement of the fracture front (Δd_{max}) controls the motion of the fracture. This maximum displacement occurs at the node where the stress intensity factor is maximum (K_{Imax}). For the other nodes located along the fracture tip, their displacement is governed by the criterion established by Mastrojannis *et al.* (1979):

$$\Delta d = \max\left(\Delta d_{\max} \left(\frac{K_I - K_{IC}}{K_{IC}} \right); 0 \right) \tag{3.37}$$

This method guarantees that the fracture front is not propagating artificially if the local value of K_I does not exceed K_{IC}. Figs. 3.3 and 3.4 show the motion of the fracture between consecutive time steps. In our algorithm, the fracture is forced to propagate at each time step to avoid unnecessary re-meshing. We accomplish this by adjusting the fluid pressure so that the critical value is exceeded at each time step. In other words, the period of time necessary to reach the maximum front displacement is calculated from the compatibility condition, which is a mass balance over the entire fracture. It should be noted that the motion of the front shown in Fig. 3.3 is exaggerated for display purposes; the two fracture fronts are actually separated by twenty successive time steps.

3.5.3 Adaptive Fracture Front Displacement

The speed of the propagation process is indirectly controlled by Δd_{max}. If Δd_{max} increases, the mass required to fill the gap between the old and the new fracture front increases, so the value of Δt^n calculated from the compatibility condition increases. Although we cannot freely choose the value of Δt^n, we can control the speed at which the fracture propagates using Δd_{max}. Several options may be used for Δd_{max}:

- Δd_{max} remains constant: the user chooses its value.
- Δd_{max} is a function of the difference between K_I and K_{IC}: the front displacement increases as the stress intensity factor increases.
- Δd_{max} is a function of the velocity of the fluid front: this method ensures that the fracture propagates at a velocity comparable to the fluid front. (This approach is similar to the one proposed by Linkov (2011)).
- Δd_{max} changes over time to ensure that the value of Δt^n calculated from the compatibility condition remains within a prescribed range.

Regardless of the method we use, Δd_{max} is the numerical parameter that is not estimated from experimental data. Although it provides some flexibility to improve the numerical stability, this flexibility is artificial, and its impact on the fracture propagation process is undesirable. The fracture propagation criterion is intrinsically grid-dependent. This numerical artifact is common in fracture modeling, as discussed by Economides and Nolte (2000).

3.5.4 Time Decoupling Scheme

We chose to use an implicit backward finite-differencing scheme for the time derivatives. This scheme is unconditionally stable, which makes it particularly suitable for calculations in which the step increment is not chosen arbitrarily by the user. As the fracture grows, the time step calculated from the compatibility equation increases significantly. Fig. 3.5 shows such an example. After a few minutes, the time increment may be too large for convection-dominated equations, which are more prone to oscillations than the elliptic diffusivity equation.

We introduce a new time-decoupling scheme to improve numerical stability and dampen oscillations. First, we compute the fracture width and fluid pressure using the relaxation iterative procedure described in section 3.5.5. Then, we solve the transport equations using a time-forward loop. For the time-forward loop, the time step Δt^n is divided in smaller time steps, which can be adjusted by the user (Δt_{cc}). For each time step Δt^n, fracture width and fluid pressure are interpolated linearly using the values obtained at times t^n and $t^n+\Delta t^n$, as seen on the right side of Fig. 3.6. Since the coupling between the transport equations is not as strong as the coupling between the fracture opening and

pressure equations, individual iterative schemes are used for solving each equation. The time-forward loop appears on the right side of the main algorithm presented in Fig. 3.2.

3.5.5 Relaxation Process

We use an adaptive relaxation iterative scheme to solve the fracture mechanics, pressure equation, and compatibility condition together. The process consists of constructing a succession of approximations that converge toward the desired solution. For a given iteration, the new estimate is based on the approximation obtained at the previous iteration and the solution obtained at the previous time step. This is done by using a linear extrapolation of the solution:

$$w^{n(k+1)} = \alpha_r F\left[w^{n(k)} \right] + \left(1-\alpha_r\right) w^{n-1} \tag{3.38}$$

In Eq. 3.38, α_r is the relaxation parameter ($0 \leq \alpha_r \leq 1$); n is the time step number; k is the iteration number; and F refers to the process of substituting $w^{n(k)}$ into the fracture opening equation. The relaxation parameter controls the convergence of the iterative process. Since the problem is highly non-linear, large values of α_r may result in the divergence or oscillation of the iterative process. On the other hand, a low value of α_r slows down the computations. The typical value used in this work is 0.3. The actual value of α_r varies over time based on the behavior of the solution, and the iterative process is said to be *adaptive*. The value of α_r is decreased if the change in fracture width becomes more dramatic, and it is increased for smooth problems with slow changes in fracture width.

3.5.6 Linear Solvers

The numerical resolution of the different PDEs consists of solving different versions of the matrix equation $\bar{K}.\tilde{U} = \tilde{F}$ where K is a N x N stiffness matrix; F is a N x 1 load vector; and U is a N x 1 unknown vector. The properties of the matrices differ for the various PDEs; hence, different solvers can be used. In this work, we use the *LAPACK* library, which is a software library for numerical linear algebra. We use version 3.3of the library, which is provided by the University of Tennessee, the University of California Berkeley, the University of Colorado, and NAG Ltd.

The resolution of the matrix equation is a two-step process: the first subroutine computes the LU factorization of the stiffness matrix, and the second subroutine solves the factorized equation. The list of subroutines used in this work includes:

- *SPOTRF-SPOTRS*: These subroutines are used for solving the fracture opening equation. The first subroutine computes the Cholesky factorization of a real symmetric positive definite matrix *K*.

- *SSYTRF-SSYTRS*: These subroutines are used for solving the pressure equation. The first subroutine factors a real symmetric matrix *K*.
- *SGETFR-SGETRS*: These subroutines are used for solving the proppant transport, component transport, and temperature equations. The first subroutine factors a general matrix *K* using Gaussian elimination with partial pivoting.

Improving the resolution of the matrix equations was non-essential to this work, and the performance of the *LAPACK* solvers was considered satisfactory. More efficient solvers are nonetheless available, and their future implementation could improve the computation time and accuracy.

3.6 MAIN FEATURES OF THE DYNAMIC UNSTRUCTURED MESH

3.6.1 Past Developments

The meshing and interpolation techniques discussed in this dissertation are based on the work of several authors. The original grid was implemented by Gu (1987), who introduced tip-specific elements along the fracture edge to overcome the singularity arising near the fracture tip. The gridding scheme, however, lacked flexibility and was not suitable for propagating elongated fractures. The number of nodes and the number of elements were constant, and the elements were constructed by connecting the adjacent nodes in a fixed relation among them. Then, Ouyang (1994) improved the gridding scheme by developing an adaptive re-meshing scheme. In his algorithm, additional nodes were implemented along the boundary and inside the domain, as the fracture grows over time. The elements were constructed in an optimized manner using the Delaunay triangulation and tactically assigned pivot points. Finally, additional criteria for node insertions have been implemented to optimize the construction of the elements. These criteria were developed by researchers at the Oak Ridge National Laboratories, and particularly by Renka who initiated these gridding capabilities (1981).

3.6.2 Mesh Structure

As the fracture grows during pumping, the fracture shape depends primarily on the vertical distribution of the minimum horizontal stress and on the fracturing treatment. The fracture is represented by a 2D dynamic unstructured mesh, of which its shape is an integral part of the solution of the moving boundary problem. The mesh is periodically remeshed for maintaining an optimal grid for the numerical evaluation of the solutions. However, the mesh may be distorted in some cases, and the irregularly shaped domain can create numerical instabilities. Therefore, building an efficient mesh generator is critical to obtain smooth solutions to the fracture propagation problem.

As seen in Fig. 3.3, the mesh consists of triangular elements and quadrilateral elements located along the fracture edge. Inside the fracture, none of the governing equations are singular, so the same element and shape functions are suitable for all the equations. The fracture opening equation becomes singular near the fracture edge. The singularity is removed by using tip-specific quadrilaterals along the fracture boundary.

3.6.3 Elements and Shape Functions

As there are different types of elements, there are different types of shape functions. For all the equations, we use linear triangular elements inside the domain. The master element for the regular triangles is shown on the left side of Fig. 3.7. The associated shape functions ψ_i^t are given by:

$$\psi_1^t = 1-\xi-\eta \quad ; \quad \psi_2^t = \xi \quad ; \quad \psi_3^t = \eta \tag{3.39}$$

ξ and η are the coordinates in the *master* element, which are mapped in the *x-y* fracture referential using simple coordinate transformations (Becker, Carey, and Oden 1981). Two types of shape functions are used for the quadrilateral elements: regular bilinear shape functions and singular root shape functions. The bilinear shape functions ψ_i^q are used for the regular quadrilaterals:

$$\begin{aligned} \psi_1^q &= \frac{1}{4}(1-\eta)(1-\xi) \quad ; \quad \psi_2^q = \frac{1}{4}(1-\eta)(1+\xi) \\ \psi_3^q &= \frac{1}{4}(1+\eta)(1+\xi) \quad ; \quad \psi_4^q = \frac{1}{4}(1+\eta)(1-\xi) \end{aligned} \tag{3.40}$$

We use singular root shape functions to solve the singular fracture opening equation over the quadrilateral elements. The shape of these functions is consistent with the work of Kassir and Sih (1966), who observed that the fracture opening displacement decreases with the square root of the distance towards the fracture tip. The master element for the singular quadrilaterals is shown on the right side of Fig. 3.7. The associated shape functions ψ_i^s and their derivatives are given by:

$$\begin{aligned} &\psi_1^s = \frac{1}{2}(1-\eta)(1-\xi)^{1/2} \quad ; \quad \psi_2^s = 0 \quad ; \quad \psi_3^s = 0 \quad ; \quad \psi_4^s = \frac{1}{2}(1+\eta)(1-\xi)^{1/2} \\ &\frac{\partial \psi_1^s}{\partial \xi} = -\frac{1}{4}(1-\eta)(1-\xi)^{-1/2} \quad ; \quad \frac{\partial \psi_4^s}{\partial \xi} = -\frac{1}{4}(1+\eta)(1-\xi)^{-1/2} \\ &\frac{\partial \psi_1^s}{\partial \eta} = -\frac{1}{2}(1-\xi)^{1/2} \quad ; \quad \frac{\partial \psi_4^s}{\partial \eta} = \frac{1}{2}(1-\xi)^{1/2} \end{aligned} \tag{3.41}$$

By construction, the side 2-3 of the singular quadrilateral always coincides with the fracture front where the width is zero. The side 1-4 of the singular quadrilateral is connected to the base of the adjacent triangle, as seen in Fig. 3.8. The displacement along the side 1-4 of the quadrilateral is a linear function, which is completely determined by its nodal values at nodes 1 and 4. On the adjacent triangle, the displacement is also a linear function along the nodes connected to side 1-4.

Therefore, there is no gap in the opening displacement between the singular and the regular elements. This arrangement is shown on the right side of Fig. 3.8.

We use Gaussian quadrature rules to perform numerical integrations. The order of the quadrature depends on the type of element. The following quadrature rules are used in this work:

- 12-point integral rule for 1D integration along a segment;
- 7-point integral rule for 2D integration along a regular triangle;
- 9-point integral rule for 2D integration along a bilinear regular quadrilateral (which is used for the pressure and transport equations); and
- 9-point integral rule for 2D integration along a bilinear singular quadrilateral (which is used for the fracture opening equation).

3.6.4 Boundary Node Generation

We use different re-meshing techniques for constructing the boundary nodes and the interior nodes. At each time step Δt^n, the fracture front advances along its outward normal direction, as seen in Fig. 3.4. The nodal points from the previous fracture front $\partial\Omega_f^n$ are repositioned to form the new fracture front $\partial\Omega_f^{n+1}$. This movement of the boundary nodes is the first step performed by the re-meshing algorithm. These nodes delimit the fracture domain.
The spacing between the boundary nodes control the size of the quadrilaterals and adjacent triangles placed near the fracture front. These elements play a critical role in determining the shape of the fracture. An efficient optimization scheme is required to refine the shape of the front and avoid numerical instabilities, particularly for cases where the distribution of the *in-situ* stresses promotes fracture propagation across multiple layers. As the fracture crosses boundaries, re-entrant corners may form and hinder the numerical calculations.

We use several refinement criteria for boundary node generation and re-distribution. A new boundary node is inserted if the ratio of the spacing between two nodes divided by the minimum spacing along the front exceeds a critical value. Similarly, a new boundary node is inserted if the ratio of the spacing between two nodes divided by the spacing between the adjacent nodes exceeds a critical value. Once we determined the number of

boundary nodes, the nodes are re-distributed using a technique referred to as *smoothing*. The position of a given node is modified if the ratio between adjacent nodes is lower than a critical value, or if this ratio exceeds a critical value. This can change these parameters to control the distribution of the boundary nodes along the fracture edge.

3.6.5 Interior Node Generation

Once the quadrilaterals are positioned along the boundary, the triangular elements are distributed within the newly formed domain. The location of the nodes, as well as the total number of nodes, is critical to ensure the stability of the numerical calculations. The construction of the interior mesh encompasses the redistribution of the existing nodes and the insertion of new nodes.

Several meshing techniques are used for interior node generation. First, we re-distribute the interior nodes using an angle-weighted average smoothing method. This method, referred to as node *convection*, reduces the occurrence of elongated elements (Ouyang 1997). Then, we remove large elements by inserting additional nodes. If the area of a triangle exceeds a critical value, a node is inserted so the triangle is divided into three smaller elements. In addition, if the ratio of the area of a triangle divided by the area of the smallest triangle exceeds a critical value, a node is inserted into the larger triangle. Finally, we construct the triangles from the interior nodes using the Delaunay triangulation, which reduces the formation of elongated elements.

The meshing techniques presented in this chapter were satisfactory for most cases, but they sometimes led to inaccurate numerical results for complex fracture shapes. Over the past decade, there have been significant developments in re-meshing techniques and adaptive schemes for moving boundary problems. In particular, the video game industry has developed fast and flexible unstructured meshing schemes that could be applicable to fracturing. Some of these techniques could be implemented in the future to improve the current gridding capabilities.

Table 3.1: Comparison of the proppant transport, component transport, and temperature equations

Proppant c	Component ω_{I1}	Temperature T_D
$\frac{\partial}{\partial t}(\alpha c)+\nabla.(\vec{q}c)$ $-\nabla.\left(w\varepsilon\vec{\nabla}c\right)=0$ $\begin{cases} c=c_{inj} \text{ on } \partial\Omega_p \\ \vec{q}=0 \text{ on } \partial\Omega_f \text{ and } \partial\Omega_c \end{cases}$	$\frac{\partial}{\partial t}(\alpha\omega_{I1})+\nabla.(\vec{q}\omega_{I1})$ $-\nabla.\left(w\varepsilon\vec{\nabla}\omega_{I1}\right)+\frac{2}{\sqrt{t-\tau}}q_L\omega_{I1}=0$ $\begin{cases} \omega_{I1}=\omega_{I1,inj} \text{ on } \partial\Omega_p \\ \vec{q}=0 \text{ on } \partial\Omega_f \text{ and } \partial\Omega_c \end{cases}$	$\frac{\partial}{\partial t}(\alpha T_D)+\nabla.(\vec{q}T_D)-\nabla.\left(w\varepsilon\vec{\nabla}T_D\right)$ $+\frac{2}{\sqrt{t-\tau}}(q_L+q_{cond})=\frac{2}{\sqrt{t-\tau}}\left(q_L\frac{T_{inj}}{T_{inj}-T_R}+q_{cond}\right)$ $\begin{cases} T_D=0 \text{ on } \partial\Omega_p \\ \vec{q}_T=0 \text{ on } \partial\Omega_f \text{ and } \partial\Omega_c \end{cases}$

Table 3.2: Choice of coefficients to obtain the proppant transport, component transport, and temperature equations from the generic problem given in Eq. 3.24.

	Proppant c	Component ω_{I1}	Temperature T_D
α	w	$w(1-c)(\rho_1 S_1+K_I\rho_2 S_2)$	$w\left(S_1^*\rho_1^*C_{p,1}^*+S_2^*\rho_2^*C_{p,2}^*\right)$
q_x	$\frac{\lambda_{1,x}q_{1,x}^*+K_\gamma\lambda_{2,x}q_{2,x}^*}{K_\gamma+S_1^*(1-K_\gamma)}$	$\rho_1 q_{1,x}^*\left((1-\gamma_1)+\frac{\rho_p}{\rho_1}\gamma_1(1-\lambda_{1,x})\right)+$ $K_I\rho_2 q_{2,x}^*\left((1-\gamma_2)+\frac{\rho_p}{\rho_2}\gamma_2(1-\lambda_{2,x})\right)$	$q_{1,x}^*\rho_1^*C_{p,1}^*+q_{2,x}^*\rho_2^*C_{p,2}^*$
q_y	$\frac{\lambda_{1,y}q_{1,y}^*+K_\gamma\lambda_{2,y}q_{2,y}^*}{K_\gamma+S_1^*(1-K_\gamma)}$	$\rho_1 q_{1,y}^*\left((1-\gamma_1)+\frac{\rho_p}{\rho_1}\gamma_1(1-\lambda_{1,y})\right)+$ $K_I\rho_2 q_{2,y}^*\left((1-\gamma_2)+\frac{\rho_p}{\rho_2}\gamma_2(1-\lambda_{2,y})\right)$	$q_{1,y}^*\rho_1^*C_{p,1}^*+q_{2,y}^*\rho_2^*C_{p,2}^*$
q_L	0	$\rho_1 C_{w,1}+K_I\rho_2 C_{w,2}$	$\rho_1 C_{p,1}C_{w,1}+\rho_2 C_{p,2}C_{w,2}$
q_{cond}	0	0	$\sqrt{\frac{K_R\rho_R C_{p,R}}{\pi}}\psi(c)\phi(c)$
f_R	0	0	$q_L\frac{T_{inj}}{T_{inj}-T_R}+q_{cond}$

Table 3.3: Matrix coefficients in Eq. 3.33 to solve the proppant transport, component transport, and temperature equations.

	Proppant c	Component ω_{l1}	Temperature T_D
A_{ij}	$\int_\Omega \alpha\phi_i\phi_j d\Omega$	$\int_\Omega \alpha\phi_i\phi_j d\Omega$	$\int_\Omega \alpha\phi_i\phi_j d\Omega$
$B_{1,ij}$	$\int_\Omega \frac{\partial\alpha}{\partial t}\phi_i\phi_j d\Omega$	$\int_\Omega \frac{\partial\alpha}{\partial t}\phi_i\phi_j d\Omega$	$\int_\Omega \frac{\partial\alpha}{\partial t}\phi_i\phi_j d\Omega$
$B_{2,ij}$	$-\int_\Omega \left(q_x \frac{\partial\phi_i}{\partial x} + q_y \frac{\partial\phi_i}{\partial y} \right)\phi_j d\Omega$	$-\int_\Omega \left(q_x \frac{\partial\phi_i}{\partial x} + q_y \frac{\partial\phi_i}{\partial y} \right)\phi_j d\Omega$	$-\int_\Omega \left(q_x \frac{\partial\phi_i}{\partial x} + q_y \frac{\partial\phi_i}{\partial y} \right)\phi_j d\Omega$
$B_{3,ij}$	$\varepsilon\int_\Omega \left(\frac{\partial\phi_j}{\partial x}\frac{\partial\phi_i}{\partial x} + \frac{\partial\phi_j}{\partial y}\frac{\partial\phi_i}{\partial y} \right) w d\Omega$	$\varepsilon\int_\Omega \left(\frac{\partial\phi_j}{\partial x}\frac{\partial\phi_i}{\partial x} + \frac{\partial\phi_j}{\partial y}\frac{\partial\phi_i}{\partial y} \right) w d\Omega$	$\varepsilon\int_\Omega \left(\frac{\partial\phi_j}{\partial x}\frac{\partial\phi_i}{\partial x} + \frac{\partial\phi_j}{\partial y}\frac{\partial\phi_i}{\partial y} \right) w d\Omega$
$B_{4,ij}$	0	$\frac{2}{\sqrt{t-\tau}}\int_\Omega q_L\phi_i\phi_j d\Omega$	$\frac{2}{\sqrt{t-\tau}}\int_\Omega q_L\phi_i\phi_j d\Omega$
$B_{5,ij}$	0	0	$\frac{2}{\sqrt{t-\tau}}\int_\Omega q_{cond}\phi_i\phi_j d\Omega$
C_i	0	0	$\frac{2}{\sqrt{t-\tau}}\int_\Omega \left(q_L \frac{T_{inj}}{T_{inj}-T_R} + q_{cond} \right)\phi_i d\Omega$

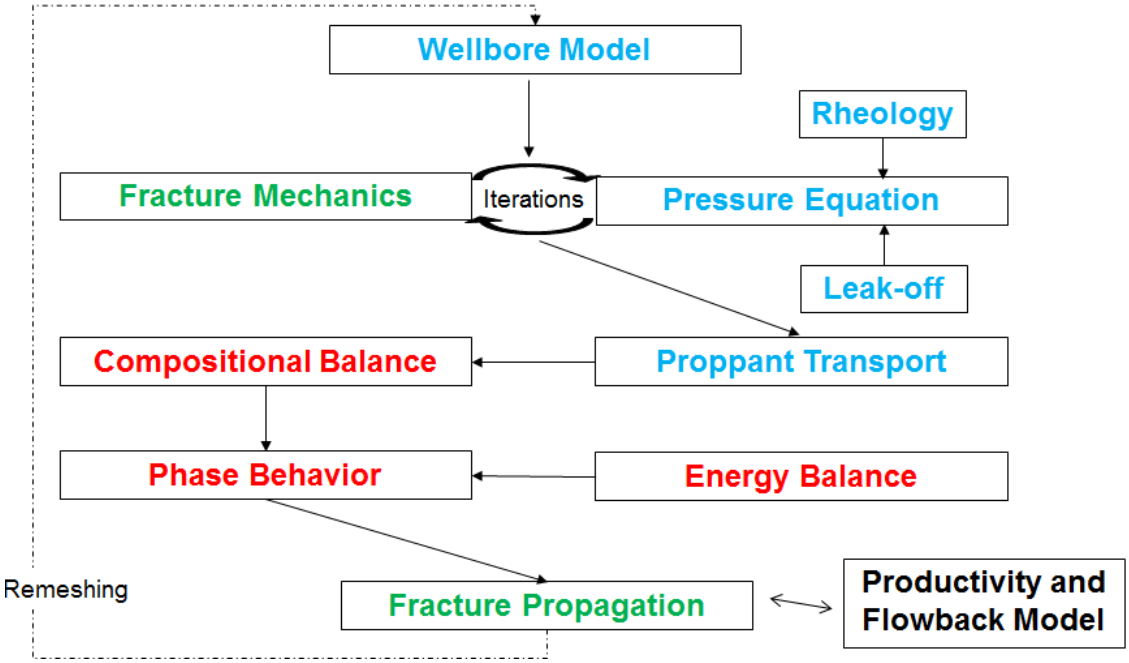

Figure 3.1: Simplified version of the main algorithm. The green color indicates equations that are used in conventional fracturing simulators; blue indicates equations that are modified to account for multi-phase compressible fluid flow; and red indicates equations that are not present in traditional fracturing models.

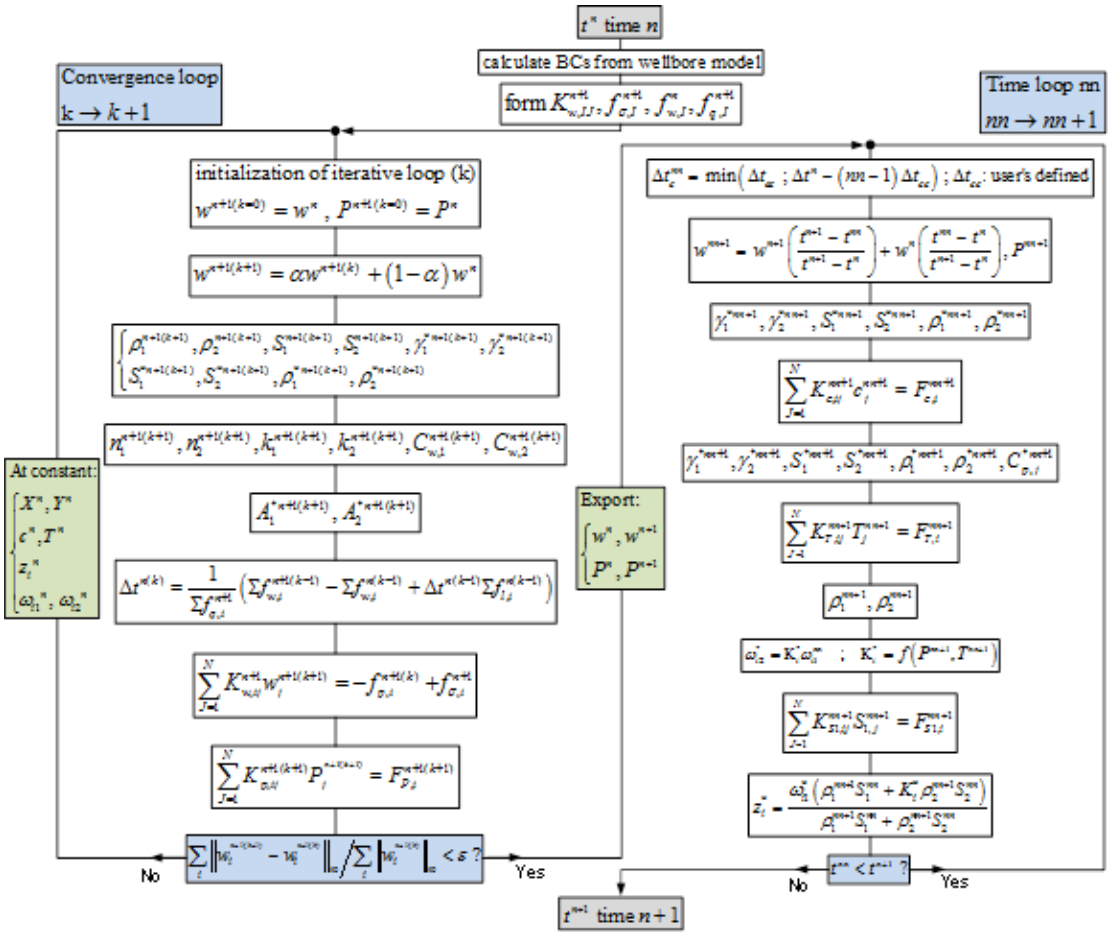

Figure 3.2: General structure of the algorithm implemented in *EFRAC-3D*. The left side shows the iterative process used to compute pressure and width for a calculated time step Δt^n. The right side shows the time-forward loop used to compute proppant concentration, fluid temperature, and fluid composition

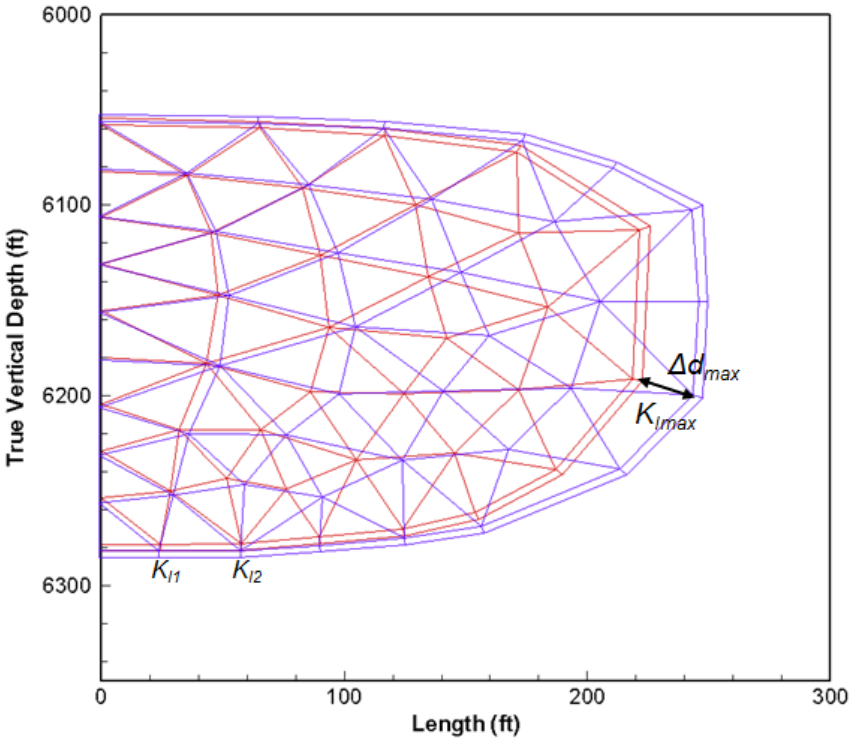

Figure 3.3: Fracture propagation scheme. The node with the maximum stress intensity factor (K_{Imax}) advances by a distance equal to the maximum front displacement (Δd_{max}). The motion of the other boundary nodes is governed by Eq. 3.37. The old fracture is indicated in red, and the new fracture is indicated in blue.

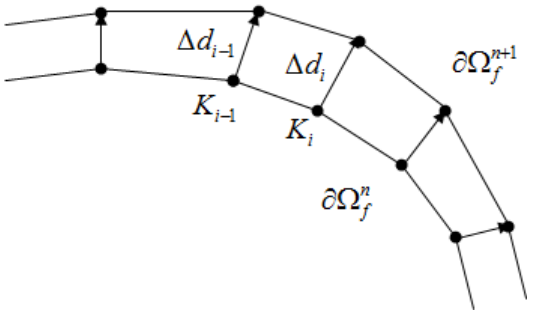

Figure 3.4: Movement of the boundary nodes between times t^n and t^{n+1}. Each node advances along its outward normal direction (adapted from Gu 1987).

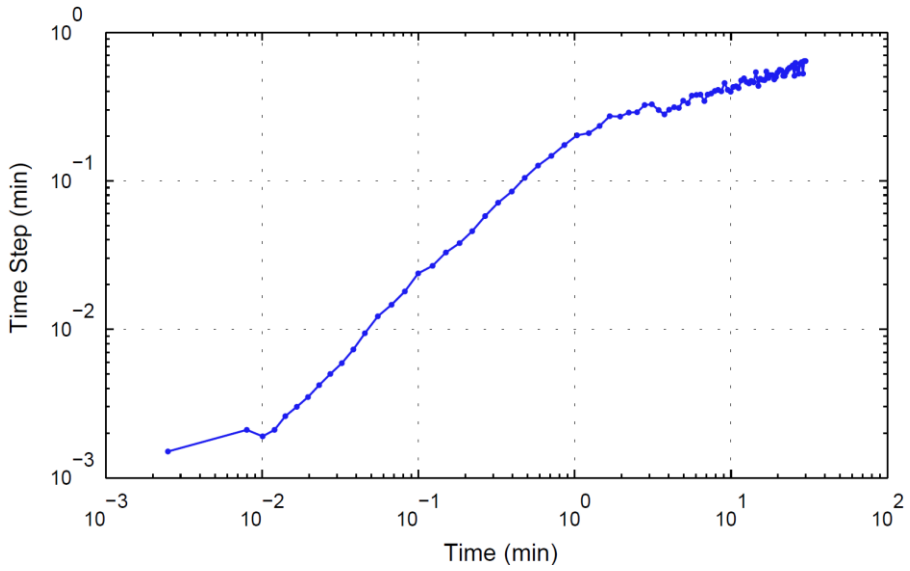

Figure 3.5: Example illustrating the evolution of the time step calculated from the compatibility condition.

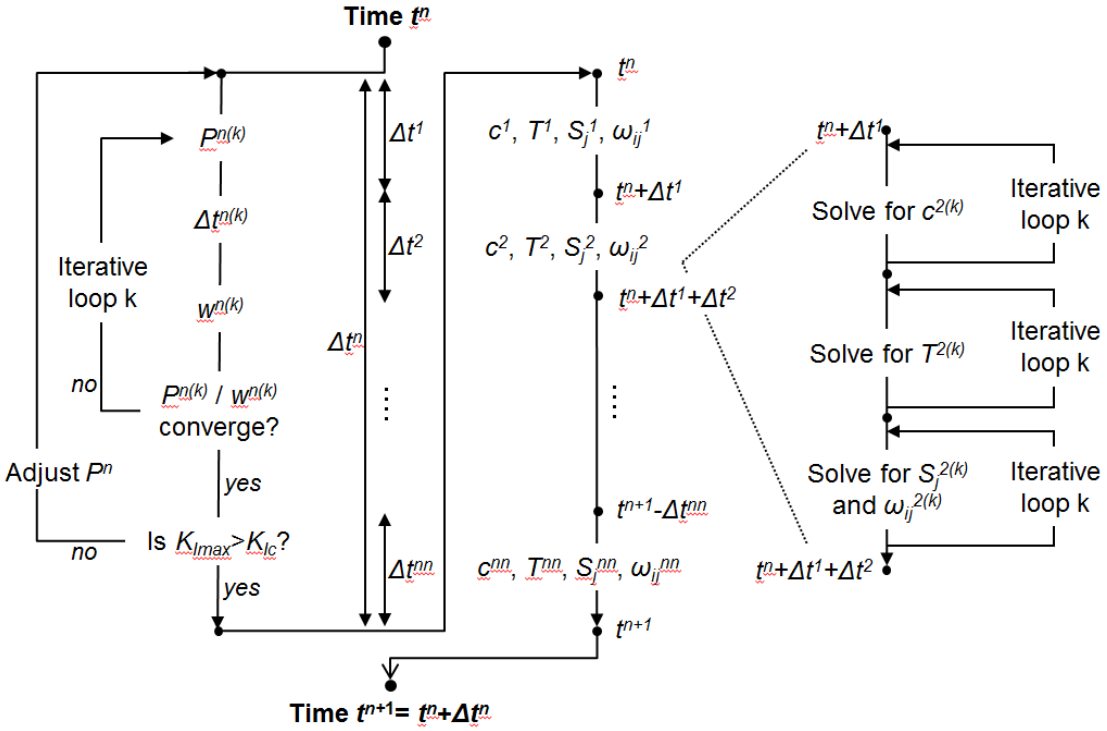

Figure 3.6: Time decoupling scheme. First, we compute fracture width and pressure using a relaxation iterative procedure. Then, we solve the transport equations using a time-forward loop and individual iterative schemes

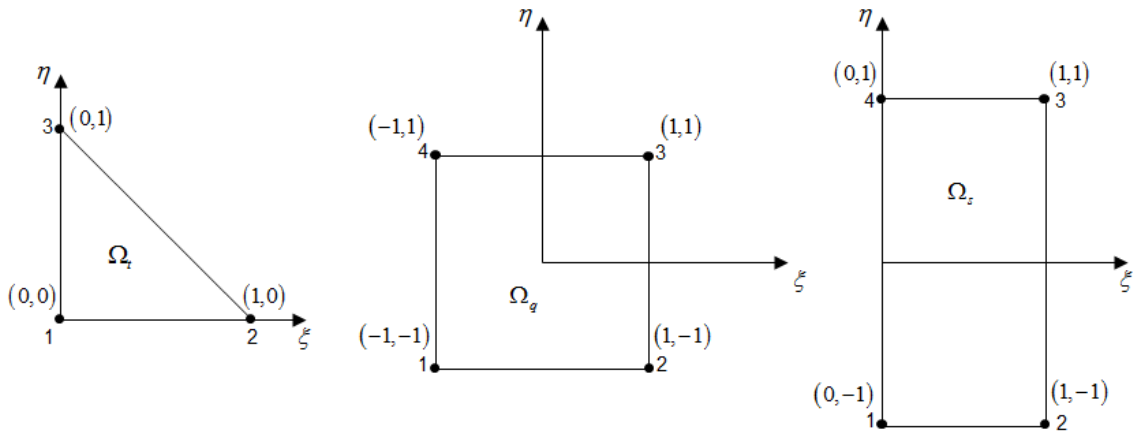

Figure 3.7: Master elements for the regular triangular (Ω_t), regular quadrilateral (Ω_q), and singular quadrilateral (Ω_s) elements.

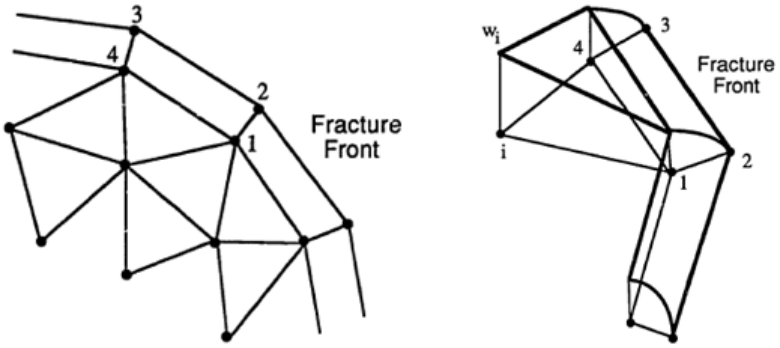

Figure 3.8: Node arrangement at the fracture tip. By construction, each pair of triangle and quadrilateral shares a side (from Gu 1987).

Nomenclature

A_{ij}, $B_{1,ij}$, C_i, F_i, K_{ij}, U_i = matrix coefficients at nodes i and j .
A_j^* = Intermediate variable defined in Eq. 3.9, $ft^5/(lbf\text{-}min)$
c = proppant concentration (volume fraction)
C_p = heat capacity, BTU/(lbm-°F)
C_w = leakoff coefficient, ft/√min
f = arbitrary function
g = gravity of earth, ft/s^2
G = shear modulus of the rock, psi
K_J = flow consistency index of slurry phase J, $lbm\text{-}min^n/ft^2$
$k_{ret,J}$ = retardation factor for slurry phase J in the horizontal direction
K_I = stress intensity factor, psi-√in
K_{IC} = fracture toughness, psi-√in
K_R = thermal conductivity of rock, BTU/(min-ft-°F)
K_γ = proppant split between two phases (γ_2/γ_1)
q_{cond} = conductive flux, ft/min
$q_{J,x}$ = flow rate per unit height of fluid phase J in the horizontal direction, ft^2/min
$q_{J,y}$ = flow rate per unit height of fluid phase J in the vertical direction, ft^2/min
$q^*_{J,x}$ = flow rate per unit height of slurry phase J in the horizontal direction, ft^2/min
$q^*_{J,y}$ = flow rate per unit height of slurry phase J in the vertical direction, ft^2/min
$q_{L,j}$ = fluid-loss flow rate per unit height of fluid phase J, ft/min
$q^*_{p,J,x}$ = flow rate per unit height of proppant in phase J in the horizontal direction, ft^2/min
$q^*_{p,J,y}$ = flow rate per unit height of proppant in phase J in the vertical direction, ft^2/min
m_{pumped} = mass rate imposed at the perforations, lbm/min
n = normal direction
n_J = flow behavior index of slurry phase J
NC = number of components
NP = number of phases
P = fluid pressure, psi
r = distance between the source and the field point in Eq. 3.34, ft
R = gas constant, ft-lbf/(lbm-°R)
S_J = saturation of fluid phase J
S_J^* = saturation of slurry phase J
t = time, min
T = fluid temperature, °F
T_D = dimensionless temperature
T_R = reservoir temperature, °F
u = unknown function
v = test function
w = fracture width, ft
x = horizontal location, ft
y = vertical location, ft

Subscripts

i = node i
I = component I
inj = BCs at the perforations
j = node j
J = phase J
N = order the of the Galerkin approximation
p = proppant
R = reservoir

Superscripts
k = iteration k
n = time step n
* = slurry property
$'$ = field point in Eq. 3.34

Greek Symbols
α, β, γ = coefficients in generic PDEs
α_r = relaxation parameter
γ_J = proppant concentration (volume fraction) in slurry phase J
Δd = displacement of the fracture front in the normal direction, ft
Δd_{max} = maximum displacement of the fracture front, ft
$\partial\Omega$ = boundary of the fracture domain
$\partial\Omega_c$ = non-perforated portion along the wellbore
$\partial\Omega_f$ = fracture front
$\partial\Omega_p$ = perforated interval along the wellbore
$\Delta m_{fracture}$ = change in fracturing fluid mass during Δt^n, lbm
$\Delta m_{leakoff}$ = mass of fluid that leaked off during Δt^n, lbm
Δt^n = time step increment, min
ε_D = diffusion coefficient in Eq. 3.24
ξ = coordinate in the master element
$\lambda_{J,x}$, $\lambda_{J,y}$ = retardation factor for proppant in phase J in the horizontal and vertical direction
η = coordinate in the master element
ϕ_N = basis function of order N
ρ_J = density of fluid phase J, lbm/ft^3
ρ_J^* = density of slurry phase J, lbm/ft^3
ρ_p = density of proppant, lbm/ft^3
ρ_R = density of reservoir rock, lbm/ft^3
ρ_T^* = density of slurry, lbm/ft^3
σ_{hmin} = *in-situ* minimum horizontal stress, psi
τ = retardation factor, min
ν = Poisson's ratio of the rock
ω_{IJ} = mass fraction of component I in phase J
Ω = fracture domain
Ω_q = regular quadrilateral master element
Ω_s = singular quadrilateral master element

Ω_t = regular triangular master element

References

Becker, E.B., Carey, G.F., and Oden, J.T. 1981, *Finite Elements: An Introduction*, Volume 1, Prentice-Hall, Inc., Englewood Cliffs, NJ.

Economides, M. and Nolte, K.G. 2000, *Reservoir Stimulation, Third Edition*, John Wiley and Sons, New York City, New York.

Gu, H. 1987. A Study of Propagation of Hydraulically Induced Fractures, Ph.D. Dissertation, The University of Texas at Austin, Austin, Texas (December 1987).

Kassir, M.K. and Sih, G.C. 1966. Three-Dimensional Stress Distribution Around an Elliptical Crack Under Arbitrary Loadings. *ASME J. Appl. Mech.* **33**: 601–611.

LAPACK, Linear Algebra PACKage, information available at www.netlib.org/lapack/.

Linkov, A.M. 2011. On Efficient Simulation of Hydraulic Fracturing in terms of particle Velocity. *Int. Journ. Eng. Sci*. **52**: 77-88.

Mastrojannis, E.N., Keer, L.M., and Mura, T. 1979. Stress Intensity Factor for a Plane Crack under Normal Pressure. *Int. J. Fracture* **15**: 247-258.

Ouyang, S. 1994. Propagation of Hydraulically Induced Fractures with Proppant Transport, Ph.D. Dissertation. The University of Texas at Austin, Austin, Texas (December 1987).

Renka, R.J. 1981. Triangulation and bivariate interpolation for irregularly distributed data points. Ph.D. Dissertation, The University of Texas at Austin, Austin, Texas (December 1981).

Ribeiro, L.H. and Sharma, M.M 2013. A New 3D Compositional Model for Hydraulic Fracturing with Energized Fluids. *SPE Prod & Oper* **28**(3): 259-267. SPE 159812-PA.

Yew, C.H. 1997, *Mechanics of Hydraulic Fracturing*, Gulf Publishing Company, Houston, Texas.

CHAPTER 4: WELLBORE AND PRODUCTIVITY MODELS

Fracturing fluid properties change not only inside the fracture, but also along the wellbore, as the fluid travels from the surface to the perforations. Operators regularly collect temperature and pressure data at the surface, but they rarely collect *in-situ* data. A wellbore model is thus required to estimate the variations in temperature and pressure along the wellbore. The wellbore model we implemented is very similar to the popular heat-transfer model proposed by Hasan and Kabir (1994, 2002, and 2012). Although variations in density and composition are negligible for traditional water-based fluids, changes in pressure and temperature affect the density and composition of compressible fluids. Heat transfers are usually amplified when we use energized fluids, as the gas component is injected at very low temperatures. Thus, a rigorous treatment of the wellbore calculations is critical when designing energized treatments.

Evaluating the performance of a fracture treatment is not about determining the final geometry of the fracture, but rather determining the associated hydrocarbon production; therefore, we developed a fractured well productivity model to assess fracture performance. It consists of a two-phase, pseudo 1D, fractured well productivity model. The fracture communicates with the reservoir via a 2D interpolation scheme that maps the properties of the unstructured grid into the Cartesian reservoir grid. The interpolation scheme constitutes the interface between the fracture and the reservoir; it monitors the amount of fluid invading the reservoir during pumping and shut-in, as well as the amount of fluid recovered during flowback.

The combination of the fracture, wellbore, and productivity models constitutes a design tool particularly suitable for designing and optimizing energized fracture treatments. This single modeling tool enables us to quantify the potential benefits of energizing the fracturing fluid.

4.1 TEMPERATURE VARIATION IN THE WELLBORE

An energy balance equation models the heat transfers occurring between the fracturing fluid and the reservoir. A rigorous treatment of heat transfers is important, as changes in temperature affect the fracturing fluid's composition, density, and rheology. Our model is very similar to the wellbore model proposed by Hasan and Kabir (1994, 2002, and 2012). We chose to use their model because of its simplicity, robustness, and popularity in the industry. The main features and derivations of the model are presented in this chapter.

4.1.1 Definition and Formulation of Heat Exchanges

The primary heat transfers are the heat conduction between the reservoir and the wellbore, and the forced convection that occurs as the fluid travels down the well. The heat conduction in the vertical direction is negligible compared to the heat transfer in the horizontal plane. This assumption reduces the heat conduction problem to a pseudo 1D

problem for each horizontal slice of the reservoir. The *undisturbed* reservoir temperature T_{ei} (also referred to as *far-field* temperature) is a known function of depth, so the heat conduction flux remains dependent on depth:

$$T_{ei}(z) = T_{ei}(TVD) = T_{es} + g_G \times TVD \tag{4.1}$$

Following the work of Ramey (1962) and Hasan and Kabir (1994), the surrounding earth is modeled as an infinite sink, and the wellbore is modeled as a line source of finite diameter. The heat diffusion per unit well depth (Q) between the well and the reservoir has the following expression, irrespective of the well configuration:

$$Q = \frac{2\pi k_R}{T_D}\left(T_{wb} - T_{ei}\right) \tag{4.2}$$

In Eq. 4.2, T_{wb} is the temperature of the interface between the well and the reservoir; T_{ei} is the undisturbed reservoir temperature; and T_D is a dimensionless function given by:

$$T_D = \ln\left(e^{-0.2t_D} + \left(1.5 - 0.3719e^{-t_D}\right)\sqrt{t_D}\right) \tag{4.3}$$

Eq. 4.3 expresses the cooling (heating) of the reservoir resulting from the heating (cooling) of the wellbore. The variable t_d is the dimensionless producing time:

$$t_D = \frac{4k_R}{\rho_e C_{p,R} {d_{wb}}^2} t \tag{4.4}$$

Even for steady-state heat transfers, the temperature of the reservoir in contact with the well is a function of time. As the reservoir heats the fracturing fluid, T_{wb} decreases, but the time dependence decreases over time, as seen on Eq. 4.3.

The heat exchanged by diffusion inside the reservoir is transferred radially from the outer layer of the wellbore to the fluid in the well. The heat transfer is given by:

$$Q = -\pi d_{to} U_{to}\left(T_f - T_{wb}\right) \tag{4.5}$$

U_{to} is an overall heat transfer coefficient (based on the outer tubing area) that represents the equivalent thermal resistance offered by the wellbore. As seen in Fig. 4.1, the equivalent resistance is the summation of the multiple resistances offered by the cement, casing wall, annulus, thermal insulation, and tubing wall. Because heat transfer is

dominant in the radial direction, we assume that the resistances are in a series; therefore, the overall heat-transfer coefficient is given by the following summation:

$$\frac{1}{U_{to}} = \frac{r_{to}}{r_{ti}h_t} + \frac{r_{to}\ln\left(r_{to}/r_{ti}\right)}{k_t} + \frac{r_{to}\ln\left(r_{ins}/r_{to}\right)}{k_{ins}} + \frac{r_{to}}{r_{ins}h_a} + \frac{r_{to}\ln\left(r_{caso}/r_{casi}\right)}{k_{cas}} + \frac{r_{to}\ln\left(r_{wb}/r_{caso}\right)}{k_{cem}} \tag{4.6}$$

If any part of the completion does not exist in a particular well configuration, the thermal resistance of that part is set to zero. The heat transfer coefficients for the natural convection in the annulus (h_a) and convection inside the tubing (h_t) are calculated from empirical correlations (Hasan and Kabir 2002).

The heat received by the fluid must equal that coming from the reservoir; therefore, the expression of the heat transfer coefficient is given by equating Eqs. 4.2 and 4.5:

$$Q = -L_R\left(T_f - T_{ei}\right) = -\frac{2\pi}{c_p m^{\bullet}}\left(\frac{r_{to}U_{to}k_R}{k_R + r_{to}U_{to}T_D}\right)\left(T_f - T_{ei}\right) \tag{4.7}$$

The parameter L_R defined in Eq. 4.7 is an overall heat transfer coefficient that depends on the thermal properties of both the wellbore and the rock formation.

4.1.2 Energy Balance Equation along the Wellbore

The temperature distribution is obtained from an energy balance equation for the fluid in the wellbore. Assuming that the heat transfers occur in a pseudo steady-state manner, the energy balance equation is given by:

$$\frac{dT_f}{dz} = -L_R\left(T_f - T_{ei}\right) + \frac{g\sin\alpha}{c_p} - \left(\frac{v}{c_p}\frac{dv}{dz} - C_{JT}\frac{dP}{dz}\right) \tag{4.8}$$

We assume that the kinetic energy (dv/dz) and Joule-Thompson (C_{JT}) effects are negligible; therefore Eq. 4.8 becomes:

$$\frac{dT_f}{dz} = -L_R\left(T_f - T_{ei}\right) + \frac{g\sin\alpha}{c_p} \tag{4.9}$$

We follow the work of Hasan and Kabir (2012) and represent the wellbore as a series of segments of constant diameter, as seen in Fig. 4.2. The parameter L_R is uniform for a

given well segment, and its time dependence is weak; hence, Eq. 5.9 is a first-order linear differential equation, which can be solved with the integrating factor method:

$$T_f = T_{ei} + \frac{1}{L_R}\left(1 - e^{L_R\left(z - z_j\right)}\right)\left(g_G \sin\alpha - \frac{g\sin\alpha}{c_p}\right) + e^{L_R\left(z - z_j\right)}\left(T_{fj} - T_{ei_j}\right) \tag{4.10}$$

In Eq. 4.10, T_{fj} is the local boundary condition that specifies that the temperature at the distance z_j is known. This expression is used to account for changes in wellbore inclination and diameter.

4.2 PRESSURE VARIATION IN THE WELLBORE

A rigorous treatment of fluid flow along the wellbore is important because energized fluids are compressible. The changes in pressure affect the fracturing fluid composition and density. Similarly to the temperature model, we chose to use the model proposed by Hasan and Kabir (2002) because of its simplicity, robustness, and popularity. The flow problem reduces to a pseudo 1D flow problem, in which the fluid properties are averaged along each cross-section of the wellbore.
The total pressure gradient is the sum of the hydrostatic head caused by the weight of the fluid, the frictional pressure drop, and the kinetic gradient:

$$\frac{dP}{dz} = \rho g - \left(\frac{dP}{dz}\right)_{fr} - \rho v \frac{dv}{dz} \tag{4.11}$$

In this study, we assume that the kinetic gradient (dv/dz) is negligible compared to the hydrostatic gradient and the frictional pressure drop. The hydrostatic head per unit of length is simply the density of the fluid multiplied by the gravitational constant. The frictional pressure drop is estimated from friction factor correlations or from actual pressure data measured along the wellbore.

For foams, we assume that the two-phase mixture remains stable; therefore, the velocity is the same for both phases, and the two-phase flow problem reduces to a pseudo single-phase flow problem. Because energized fluids are compressible, the density of the fluid is itself a function of pressure in Eq. 4.11. This effect is accounted for by updating the fluid density and composition at intermediate locations along the wellbore. We use a similar procedure to update fluid rheology along the well.

4.2.1 Frictional Loss

The frictional pressure loss depends on the rate of injection, fluid rheology, and tubing diameter. The pressure loss is usually estimated from empirical correlations that invoke

the Fanning friction factor (*f*), which is a function of the roughness of the pipe and the level of turbulence within fluid flow:

$$\left(\frac{dP}{dz}\right)_{fr} = \frac{2 f \rho v^2}{d_{ti}} \tag{4.12}$$

Many laboratory and field studies have been conducted to estimate the frictional pressure loss. In our model, three options are available:

- the frictional pressure gradient is prescribed by the user;
- the Fanning friction factor is prescribed by the user; or
- the Fanning friction factor is estimated from empirical correlations.

When field data are available, the user can directly prescribe the frictional pressure gradient per unit length for a given injection rate. This is the most accurate representation of the flow behavior inside the well. Similarly, the user can prescribe the value of the fanning friction coefficient when it is determined from carefully-controlled experiments. These formulations are particularly useful for history-matching purposes.

Often, the frictional pressure loss is unknown *a priori*, so empirical models are required to estimate it. The injection rates, viscosities, and tubing diameters used in fracturing typically result in turbulent flow at high Reynolds numbers (*Re*higher than 10^4). A common correlation for the friction factor under turbulent flow (Denn 1980) is given by:

$$f = \left(-1.737 \ln\left[0.269 \frac{\varepsilon}{d_{ti}} - \frac{2.185}{\mathrm{Re}} \ln\left(0.269 \frac{\varepsilon}{d_{ti}} + \frac{14.5}{\mathrm{Re}} \right) \right] \right)^{-2} \tag{4.13}$$

This correlation predicts unreasonably large pressure drops for most fracturing applications, as fracturing fluids usually contain friction-reducing polymers that have been known to cause a drag reduction. As shown by Virk (1975) and Denn (1980), long polymer molecules dampen flow instabilities and hence reduce the turbulent energy dissipation. For high Reynolds numbers, Denn (1980) proposed thefollowing friction factor correlation:

$$\begin{aligned} &\ln(f) = 28.135 + \left[-29.379 + \left(8.2405 - 0.86227 x_{\mathrm{Re}} \right) x_{\mathrm{Re}} \right] x_{\mathrm{Re}} \\ &\textit{where} \quad x_{\mathrm{Re}} = \ln\left[\ln\left(\mathrm{Re}_w \right) \right] \end{aligned} \tag{4.14}$$

In the oil industry, Valkó and Economides (1995) notably used Eq. 4.14 to account for the addition of gelling agents in fracturing fluids. The wall Reynolds number, Re_w, is used in Eq. 4.14 so the shear-thinning behavior of the fluid is taken into account. The wall Reynolds number is related to the general Reynolds number *Re* as follows:

$$\mathrm{Re}_w = \left(\frac{1+3n}{4n}\right)\mathrm{Re} \tag{4.15}$$

4.3 NEAR-WELLBORE FRICTIONAL LOSS

High near-wellbore friction losses have been observed in fracturing treatments, particularly in deviated wells or when the perforations are inadequate or poorly designed. The friction losses are attributed to several phenomena, such as poor wellbore communication through the perforations, tortuosity as the fracture turns and twists, and perforation phasing misalignment. A close study of fracture initiation and near-wellbore complexities requires the use of complex models, which are applicable only in a research environment under limited assumptions. These models are computationally intensive and generally require a specialist to obtain and interpret the results. One example of such a study was recently published by Alekseenko *et al.* (2013). Instead of conducting a comprehensive study of near-wellbore phenomena, we chose to use simple empirical correlations to account for near-wellbore pressure losses.

4.3.1 Perforation Frictional Loss

Improper perforating can result in near-wellbore screenouts if the perforations do not provide an adequate pathway between the wellbore and the fracture. The equation commonly used to calculate the perforation friction loss was proposed by McClain (1963):

$$\Delta P_{perf} = 0.2369\frac{\rho q^2}{d_{perf}^4 N^2 C_{disc}^2} \tag{4.16}$$

In Eq. 4.16, the fluid density ρ is in lbm/gal, the total flow rate q is in bpm; the perforation diameter d_{perf} is in inches; N is the number of active perforations contributing to fluid flow into the fracture; and C_{disc} is a dimensionless discharge coefficient. The form of Eq. 4.16 is based on the assumption that the perforations are short cylindrical tunnels of the same length and diameter. C_{disc} accounts for the effect of the perforation shape on the friction pressure; so this empirical coefficient provides some flexibility for matching field and experimental data.

When proppant is pumped at high flow rates, an erosion process alters the shape of the perforation, thereby reducing the friction loss through the eroded perforations (Crump and Conway 1988). As seen in Fig. 4.3, sand erosion increases the value of the discharge coefficient, which results in a decrease in the pressure drop:

$$C_{disc} = \min\left(0.56 + 1.65\times10^{-4} m_{sand,cum}; 0.95\right) \tag{4.17}$$

The erosion process reaches equilibrium after enough sand has been produced; therefore, Eq. 4.17 contains an upper limit for the value of C_{disc}.

Alternatively, we can use direct empirical correlations to assess the perforation friction loss. When properly calibrated, these empirical correlations are the most accurate representation of the fluid behavior through the perforations. This correlation is not limited by any assumption:

$$\Delta P_{perf} = a_{perf} q^{b_{perf}} \tag{4.18}$$

Eq. 4.18 is a more general representation of the problem, which encompasses the model formulation proposed by McClain (1963) when using:

$$a_{perf} = 0.2369 \frac{\rho}{d_{perf}^4 N^2 C_{disc}^2} \quad and \quad b_{perf} = 2 \tag{4.19}$$

The user has three options to estimate the perforation friction loss: using Eq. 4.16 with a constant value of C_{disc}, using Eqs. 4.16 and 4.17, or using Eq. 4.18.

4.3.2 Tortuosity Effects

The expression of the perforation friction loss given in Eq. 4.16 assumes that the fracture is properly aligned with the perforations along the wellbore. The friction loss increases when this is not the case, due to phase misalignment, tortuosity, or other near-wellbore phenomena. In this work, the effect of phase misalignment is not explicitly accounted for. Rather, it can be incorporated by decreasing the value of N in Eq. 4.16. N refers to the number of active perforations contributing to fluid flow into the fracture; therefore, if the perforations are misaligned with the fractures, the effective number of active perforations decreases.

Another phenomenon is the turning and twisting of the fracture near the perforations in deviated and horizontal wells (Fig. 4.4). In a vertical well, the contact between the fracture and the wellbore extends over several tens of feet, which constitutes a large pathway for the fluid. The flow communication is much more restrained in horizontal wells, as the contact between the fracture and the wellbore is about the size of the wellbore diameter. In a vertical well, the flow regime inside the fracture and near the wellbore is linear. In a horizontal well, the flow regime inside the fracture remains linear, but the flow regime converges toward radial flow near the wellbore. The consequence is an additional pressure drop. Mukherjee and Economides (1991) modeled this behavior as

a skin effect, referred to as *choke effect*. In their work, the dimensionless productivity index of a transverse fracture intersecting a horizontal well (J_{DH}) can be obtained from the productivity index of the corresponding fractured vertical well (J_{DV}) as follows:

$$J_{DH} = \frac{1}{\frac{1}{J_{DV}} + s_c} \quad ; \quad s_c = \frac{kh}{k_f w}\left[\ln\left(\frac{h}{2r_{wb}} - \frac{\pi}{2}\right)\right] \tag{4.1}$$

Alternatively, the impact of the different mechanisms responsible for increased friction loss near the wellbore may be accounted for by using Eq. 4.18 with an appropriate choice of coefficients. This is the method we recommend for deviated (and horizontal) wells. Indeed, the current model does not explicitly solve for the local twisting and turning of the fracture near the perforations (as illustrated in Fig. 4.4). For deviated wells, the well trajectory impacts the flow calculations inside the wellbore, but it does not explicitly impact the friction loss caused by the fracture tortuosity. As of now, this effect is accounted for by increasing the value of the friction drop using Eq. 4.18.

4.4 INTERPOLATION SCHEME BETWEEN FRACTURE AND RESERVOIR

The performance of the fracturing treatment depends on the interactions between the created fracture and the reservoir. Good communication is essential for the hydrocarbon to flow from the reservoir into the fracture. Thus far, all the computations have been performed inside the fracture using a dynamic unstructured mesh for the propagating fracture, thereby ignoring what happens inside the reservoir. On the other hand, a productivity model estimates the amount of hydrocarbon recovered from the stimulated portion of the reservoir by considering the fracture as a boundary condition for the reservoir. The link between the two approaches is the interpolation scheme presented in this section. The interpolation scheme connects the propagating reservoir and the static reservoir by mapping the dynamic unstructured mesh into a static Cartesian grid.

4.4.1 Algorithm for Interpolation

We developed an efficient algorithm to perform the interpolation between the fracture grid and the reservoir grid. Fig. 4.5 shows the main steps performed by the algorithm for an arbitrary fracture element T_{elem}. In Fig. 4.5, the smaller black points are the nodes of the reservoir grid. The spacing between the reservoir nodes in the *x*- and *y*- directions is a constant prescribed by the user. The three large black points refer to the vertices of the triangular element T_{elem}. The coordinates of these nodes are obtained as part of the solution of the moving-boundary fracturing problem; therefore, the orientation of the

triangle is unknown *a priori*. We use the following algorithm (also shown in Fig. 4.6) to perform the interpolation scheme over all the fracture elements:

1. Start an outer loop over all the fracture elements.
2. Identify the minimum and maximum along the *x*- and *y*- directions for a given element T_{elem}. In this example: $x_{min}=x_1$, $x_{max}=x_2$, $y_{min}=y_2$, and $y_{max}=y_3$.
3. Define the interval of reservoir nodes that encompasses T_{elem} (shown in red in Fig. 4.5). The corresponding indices are denoted by i_{min}, i_{max}, j_{min}, and j_{max}.
4. Start an inner loop over all the reservoir nodes inside this interval. We consider here node i_{node}.
5. Check whether node i_{node} has been used already. A given reservoir node can only belong to one fracture element at most; therefore, if this node has already been identified as part of an element, it is not considered for the following steps.
6. Test whether node i_{node} is strictly inside triangle T_{elem} using a 2D barycentric test referred to as *triangle inclusion test*. An additional test is performed to check if i_{node} lies along one of the triangle edges.
7. If the node is inside the triangle, perform a 2D barycentric interpolation using the values of the property of interest at the vertices of T_{elem}. These nodes, which are indicated by a blue circle in Fig. 4.5, are then discarded for the computations over the next fracture elements.
8. Stop the inner loop over the nodes contained in the interval defined in step 3.
9. Stop the outer loop over the fracture elements.

4.4.2 Barycentric Method

The 2D barycentric method is a simple test to determine if a given node belongs to a given triangle of arbitrary size and orientation. As shown in Fig. 4.5, we consider a node located at (x_p, y_p) and a triangle T_{elem} formed by three nodes of coordinates (x_1, y_1), (x_2, y_2), and (x_3, y_3). The node is inside the triangle if the node always lies on the same side of the vectors formed by the triangle edges. This is the case if the three quantities (t_{p1}, $t_{p2,}$ and t_{p3}) have the same sign:

$$\begin{cases} t_{p1} = (x_p - x_1)(y_2 - y_1) - (y_p - x_1)(x_2 - x_1) \\ t_{p2} = (x_p - x_2)(y_3 - y_2) - (y_p - x_2)(x_3 - x_2) \\ t_{p2} = (x_p - x_3)(y_1 - y_3) - (y_p - x_3)(x_1 - x_3) \end{cases} \tag{4.21}$$

If the node of coordinates (x_p,y_p) is inside the triangle T_{elem}, the interpolated value z_p at this node is given by:

$$z_p = \alpha_1 x_p + \alpha_2 y_p + \alpha_3$$

$$where \begin{cases} \alpha_0 = x_1 y_2 - x_2 y_1 + x_2 y_3 - x_3 y_2 + x_3 y_2 - x_1 y_3 \\ \alpha_1 = \dfrac{1}{\alpha_0}\left[z_1 (y_2 - y_3) + z_2 (y_3 - y_1) + z_3 (y_1 - y_2) \right] \\ \alpha_2 = \dfrac{1}{\alpha_0}\left[z_1 (x_3 - x_2) + z_2 (x_1 - x_3) + z_3 (x_2 - x_1) \right] \\ \alpha_3 = \dfrac{1}{\alpha_0}\left[z_1 (x_2 y_3 - x_3 y_2) + z_2 (x_3 y_1 - x_1 y_3) + z_3 (x_1 y_2 - x_2 y_1) \right] \end{cases} \tag{4.22}$$

4.5 PRODUCTIVITY MODEL FOR FRACTURED WELL

We use a two-phase, pseudo 1D, fractured well productivity model to assess the performance of the fracturing treatment (Ribeiro and Sharma 2013). Our model is almost identical to the model developed by Friehauf, Suri and Sharma (2010), and the reader may refer to their work for more details regarding the derivations of the model. Our formulation is different because the fracture height is not necessarily equal to the pay zone height. A height correction factor (h_c) is used to assess how much of the vertical section of the pay zone is actually covered by the fracture. The fluid and reservoir properties are averaged vertically for each location along the fracture. These assumptions make the model a pseudo 1D model; therefore, there is no cross-flow, and gravity effects are not accounted for inside the reservoir. These assumptions are too simplistic to evaluate a gravity-driven liquid unloading process (Agrawal and Sharma 2013). Nevertheless, the model provides valuable insight regarding the impact of the fracturing fluid on hydrocarbon production.

4.5.1 Formulation of the Productivity Model

Well productivity is typically represented by the productivity index (J), which is defined as the rate of production divided by the applied drawdown. The applied drawdown is the pressure difference between the initial reservoir pressure and the bottomhole flowing pressure. Using the electronic-hydraulic analogy, the productivity index equals the inverse of the total hydraulic resistance R_{tot}:

$$J = \frac{q}{\Delta P} = \frac{q}{P_e - P_{wf}} = \frac{1}{R_{tot}} \tag{4.23}$$

For comparison purposes, J may be normalized by a base productivity index. For example, we define the base productivity J_0 as the productivity of an unfractured, undamaged well in a circular drainage area. Assuming steady state flow of a single hydrocarbon phase, the ratio of the productivity index becomes:

$$\frac{J}{J_0} = \frac{q/\Delta P}{q_0/\Delta P} = \frac{2\mu \ln\left(r_e / r_w\right)}{\pi kh} \frac{1}{R_{tot}} \tag{4.24}$$

The total flow resistance R_{tot} is calculated from the combination of the flow resistances that constitute the circuit shown in Fig. 4.13. For reasons of symmetry, the reservoir is split into four quarters. The definition of each resistance and the algorithm used for combining the resistances for a constant-height 2D fracture are provided in Friehauf (2009) and Friehauf, Suri and Sharma (2010). We have modified their formulation to account for 3D fracture geometry. Fig. 4.13 only shows a horizontal slice of the reservoir, but the calculations are performed for multiple horizontal slices of the reservoir. Because we do not consider any cross-flow, the horizontal slices of the reservoir are merely superposed.

During flowback, we assume Darcy's law in both the reservoir and into the propped fracture, which is modeled as a channel of known permeability and width. Depending on the flow geometry, the flow is modeled as elliptical, radial, or linear, and a flow resistance is appropriately defined. R_{tot} is the sum of the outer resistance (R_{out}), which connects the outer boundary of the drainage zone to the inner ellipse, and the inner resistance (R_{in}), which accounts for the flow from the boundary of the inner ellipse to the fracture:

$$R_{tot} = R_{out} + R_{in} \tag{4.25}$$

The outer resistance is delimited by the constant pressure ellipse, which is the limit of the drainage area, and the inner ellipse that encloses the stimulated fracture region. The ellipse dimensions are calculated in a similar fashion to Prats (1961) and Suri and Sharma (2007). In the outer ellipse, fluid flow is not altered by the fracturing treatment; therefore, the flow resistance is given by:

$$R_{out} = \frac{1}{\bar{h}_c} \frac{2\mu}{\pi hk} \ln\left(\frac{a_2 + b_2}{a_1 + b_1}\right) \tag{4.26}$$

The distance a_1 is assumed to be slightly longer than the fracture length. The distance b_1 is a function of the dimensionless quantity a_{Prats}, which is defined in Eq. 4.27. A graphical representation of the inner equi-pressure boundary around the fractured well is shown in Fig. 4.14. As shown by Friehauf (2009), a_{prats} is the dominating factor in controlling the inner ellipse size b_1. The dimensions of the outer drainage ellipse are calculated by assuming a confocal ellipse around points x=-L and x=L, with an area equal

to the drainage area of the reservoir (A). The dimensions of the inner and outer ellipses are given by:

$$\begin{cases} b_1 = L\left(1+\varepsilon_{drained}\right) \\ a_1 = f\left(a_{prats}, b_1\right) \\ a_{prats} = \dfrac{\pi}{2}\dfrac{kL}{k_f w_{ave}} \end{cases} ; \quad \begin{cases} b_2 = \dfrac{\sqrt{2(\sqrt{\pi^2 L^4 + 4A^2} - \pi L^2)}}{2\sqrt{\pi}} \\ a_2 = \dfrac{A}{\pi(b_2)} \end{cases} \tag{4.27}$$

Within the inner ellipse, the fluid travels through three successive zones: (1) the virgin zone, which is at the initial reservoir conditions, (2) the invaded zone, in which the saturation and the relative permeability to gas (oil) depend on fluid leak-off, and (3) the fracture, in which the conductivity is a function of fracture width, proppant concentration, and fluid saturation. These three zones are represented in Fig. 4.13: $R_{el,i}$ refers to a resistance in the virgin zone; $R_{d,i}$ refers to a resistance in the invaded zone; and $R_{f,i}$ refers to a resistance along the fracture. The length of the virgin and invaded zones is itself a function of the amount of fluid leak-off. For calculations purposes, the inner ellipse ($b_{1,i}$), the fracture width (w_i), the fracture height (h_i), and the length of the invaded zone ($h_{leak,i}$) are divided into segments of length ΔX. The flow resistances in the inner ellipse are given by:

$$\begin{cases} \mathrm{R}_{el,0} = \dfrac{1}{\mathrm{h}_{c,i}}\dfrac{2\mu}{\pi kh}\left[\dfrac{k}{k_s}\ln\left(r_s / r_w\right) + \ln\left(b_{1,0} / r_s\right)\right] & ; \quad \mathrm{h}_{c,i} = \max\left(\dfrac{h_i}{h}, 1\right) \\ \mathrm{R}_{el,i} = \dfrac{1}{\mathrm{h}_{c,i}}\dfrac{\mu}{kh}\dfrac{\left(b_{1,i} - h_{leak,i}\right)}{\Delta X} & ; \quad \mathrm{R}_{el,t} = \dfrac{1}{\mathrm{h}_{c,i}}\dfrac{\mu}{kh}\dfrac{b_{1,t}}{\left(a_1 - L\right)} \\ \mathrm{R}_{d,i} = \dfrac{1}{\mathrm{h}_{c,i}}\dfrac{\mu}{kh}\dfrac{kh_{leak,i}}{k_d \Delta X} & ; \quad \mathrm{R}_{f,i} = \dfrac{1}{\mathrm{h}_{c,i}}\dfrac{\mu}{kh}\dfrac{2k\Delta X}{k_f w_i} \end{cases} \tag{4.28}$$

Using the circuit shown in Fig. 4.13, these resistances are combined to obtain the inner resistance through the stimulated zone. This is done numerically using the algorithm proposed by Friehauf, Suri, and Sharma (2010). The inner flow resistance is a series that takes the form of:

$$\frac{1}{R_{in}} = \frac{1}{R_{el,0}} + \frac{1}{R_{f,1} + \frac{1}{R_{f,2} + \frac{1}{R_{el,1} + R_{d,1}} + \frac{1}{R_{f,3} + \frac{1}{R_{el,2} + R_{d,2}} + \frac{1}{R_{f,4} + \frac{1}{R_{el,3} + R_{d,3}} + ...}}}}} \tag{4.29}$$

4.5.2 Properties of the Virgin Zone, Invaded Zone and Fracture

The flow properties in the virgin zone are known because the initial fluid distribution has not been altered. Along the fracture, the fracture model calculates the fracture width and proppant concentration at each location. We assume that the saturation of the hydrocarbon phase inside the fracture is constant and provided by the user; however, this assumption is not rigorous as the liquid unloading occurs over time and is not uniform in the fracture (Economides and Nolte 2000; Agrawal and Sharma 2013). A reservoir simulator coupled with the fracturing model would be required to model the unloading process over time. In this study, our intent was to formulate a standalone simulator that can estimate the fractured well productivity.

The flow properties in the invaded zone are altered by fluid leak-off. A damaged zone is formed when water leak-off occurs during the creation of the fracture. The zone may or may not cause significant damage to the fracture productivity based on the extent of leak-off and on the reservoir properties. For cases where the permeability and drawdown pressures are high, water is removed efficiently, and the flow is not significantly impeded by the damage zone. In cases with low permeability and low drawdown pressure, the damage remains significant because the viscous forces are not sufficient to overcome the capillary forces. The high-water saturation zone impedes hydrocarbon production by reducing the relative permeability to the hydrocarbon phase. This water-blocking effect is illustrated in Fig. 4.15. One of the motivations behind using energized fluids is precisely to eliminate (or reduce) the water-blocking effect, by limiting the amount of water placed in the formation.

We assume that the capillary force is the main force trapping the water, and that the relative permeability to gas (oil) is a function of the capillary properties of the rock and the drawdown pressure only. Any *a priori* model may be used to model the changes in permeability as a function of saturation. For illustration purposes, the Brooks and Corey models (1966) are used to calculate the capillary pressure and relative permeability to gas (oil) as a function of the phase saturations:

$$P_c = P_c^o (S_w^*)^{-1/b} \quad where \quad S_w^* = \frac{S_w - S_{wr}}{1 - S_{wr}} \tag{4.30}$$

$$\frac{k_d}{k} = k_{rnw} = k_{rnwo}(1-S)^n \quad where \quad S = \frac{S_w - S_{wr}}{1 - S_{wr} - S_{nwr}} \tag{4.31}$$

S_{wr} and S_{nwr} refer to the residual saturation of the wetting and non-wetting phases, respectively. Water is assumed to be the wetting phase, making the recovery of water by gas (oil) a drainage process. If the capillary pressure is much higher in the damaged zone than in the fracture (which is likely to be the case), the capillary pressure in the invaded zone is equal to the drawdown pressure across the invaded zone. Combining Eqs. 4.29 and 4.30, we can relate the effective permeability of the damaged zone (k_d) to the drawdown pressure (ΔP) as follows:

$$\frac{k_d}{k} = k_{rnwo}\left(1 - \frac{(1-S_{wr})\left(\frac{\Delta P}{P_c^o}\right)^{-b}}{1 - S_{nwr} - S_{wr}}\right)^n \tag{4.32}$$

The parameter P_c^0 defined in Eq. 4.30 is a measure of the capillary pressure at high wetting (typically water) saturation. If the region around the fracture is fully saturated with the wetting phase, P_c^0 represents the minimum drawdown that any wetting phase could be recovered from that region. If the drawdown is less than P_c^0, the water saturation will remain high, causing relative permeability damage that can permanently inhibit gas from flowing into the fracture. The value of P_c^0 can be estimated from field measurements, laboratory tests, or estimates based on the work of Leverett (1940):

$$\mathrm{P_c^0} = 0.42\sigma\cos\theta\sqrt{\frac{\phi}{k}} \tag{4.33}$$

4.5.3 Determination of the Invaded Zone Length

The length of the invading zone (h_{leak}) is unknown *a priori*. It depends on fluid invasion, applied drawdown and shut-in strategy, and reservoir petrophysical properties. During pumping, a fraction of the fracturing fluid leaks off into the reservoir. We use the interpolation scheme presented in Section 4.4 to track the cumulative mass distribution of each component that invades the reservoir. The mass (per unit area) of component *i* invading the reservoir during Δt^n is given by:

$$\left(\frac{\Delta m_{lk,i}}{\Delta X\,\Delta Y}\right)_{pumping}^{t^n\to t^n+\Delta t^n} = 4\left(\sqrt{t^n+\Delta t^n-\tau}-\sqrt{t^n-\tau}\right)\left(\rho_1 C_{w,1}x_i+\rho_2 C_{w,2}y_i\right) \quad ; \quad i=1...NC \qquad (4.34)$$

At the end of pumping, the operator can choose to flow back immediately or shut-in the well for a period of time. If the operator immediately flows back, the fracturing fluid left in the fracture at the end of pumping is recovered at the surface; therefore, the total amount of fluid invading the reservoir is equal to the time integral of Eq. 4.34. Alternatively, if the operator waits for an extended (infinite) time, the totality of the fracturing fluid left in the fracture at the end of pumping invades the formation, as the rock closes on the proppant. The additional mass (per unit area) of component *i* invading the reservoir for an extended shut-in is given by:

$$\left(\frac{\Delta m_{lk,i}}{\Delta X\,\Delta Y}\right)_{shutin}^{\infty} = w\frac{(1-c)}{(1-\phi_{frac})}\left(\rho_1 S_1 x_i+\rho_2 S_2 y_i\right) \quad ; \quad i=1...NC \qquad (4.35)$$

In practice, the shut-in is a finite period of time, so only a fraction of the fracturing fluid left in the fracture after pumping invades the formation during shut-in. This process is not modeled explicitly; rather, it is modeled by a simple parameter ε_{shutin}, which can be estimated from the amount of fracturing fluid immediately recovered when the well is brought back in production:

$$\left(\frac{\Delta m_{lk,i}}{\Delta X\,\Delta Y}\right)_{shutin} = \varepsilon_{shutin}\, w\frac{(1-c)}{(1-\phi_{frac})}\left(\rho_1 S_1 x_i+\rho_2 S_2 y_i\right) \quad ; \quad i=1...NC \qquad (4.36)$$

By definition, ε_{shutin} ranges between 0 and 1, where 0 is the immediate flowback case, and 1 is the extended (infinite) shut-in case.

Once we know the mass of each component placed into the reservoir, we can estimate the length of the invaded zone. To do so, we perform Flash calculations under the reservoir conditions to assess the composition and density of each phase in the invaded zone. Assuming a pseudo 1D piston-like displacement of the reservoir fluids by the fracturing fluid, we calculate the volume (per unit area) of each phase inside the reservoir. This volume is then converted to an invaded zone length (h_{leak}):

$$h_{leak} = \frac{m_{lk,1}/\rho_1}{\phi S_1 \Delta X\,\Delta Y} \qquad (4.37)$$

Based on the fractional flow curve and the initial fluid saturations in the reservoir, the value of h_{leak} and S_1 are corrected to agree with the rock petrophysical properties.

4.5.4 Comments Regarding Foams

The productivity model used to assess the performance of the fracturing treatment during flowback is a two-phase model that considers an aqueous phase and a hydrocarbon phase. Foams are themselves two-phase mixtures. They typically contain a water phase and a second phase that is miscible with hydrocarbons. During pumping, we assumed that foams remain stable along the wellbore and inside the fracture; therefore, they have been treated as pseudo single-phase fluids. During flowback, we consider, however, that foams break and split in two separate phases. This is primarily because of the filtration mechanism that occurs when the fracturing fluid invades the reservoir. As shown by Ribeiro and Sharma (2012), the filter cake created at the surface of the rock breaks the foam structure and allows for separate leak-off of each phase. Thus, we consider two separate phases in the reservoir and inside the fracture for the productivity calculations. Each phase can mix with a different fluid present in the reservoir. For instance, in the case of CO_2 foam invading a gas reservoir, the liquid (water-rich) phase mixes with connate water, while the gas (CO_2-rich) phase mixes with the hydrocarbon phase. The displacement of the two phases is no longer affected by the presence of the surfactant.

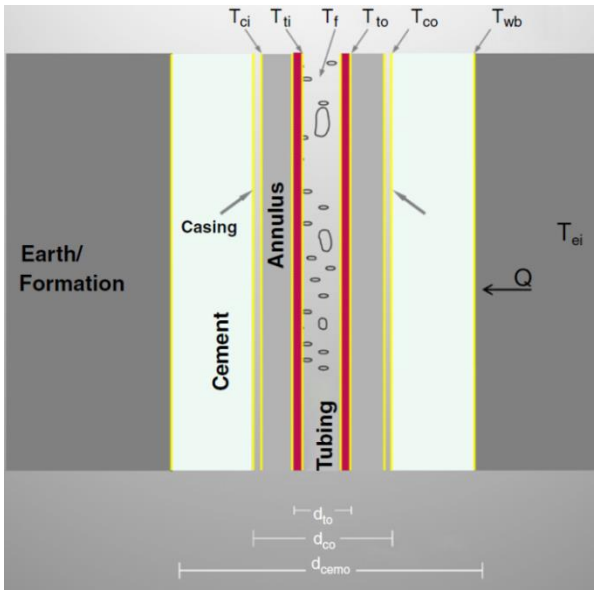

Figure 4.1: Wellbore configuration and heat flow through a series of resistances (from Hasan and Kabir 2012).

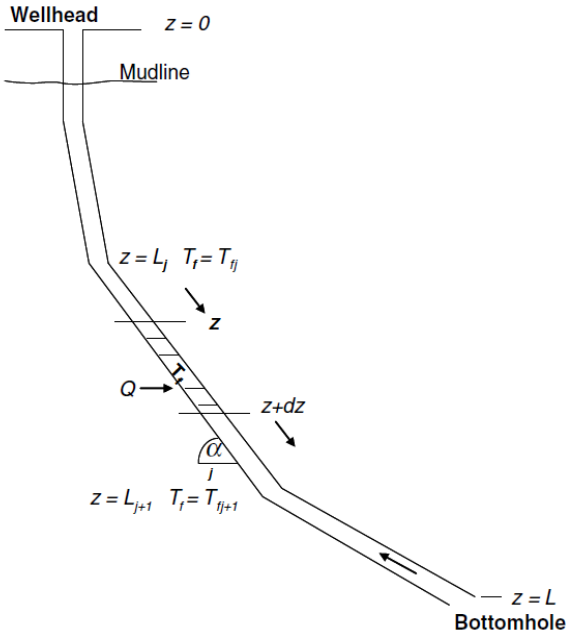

Figure 4.2: Well, made of segments of variable inclination and pipe diameter (from Hasan and Kabir 2012).

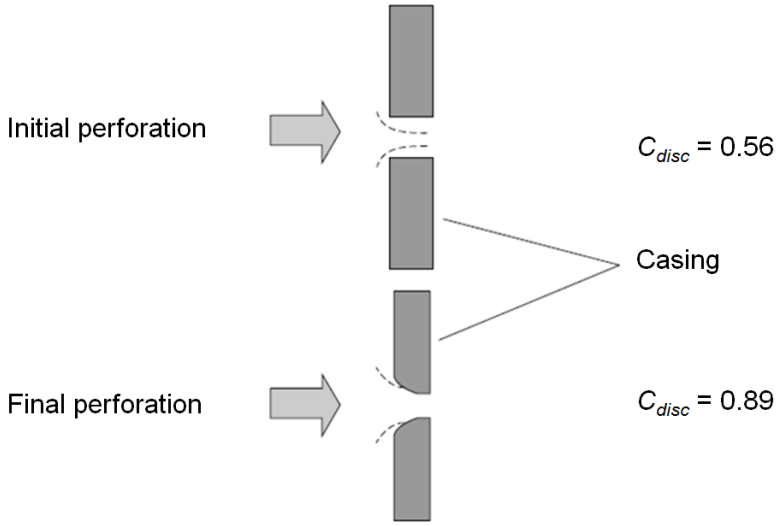

Figure 4.3: Evolution of the discharge coefficient due to sand erosion (from Crump and Conway 1988).

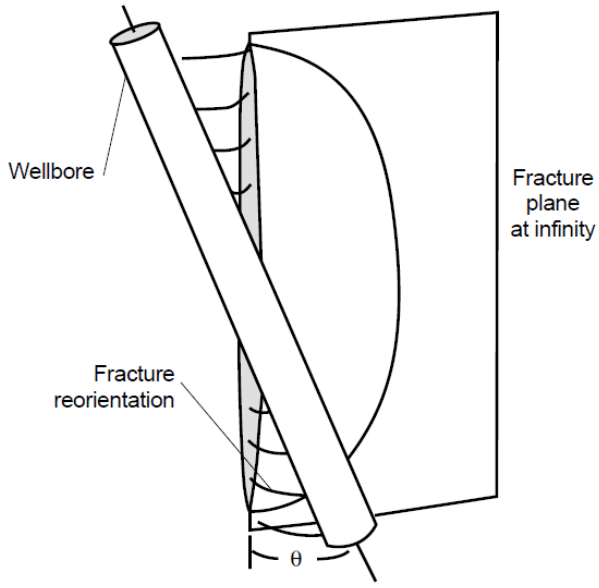

Figure 4.4: Tortuosity effect: the fracture twists and turns to align itself with the preferred direction of propagation (from Economides and Nolte 2000).

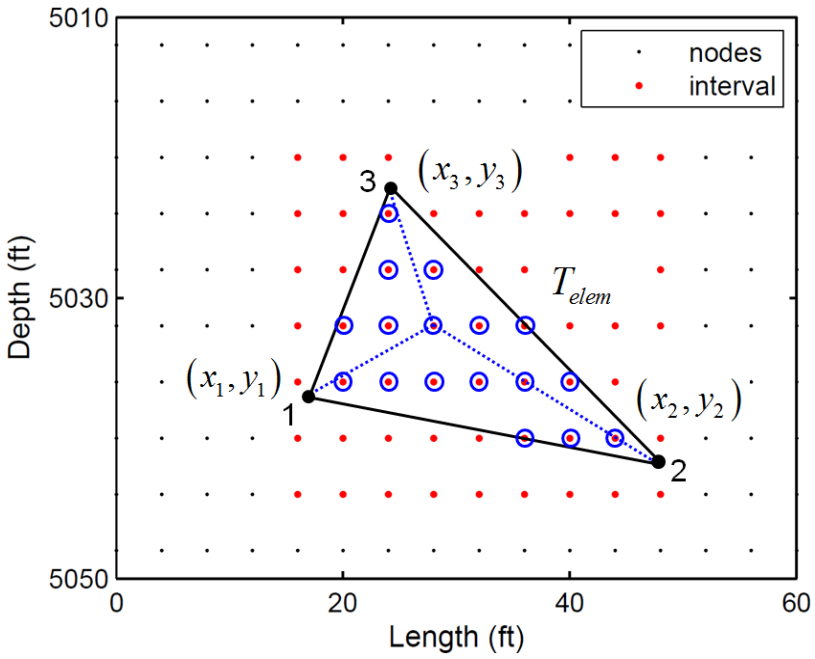

Figure 4.5: Interpolation scheme that relates the unstructured fracture grid to the Cartesian reservoir grid. Only the nodes indicated in blue are interpolated for this element.

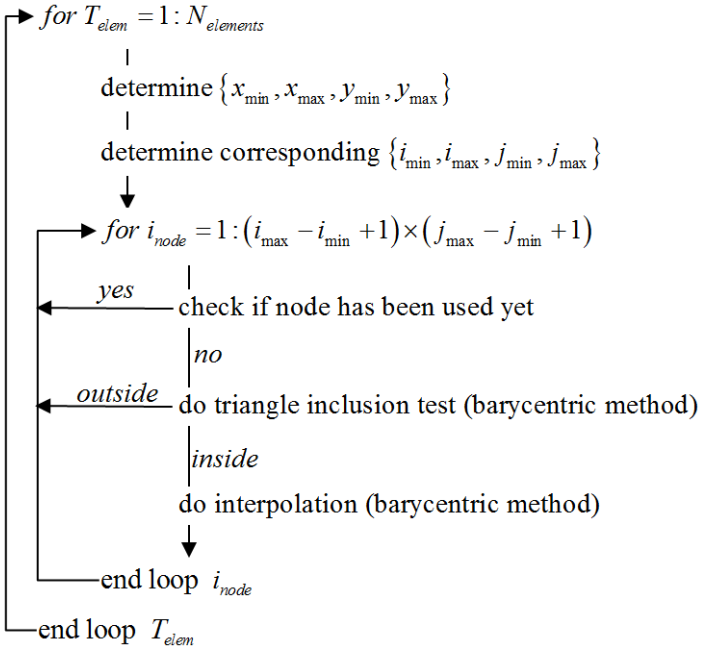

Figure 4.6: Algorithm used for the interpolation scheme.

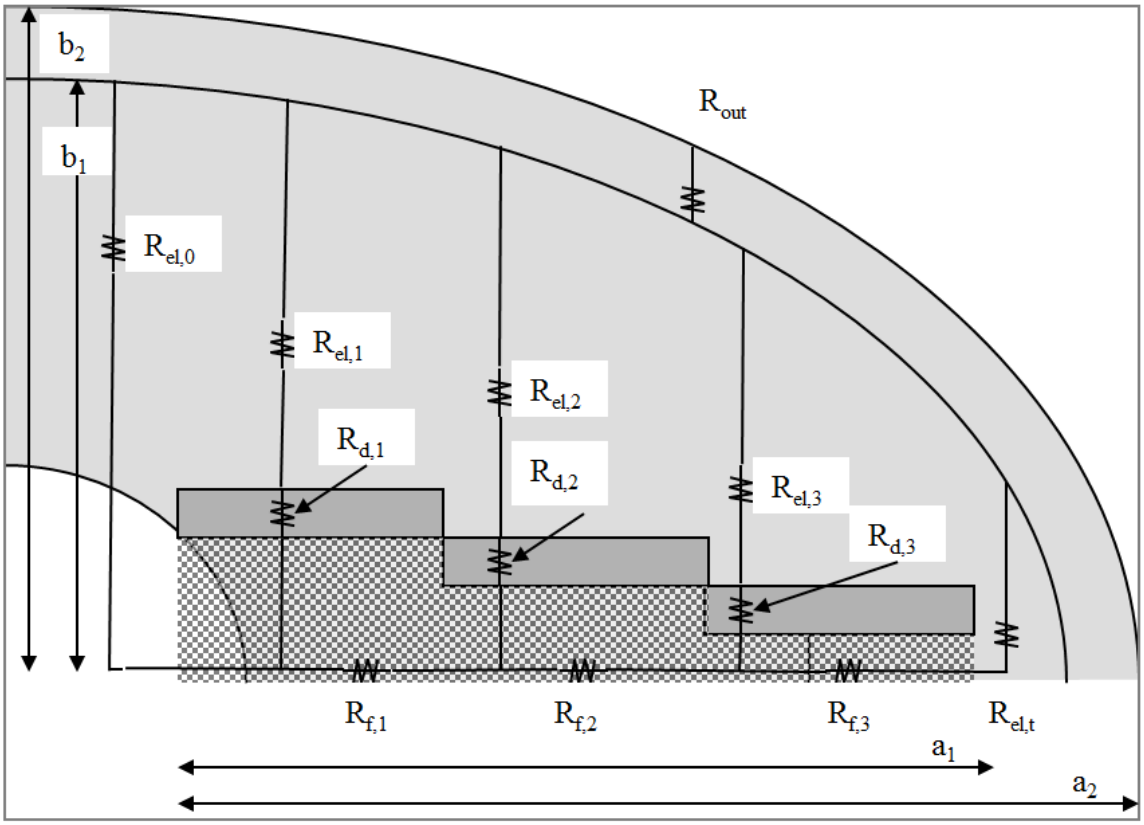

Figure 4.7: Association of flow resistances forming the productivity model (from Friehauf, Suri, and Sharma 2010). Because of the symmetry, only a quarter of the fractured well system is shown. R_{out} is the resistance in the outer ellipse; $R_{el,i}$ is a resistance in the virgin zone; $R_{d,i}$ is a resistance in the invaded zone; and $R_{f,i}$ is to a resistance along the fracture. The outer ellipse is delimited by a_2 and b_2; and the inner ellipse is delimited by a_1 and b_1.

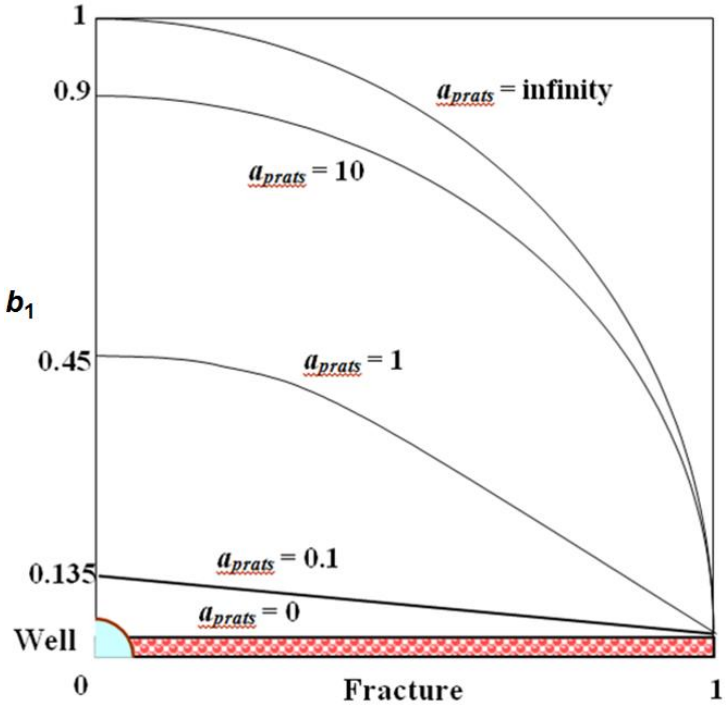

Figure 4.8: Inner ellipse minor axis versus a_{prats} conductivity (from Friehauf, Suri, and Sharma 2010).

NOMENCLATURE

a_1	= inner ellipse dimension parallel to the fracture, ft
a_2	= outer ellipse dimension parallel to the fracture, ft
a_{perf}	= empirical correction factor defined in Eq. 5.18
a_{prats}	= fracture conductivity defined by Prats (1961)
A	= drainage area, acre
b	= Brooks-Corey model for capillary pressure exponent
$b_{1,i}$	= inner ellipse dimension perpendicular to the fracture, ft
b_2	= outer ellipse dimension perpendicular to the fracture, ft
b_{perf}	= empirical correction factor defined in Eq. 5.18.
c	= proppant concentration (volume fraction)
C_{disc}	= discharge coefficient defined in Eq. 5.16
C_{JT}	= Joule-Thompson coefficient, °F/psi
C_p	= heat capacity, BTU/(lbm-°F)
$C_{w,j}$	= leakoff coefficient phase j, ft/√min
d_{perf}	= perforation diameter, in
d_{ti}	= inner tubing diameter, ft
d_{to}	= outside tubing diameter, ft
d_{wb}	= wellbore diameter, ft
f	= Fanning friction factor
g	= gravity of earth, ft/s^2
g_G	= geothermal gradient, °F/ft
h	= height of pay zone, ft

h_a = heat-transfer coefficient in annulus, BTU/min-ft^2-°F
$h_{c,i}$ = height correction factor
h_i = height of fracture, ft
$h_{leak,i}$ = lateral extent of damaged zone, ft
h_t = heat-transfer coefficient in tubing, BTU/min-ft^2-F°
J = productivity index, BPD/psi
J_0 = productivity index for unfractured, undamaged well, BPD/psi
J_{DH} = productivity index for transverse fractured well, BPD/psi
J_{DV} = productivity index for vertical well, BPD/psi
k = reservoir permeability, mD
k_{cas} = thermal conductivity of casing, BTU/min-ft-°F
k_{cem} = thermal conductivity of cement, BTU/min-ft-°F
k_d = damaged zone permeability (effective permeability of the producing phase i.e. oil/gas)
k_f = fracture permeability, mD
k_{ins} = thermal conductivity of insulation, BTU/min-ft-°F
k_R = thermal conductivity of reservoir, BTU/(min-ft-°F)
k_{rnw} = relative permeability of non-wetting phase
k_{rnw0} = endpoint relative permeability of non-wetting phase
k_s = permeability of (mechanical) damage around the wellbore, mD
k_t = thermal conductivity of tubing, BTU/min-ft-°F
L = fracture half-length, ft
L_R = coefficient defined in Eq. 4.7
$m\cdot$ = mass flux, lbm/ft
$m_{sand,cum}$ = cumulative mass of sand produced, lbm
n = flow behavior index in Eq. 4.15
n = Corey exponent in Eq. 4.31
N = number of open perforations
NC = number of components
P = fluid pressure, psi
P_c = capillary pressure, psi
P_c^0 = endpoint capillary pressure psi
P_e = outer boundary pressure, psi
P_{wf} = bottomhole flowing pressure, psi
q = flow rate, BPM
Q = thermal flux, BTU/min-ft
r_{casi} = inner casing radius, ft
r_{caso} = outside casing radius, ft
r_{ins} = insulation radius, ft
r_s = radius of (mechanical) damage around the wellbore, ft
r_{ti} = inner tubing radius, ft
r_{to} = outside tubing radius, ft
r_{wb} = wellbore radius, ft
Re = Reynolds number
Re_w = wall Reynolds number
$R_{d,i}$ = damage zone flow resistance
$R_{el,i}$ = virgin zone flow resistance
$R_{f,i}$ = fracture flow resistance
R_{in} = inner flow resistance
R_{out} = outer flow resistance
R_{tot} = total flow resistance
s_c = choke skin factor
S_J = saturation of fluid phase J
S_{nwr} = residual non-wetting phase saturation
S_w = wetting phase saturation
S_{wr} = residual wetting phase saturation
t = time, min
t_D = dimensionless producing time
t_{pi} = quantity defined in Eq. 4.21
T or T_f = fluid temperature, °F
T_D = dimensionless temperature
T_{ei} = undisturbed reservoir temperature, °F
T_{es} = surface reservoir temperature, °F
T_R = reservoir temperature, °F
T_{wb} = wellbore/reservoir interface temperature, °F
TVD = true vertical depth, ft
U_{to} = overall heat-transfer coefficient, BTU/min-ft^2-°F
v = fluid velocity, ft/min
w = fracture width, ft
w_{ave} = average fracture width, ft
x = horizontal location, ft

x_i = mass fraction of component i in the liquid phase
x_{Re} = coefficient defined in Eq. 4.14
y = vertical location, ft
y_i = mass fraction of component i in the gas phase
z = well depth, ft
z_p = extrapolated value in Eq. 4.22

Subscripts
i = segment i
p = proppant
R = reservoir
s = skin factor

Greek Symbols
α = well inclination from horizontal, deg
α_i = quantities defined in Eq. 4.22
$\Delta m_{lk,i}$ = mass of fluid component i that leaked off, lbm
Δt^n = time step, min
ΔP = drawdown pressure, psi
ΔP_{perf} = perforation friction loss, psi
Δt^n = time increment, min
ΔX = length of fracture segment, ft
ΔY = height of fracture segment, ft
ε = pipe roughness
$\varepsilon_{drained}$ = coefficient defined in Eq. 4.27
ε_{shutin} = coefficient defined in Eq. 4.36
μ = reservoir fluid viscosity, cp
ρ = density of fluid mixture in Eq. 4.16, lbm/gal
ρ_e = density of reservoir, lbm/ft^3
ρ_j = density of fluid phase j, lbm/ft^3
ϕ = reservoir porosity
ϕ_{frac} = fracture porosity
$\sigma cos\theta$ = interfacial tension, dynes/cm
τ = retardation factor, min
ω_{IJ} = mass fraction of component I in phase J

References

Agrawal, S. and Sharma, M.M 2013. Impact of Liquid Loading in Hydraulic Fractures on Well Productivity. Paper SPE 163837 presented at the SPE Hydraulic Fracturing Technology Conference, The Woodlands, Texas, 4-6 February.

Alekseenko, O.P., Potapenko, D.I., Cherny, S.G., Esipov, D.V., Kuranakov, D.S., and Lapin, V.N. 2013. 3D Modeling of Fracture Initiation From Perforated Non-cemented Wellbore. *SPE J.* (to be published). SPE 151585-PA.

Brooks, R.H. and Corey, A.T. 1966. Properties of Porous Media Affecting Fluid Flow. *J. Irrigation and Drainage Div., Proc. ASCE* **92**: 61-88.

Crump, J. and Conway, M. 1988. Effects of Perforation-Entry Friction on Bottomhole Treating Analysis. *J. Pet Tech* **40**(8): 1041-1048. SPE 15474-PA.

Denn, M.M. 1980, *Process Fluid Mechanics*, Prentice Hall, Englewood Cliffs, New Jersey.

Economides, M. and Nolte, K.G. 2000, *Reservoir Stimulation, Third Edition*, John Wiley and Sons, New York City, New York.

Friehauf, K.E. 2009. Simulation and Design of Energized Hydraulic Fractures. Ph.D. Dissertation, The University of Texas at Austin, Austin, Texas (August 2009).

Friehauf, K.E. and Sharma, M.M. 2009. A New Compositional Model for Hydraulic Fracturing With Energized Fluids. *SPE Prod & Oper* **24**(4): 562-572. SPE 115750-PA.

Friehauf, K.E., Suri, A., and Sharma, M.M. 2010. A Simple and Accurate Model for Well Productivity for Hydraulically Fractured Wells. *SPE Prod & Oper* **25**(4): 453-460. SPE 119264-PA.

Hasan, A. and Kabir, S. 1994. Aspects of heat Transfer During Two-Phase Flow in Wellbores. *SPE Prod & Fac* **9**(1): 12-16. SPE 22948-PA.

Hasan, A. and Kabir, S. 2002, *Fluid Flow and Heat Transfer in Wellbores*, Society of Petroleum Engineers, 2002.

Hasan, A. and Kabir, S. 2012. Wellbore Heat-Transfer Modeling and Applications. *J. Pet Sci. & Eng.* **86**: 127-136.

Leverett, M.C. 1940. Capillary Behavior in Porous Solids. *Trans. AIME* **142**(1): 152-169. SPE 941152-G.

McClain, C. 1963, *Fluid Flow in Pipes*, The Industrial press, New York City, New York.

Mukherjee, H. and Economides, M.J. 1991. A Parametric Comparison of Horizontal and Vertical Well Performance, *SPE Form Eval* **6**(2): 209-216. SPE 18303-PA.

Prats, M. 1961. Effect of Vertical Fractures on Reservoir Behavior – Incompressible Fluid Case. *SPE J.* **1**(2): 105-117. SPE 1575-G.

Ramey, H.J. 1962. Wellbore Heat Transmission. *J. Pet Tech* **14**(4): 427-435. *Trans. AIME* 225. SPE 96-PA.

Ribeiro, L.H. and Sharma, M.M. 2012. Multi-Phase Fluid-Loss Properties and Return Permeability of Energized Fracturing Fluids. *SPE Prod & Oper* **27**(3): 265-277. SPE 139622-PA.

Ribeiro, L.H. and Sharma, M.M 2013. Fluid Selection for Energized Fracture Treatments. Paper SPE 163867 presented at the SPE Hydraulic Fracturing Technology Conference, The Woodlands, Texas, 4-6 February.

Suri, A. and Sharma, M.M. 2007. A Model for Water Injection in Frac-Packed Wells. Paper SPE 110084 presented at the 2007 SPE Annual Technical Conference and Exhibition held in Anaheim, California. 11-14 November.

Valkó, P. and Economides, M.J. 1995, *Hydraulic Fracture Mechanics*, *First Edition*, John Wiley and Sons, New York City, New York.

Virk, P.S. 1975. Drag Reduction Fundamentals, *AIChE J.* **21**(4): 625-656.

CHAPTER 5: PHASE BEHAVIOR, RHEOLOGY AND LEAK-OFF OF ENERGIZED FLUIDS

The main advantage of the compositional fracturing model is to capture a more realistic representation of the fluid behavior, as opposed to the simplistic fluid characterization assumed in traditional fracturing models. The additional complexity of the compositional model enables us to model the unique properties of energized fluids; however, this modeling effort is futile if it is not supported by an accurate fluid characterization that is consistent with experimental data. Thus, the objective of this chapter is to review key fluid properties and provide meaningful data to the reader.

Foams exhibit unique properties that set them apart from traditional fluid formulations. Variations in pressure and temperature cause changes in fluid density and behavior, thereby impacting the fracture volume and the flowback performance. Foams experience dramatic changes in viscosity across different flow regimes, and the fracturing engineer can take advantage of this wide range of viscosities to optimize fluid design. Moreover, foams typically present superior fluid-loss control properties, and the reduction in liquid leak-off significantly bolsters oil and gas production.

5.1 PHASE DENSITY

Fluid density primarily affects fracture geometry, pump horsepower requirements, and proppant transport. Common additives do not modify fluid density because their concentration is too low; and they do not impact phase behavior because they are not chemically reactive. The density of water-based fracturing fluids is generally assumed to be constant, which is a reasonable assumption because the water density typically varies by less than 1% in most fracturing applications. For energized fluids, significant fluid expansion increases the fracture volume as temperature increases, but this effect is not captured by traditional isothermal fracturing simulators. The compositional model captures this effect; therefore, it requires the knowledge of fluid density as a function of temperature, pressure, and composition. The densities of the many fluid formulations encountered are well-documented, and we use empirical correlations to determine phase density.

Liquids:

For liquid-like fluids, thermal expansion (α_T) and isothermal compressibility (β_P) are taken into account.

$$\rho(P,T)=\rho_0(P_0,T_0)\times e^{\left[-\alpha_T(T-T_0)\right]}\times e^{\left[\beta_P(P-P_0)\right]} \tag{5.1}$$

The above equation is tuned so that the thermal expansion (α_T) and isothermal compressibility (β_P) are functions of pressure and temperature, respectively.

Gases:

For gas-like fluids, phase density can be calculated from the real gas equation of state, for which the compressibility factor is obtained from a mathematical fit of experimental data.

$$\rho(P,T)=\frac{M_w P}{Z(P_r,T_r)RT} \tag{5.2}$$

For the compressibility factor, the following correlations provide a simple and effective way to estimate fluid density:

$$z(P,T)=\alpha_1(T_r)+\alpha_2(T_r)P_r+\frac{\left(1-\alpha_1(T_r)\right)}{e^{\alpha_7(T_r,P_r)}}+\alpha_6(T_r)\left(\frac{P_r}{10}\right)^4$$

$$\begin{cases}\alpha_1=-0.101-0.36T_r+1.3868\sqrt{T_r-0.919}\\ \alpha_2=0.021+\dfrac{0.04275}{T_r-0.65}\\ \alpha_3=0.6222-0.224T_r\\ \alpha_4=\dfrac{0.0657}{T_r-0.86}-0.037\end{cases}\quad;\quad\begin{cases}\alpha_5=0.32\exp\left(-19.53(T_r-1)\right)\\ \alpha_6=0.122\exp\left(-11.3(T_r-1)\right)\\ \alpha_7=P_r\left(\alpha_3+\alpha_4\times P_r+\alpha_5\times P_r^4\right)\end{cases} \tag{5.3}$$

5.2 COMPONENT SOLUBILITY

For two-phase fluids, component solubility primarily affects the flowback performance of the fracture treatment. Because liquid leak-off is usually higher than gas leak-off, an energized component is more likely to invade the reservoir rock when that component is leaking off with the liquid phase. As the bottomhole pressure is decreased during flowback, the soluble component comes out of solution, thereby

increasing gas saturation. This phenomenon significantly facilitates the flow of the hydrocarbon fluids to the wellbore.

We use *K*-values to assess component solubility in two-phase fluids. For a given component, the *K*-value is a function of pressure and temperature. Fundamentally, the *K*-values express Henry's Law, which states that the solubility of a gas in a liquid is directly proportional to the partial pressure of the gas above the liquid. These *K*-values can be obtained from an empirical fit of solubility data, and we chose to use a Langmuir-type equation given below to fit the data. This choice was motivated by the fact that the solubility process is analogous to the adsorption of molecules on a solid surface, which was the process originally modeled by the Langmuir equation. The equation is bounded, which is necessary to represent the intrinsic limit of solubility. The solubility estimate ($x_{i,\,sol}$) is converted to the mass fraction of component *i* (x_i) in the liquid phase as follows:

$$x_{i,sol} = \beta(T)\frac{\alpha(T)P}{1+\alpha(T)P} \quad and \quad x_i = \frac{x_{i,sol}}{100 + x_{i,sol}} \tag{5.4}$$

5.3 RHEOLOGY

One of the most important considerations in fluid selection is viscosity, which impacts fracture geometry, fluid-loss control, and proppant transport. For non-energized fluids, fluid design primarily consists in selecting the optimum fluid rheology for a given reservoir. Depending on the nature of the reservoir, high viscosities may or may not be desirable. Viscous fluids tend to create wider and shorter fractures because the frictional loss dramatically increases in a narrow opening. The gelling agents and other viscosifying additives typically used in fracturing form a competent filter-cake on the fracture face, leading to a reduction in fluid leak-off. Increasing fluid viscosity also improves proppant placement by reducing proppant settling. For these reasons, the fluid rheology plays a critical role in fracturing.

5.3.1 Base Fluid Rheology

The rheology of water-based fluids is well documented, with numerous textbooks and monographs on the subject. Rheology primarily depends on the gelling agents and

fluid additives that are used. A large cocktail of additives is available, sometimes with major differences between the providers; therefore, few comprehensive models and/or databases describe the rheology of water-based fluids. Knowledge of the based-fluid rheology is necessary to assess the rheology of the two-phase mixture. For the experiments presented in this chapter, the base-fluid is a 30 lbm/Mgal linear Guar gel with 3% KCl per weight. If the base-fluid was different, the absolute values of viscosity would be different.

Rheological data for gelled CO_2 and LPG formulations are very scarce in the literature. Often, rheology data and protocols for gelling and mixing remain confidential. LPG is compatible with most of the common gelling agents, and the gelling process has been done routinely in the field. This is not the case for single-phase CO_2because of incompatibilities between the gelling agents and CO_2. In some cases, the alternative approach is to mix the CO_2 with another fluid that is easily gelled. In this study, we assume that the gelling process is efficient enough to increase the CO_2 or LPG viscosity. Without any additives, pure CO_2 and LPG are about three to five times less viscous than water under typical fracturing conditions; therefore, we will assume that gelled CO_2 and LPG remain less viscous than their gelled water counterparts.

5.3.2 Foam Rheology

Foam rheology is inherently dependent on foam stability, which results from the quasi-equilibrium between buoyancy and inertial forces (that favor gas bubble coalescence), and shear forces (that dynamically breaks the gas bubbles and mixes them with the internal phase). Unstable foams can be seen as mixtures of dissociated gas and liquid phases. The phases may travel at different velocities based on their intrinsic rheology. For stable foams, the two phases travel at the same velocity, so there is no slippage. Also, interfacial forces prevent gravity segregation. From a transport standpoint, stable foam is seen as a single "pseudophase" that contains gas bubbles and liquid together. For unstable foams, the interfacial forces are not capable of holding the gas bubbles inside the external liquid phase. As gas bubbles coalesce, the subsequent gas pocket migrates upward because of gravity segregation.

Foam rheology depends on both the rheology of the sole continuous liquid phase, and the interactions between the dispersed gas bubbles and the liquid phase. These interactions are related to the texture, or bubble-size distribution, of the foam.

A critical parameter for foam rheology is quality, which is defined as the volume fraction of the external phase (gas). At high qualities, interactions between bubbles cause energy dissipation resulting in a high effective viscosity. The internal phase remains stable until very high qualities are reached (~95%). Then, the gas becomes the external phase, and the mixture is referred to as a mist. At low qualities (typically lower than 50%), the interactions between bubbles are minimal, so the fluid viscosity resembles that of the base fluids. At low qualities, the fluid is typically referred to as a comingled fluid. These three flow regimes (i.e., comingled, foam, and mist) are indicated in Fig. 5.1. In practice, the transition between the regimes can be vague, and the scarcity of rheology data does not allow a proper characterization of the fluid behavior over a large spectrum. As seen in Fig. 5.1., multiple interpretations of the same data set are often possible.

Reidenbach *et al*. (1986) studied the rheology of foams under laminar and turbulent flow conditions. They described the rheology of N_2-hydroxypropyl guar (HPG) foam with a Herschel-Buckley model that depends on foam quality, gas type, and base-fluid rheology. The Herschel-Buckley model is a non-linear rheology model characterized by three parameters: the fluid consistency *K*, the flow index *n*, and the yield shear stress τ_0. The model relates the shear stress τ experienced by the fluid to the shear rate γ as:

$$\tau = \tau_0 + K\gamma^n \tag{5.5}$$

According to Reidenbach *et al.* (1986), the foam yield shear stress is only a function of quality for linear-gel-based foams. The yield stress significantly increases for qualities higher than 0.6, which is related to the large energy dissipation associated with the bubbles interactions at high foam qualities. Reidenbach *et al.* (1986) also assumed that the foam flow index equals the flow index of the liquid phase, and the consistency index is a function of quality and gel loading, as seen in Table 5.1 and equation below:

$$\begin{cases} \tau_{0,\,foam} = 0.07\Gamma \; if \; \Gamma \le 0.6 \\ \tau_{0,\,foam} = 0.0002e^{9\Gamma} if \; \Gamma > 0.6 \end{cases} \quad ; \quad n_{foam} = n_0 \quad ; \quad K_{foam} = K_0 \exp\left(C_1\Gamma + 0.75\Gamma^2\right) \tag{5.6}$$

The assumption that n remains constant has been challenged by Khade and Shah (2004), who claimed that the flow index n should decrease as the flow consistency K decreases:

$$\begin{cases} n_{foam} = n_0\left(1-2.1006\Gamma^{7.3003}\right) \\ K_{foam} = K_0\exp\left(-1.9913\Gamma+8.9722\Gamma^2\right) \end{cases} \quad for\ 20lbm/Mgal\ guar$$

$$\begin{cases} n_{foam} = n_0\left(1-0.1535\Gamma^{6.5152}\right) \\ K_{foam} = K_0\exp\left(-2.3761\Gamma+8.8830\Gamma^2\right) \end{cases} \quad for\ 30lbm/Mgal\ guar \qquad (5.7)$$

$$\begin{cases} n_{foam} = n_0\left(1-0.6633\Gamma^{5.168}\right) \\ K_{foam} = K_0\exp\left(-0.4891\Gamma+5.6203\Gamma^2\right) \end{cases} \quad for\ 40lbm/Mgal\ guar$$

The impact of proppant concentration on foam rheology is a topic open to discussion, as the literature of this subject is virtually nonexistent. The constant-internal-phase assumption assimilates the proppant as part of the internal phase. It considers volume fraction as the key variable for fluid flow, irrespective of the composition of the internal phase. This approach assumes that proppant settling is negligible and does not modify the flow pattern. An alternative approach is to consider that the foam has its own viscosity, and the addition of proppant modifies it, as this is typically assumed in single-phase slurry flow. The proppant effect on rheology is represented by an empirical correlation, such as:

$$\begin{cases} n_{prop} = n_{fluid}\exp\left(n_c\times c\right) \\ K_{prop} = K_{fluid}\exp\left(k_c\times c\right) \end{cases} \qquad (5.8)$$

For stable foams, n_{fluid} and K_{fluid} are the rheology parameters at a given foam quality. Additional experimental work is required to properly characterize the flow behavior of foam slurries.

5.4 MULTI-PHASE LEAK-OFF COEFFICIENTS

The rate of fluid leak-off is one of the most critical parameters involved in fracture design, as it directly impact production by affecting fracture geometry, fracture-

closure time, and proppant distribution. Fracture productivity is largely related to the amount of damaging fluid placed into the formation. If an operator overestimates leak-off, the pumping rate may be unnecessarily high and cause excessive pump pressures. Alternatively, an operator is likely to lower the pumping rate if he underestimates leak-off. In this case, the fracturing fluid may not be able to propagate large quantities of proppant. As the proppant accumulates and the frictional pressure drop surges near the perforations, a premature screenout may occur and cause a premature job termination. Although the importance of fluid leak-off is widely acknowledged by the industry, the understanding of multi-phase fluid-loss is very limited. This section identifies and explores the experimental challenges that must be overcome to gain a better understanding of the behavior of energized fluids.

5.4.1 Field Determination

Fluid leak-off is typically evaluated from a mini-frac (or leak-off) test, in which one injects a small volume of fluid at a pressure sufficient enough to initiate a fracture. Once the pressure breakdown is observed, the well is shut-in and the pressure response is monitored over time. The analysis of the pressure decline provides an average leak-off value that is representative of the region of the reservoir in contact with the fracture volume.

Data interpretation of leak-off tests with energized treatments is not trivial. Liquid and gas leak-off occur at different rates, but only one pressure response is available. The problem is ill-posed because we have two variables ($C_{w,l}$ and $C_{w,g}$) for only one equation (the pressure response). In addition, the pressure response is often measured from surface gauges, so the downhole pressure is obtained by estimating the weight of the fluid column in the wellbore. While this approach may be reasonable for incompressible fluids, the compressibility effects complicate the analysis of the pressure response in energized treatments.

For both non-energized and energized treatments, mini-frac tests have several shortcomings in unconventional formations. In shales, the matrix permeability is not necessarily the key parameter for fluid leak-off because leak-off primarily occurs through natural fractures. Mini-frac tests are short duration tests that span a small fraction of the reservoir, so the area of investigation is not likely representative of the reservoir. Thus, if the induced fracture does not interest any major fractures, the average leak-off will be underestimated, whereas it will be overestimated if the

induced fracture intersects an abnormally large number of natural fractures. Also, the timing is critical because the opening of pre-existing fractures may require a larger pressure than the one experienced during the mini-frac test. In this case, the leak-off is pressure-dependent and highly location-dependent; therefore, the use of a "Carter-type" leak-off model may lead to large discrepancies.

5.4.2 Experimental Determination

In the laboratory, the determination of dynamic multi-phase leak-off coefficients is challenging because it involves two experimental tasks that are not well understood by the industry: the generation of stable foams at high pressures, and the measurement of dynamic leak-off coefficients. These challenges have hindered the development of experimental studies on multi-phase leak-off.

5.4.3 Conclusions from In-House Experiments

Under all conditions, (Ribeiro and Sharma 2012) foams show superior fluid-loss control properties than linear gels, regardless of the foam quality. The different foam formulations (which contain a gelling agent in the liquid phase) built a competent filter-cake on top of the rock surface. The thick, polymer-rich, cake constitutes a low-permeability barrier that impedes the flow of gas and liquid. The ability of the foam to form a rapid wall-building filter-cake is critical in reducing the fluid-loss. There is a clear reduction in liquid leak-off as quality increases. This observation is intuitive because less liquid is used at higher foam qualities. Additionally, the invasion of gas into the porous medium reduces liquid invasion because of relative permeability effects. At qualities higher than about 60%, the gas leak-off seems to stabilize or to even decrease. This behavior might be explained by the fundamental change occurring within the fluid at the microscopic scale. At qualities above 50% or so, the interactions between gas bubbles become preponderant, thereby increasing the internal friction and the viscosity of the foam.

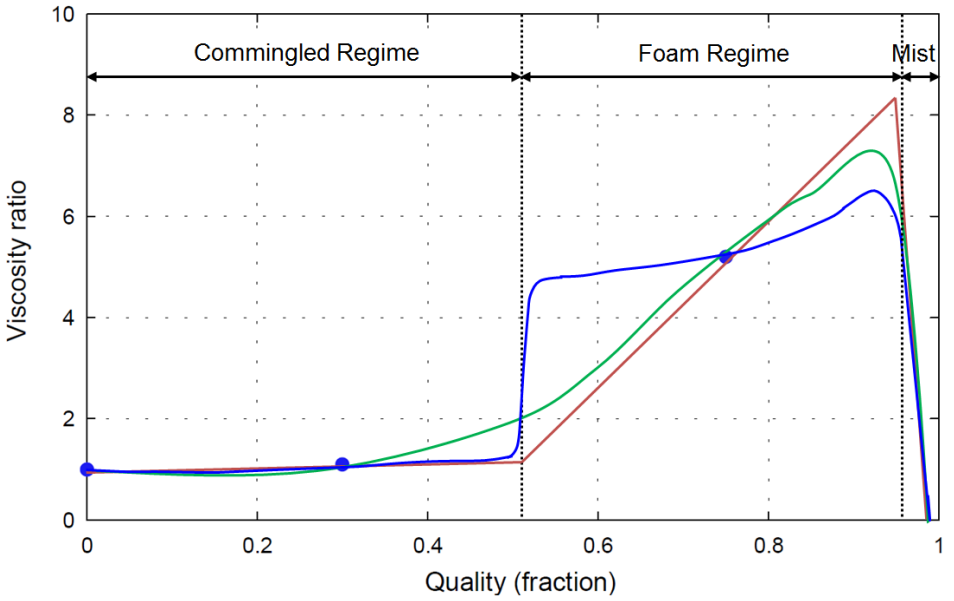

Figure 5.1: Illustration of the three flow regimes: commingled, foam, and mist. The transition between the regimes can be vague, and the scarcity of rheology data does not allow a proper characterization of the fluid behavior over a large spectrum. Often, multiple interpretations are possible because of the limited number of data points (indicated by the blue markers).

Table 5.1: Rheology correlation values for N_2 foams (from Reidenbach *et al*. 1986).

HPG Load (lbm/Mgal)	n (-)	K (lbf-sec^n/ft^2)	C_1 (-)
0	1	0.00002	3.6
10	0.75	0.0053	2.1
20	0.607	0.00256	1.7
40	0.45	0.0152	1.2

Nomenclature

$C_{w,g}$ = leakoff coefficient of the gas phase, ft/√min
$C_{w,l}$ = leakoff coefficient of the liquid phase, ft/√min
C_1 = coefficient defined in Table 5.1
k_c = coefficient in Eq. 5.8
K = flow consistency index, lbm-min^n/ft^2
K_{fluid} = flow consistency index of the clean fluid, lbm-min^n/ft^2
K_{foam} = flow consistency index, lbm-min^n/ft^2
K_{prop} = flow consistency index of the slurry, lbm-min^n/ft^2
K_0 = flow consistency index of the base-fluid, lbm-min^n/ft^2
M_w = molecular weight, atomic mass unit
n = flow behavior index
n_c = coefficient in Eq. 5.8
n_{fluid} = flow behavior index of the clean fluid
n_{foam} = flow behavior index
n_{prop} = flow behavior index of the slurry
n_0 = flow behavior index of the base-fluid
P = fluid pressure, psi
P_c = critical pressure, psi
P_r = reduced pressure (P/P_c)
P_0 = reference pressure, psi
R = gas constant, ft-lbf/(lbm-°R)
T = fluid temperature, °F
T_c = critical temperature, °F
T_r = reduced temperature (T/T_c)
T_0 = reference temperature, °F
x_i = mass fraction of component *i* in the liquid phase
$x_{i,sol}$ = solubility of component *i* in the liquid phase
Z = compressibility factor

Greek Symbols

α = Langmuir coefficient in Eq. 5.4
α_i = coefficients defined in Eq. 5.3
α_T = thermal expansion, 1/°F

β = Langmuir coefficient in Eq. 5.4
β_P = isothermal compressibility, 1/psi
γ = shear rate, s^{-1}
Γ = foam quality (volume fraction)
ρ = density, lbm/ft^3
ρ_0 = density of reference at (P_0, T_0), lbm/ft^3
τ = yield shear stress, lbf/ft^2
$\tau_{0,foam}$ = yield shear stress of foam, lbf/ft^2
τ_0 = yield shear stress of the base-fluid, lbf/ft^2

References

Khade, K. and Shah, S. 2004. New Rheological Correlations for Guar Foam Fluids. *SPE Prod & Fac* **19**(2): 77-85. SPE 88032-PA.

Reidenbach, V.G., Harris, P.C., Lee, Y.N, and Lord, D.L. 1986. Rheological Study of Foam Fracturing Fluids using Nitrogen and Carbon Dioxide. *SPE Prod Eng* **1**(1): 31-41. SPE 12026-PA.

Ribeiro, L.H. 2012. Multi-Phase Fluid-Loss Properties and Return Permeability of Energized Fracturing Fluids. Master's Report, The University of Texas at Austin, Austin, Texas (May 2012).

Ribeiro, L.H. and Sharma, M.M. 2012. Multi-Phase Fluid-Loss Properties and Return Permeability of Energized Fracturing Fluids. *SPE Prod & Oper* **27**(3): 265-277. SPE 139622-PA.

CHAPTER 6: DESIGN RECOMMENDATIONS

Although fluid selection should be evaluated on a case-by-case basis, several design recommendations can be made as follows:

1. If the fluid-induced damage is acceptable, water-based fluids constitute a simple and attractive solution. This is the case when the drawdown pressure is sufficient to recover the damaging fluid.
2. When water blocking severely impedes gas flow, the use of energized fluids improves clean-up and well productivity.
3. Reductions in relative permeability to gas (oil) by less than a factor of ten do not affect hydrocarbon production; therefore, low-quality foams often allow enough gas to invade the formation to limit the water blocking effect.
4. In depleted reservoirs, recovering any of the water lost to the formation is challenging because the drawdown pressure is limited. Alternatively, energized fluids experience a significant fluid expansion that improves fluid clean-up.
5. In under-saturated rocks, any water lost to the rock matrix remains trapped, thereby lowering the relative permeability to gas. When energized fluids are used, an extended shut-in can improve fluid clean-up by placing an additional amount of gas into the formation.
6. Non-aqueous fluids such as LPG and CO_2 are preferred in reservoirs that are prone to excessive fines migration and clay swelling. High-quality foams reduce the amount of water in contact with clays, although they do not eliminate clay swelling.
7. Fluids with higher solubility in the liquid phase have an increased ability to reduce damage in the invaded zone. Adding a component such as methanol increases the solubility of CO_2 in the liquid phase and alleviates fine migration and clay swelling in some sandstone reservoirs.
8. High-quality foams favor the propagation of short and wide fractures of high fracture conductivities, while low-quality foams promote the propagation of elongated fractures.
9. In many reservoirs, comingled fluids (30 to 50% quality) are optimum because they not only create long fractures with satisfactory proppant placement, but they also reduce the fluid-induced damage enough to ensure good flowback performance.
10. An extended shut-in is detrimental when damaging fluids are used because more liquid invades the rock formation. However, some of the proppant may be recovered when the fracturing fluid is flowed back immediately. If this is the case,

it is important to slowly bring the well back to production by carefully ramping-up the production rate.

The additional complexity of the compositional model enables us to model the unique properties of energized fluids; therefore, an accurate fluid characterization that is consistent with experimental data is critical for evaluating fluid performance. The following fluid properties have an impact:

1. *Density:* Under typical fracturing conditions, CO_2, LPG, and N_2 expand by more than 15% inside the fracture as the reservoir heats the fluid.
2. *Solubility:* Under typical fracturing conditions, the mass fraction of CO_2 in water is between 5% and 10%. The addition of methanol increases CO_2 solubility to more than 20% on a mass basis.
3. *Rheology:* Foams offer a wide range of viscosities without using excessive amounts of gelling agents and additives. At high shear rates, high-quality foams are dramatically more viscous than the base-fluid while low-quality foams have a viscosity similar to the base-fluid.
4. *Filter-cake:* Foams provide superior fluid-loss control without using excessive amounts of gelling agents. The filter-cake is supplemented by the presence of gas bubbles that reduce liquid-flow into the porous medium.
5. *Liquid leak-off*: Experimental work showed that low-quality foams were effective at reducing liquid leak-off (by at least a factor of three), and high-quality foams further reduced liquid invasion by a factor of two.
6. *Gas leak-off*: The gas phase leaks off into the reservoir. The ability of the gas to invade the reservoir has a critical effect on fracture design and well productivity.

Essentially, energized fluids offer properties similar to any water-based fluids in terms of fracture creation, proppant transport, and fracture conductivity, while also offering the advantage of limited fluid-induced damage as compared to water-based fluids. Nevertheless, the use of energized fluids typically requires larger capital expenditures, so it would only make sense to use these fluids when the profits associated with increased production outweigh the additional expenditures. The following safety and economic considerations play important roles in fluid selection:

1. *Safety hazards:* The use of gases requires additional safety measures because of their compressibility. High-pressure storage units are required, with numerous

instruments to prevent and monitor potential leaks. This is also true when using LPG because of its flammability and volatility.

2. *Operational considerations:* The use of gases such as N_2 and LPG may require pumping equipment with more horsepower because of the limited weight of the fluid column inside the wellbore. When using foams, care should be taken to avoid the formation of extremely-high-viscosity foams, which would halt pumping operations.
3. *Cost and availability:* In certain areas, the use of large quantities of gas is prohibitive because of the costs associated with the deployment of many trucks and pressurized storage units. Notably, this is the case in remote areas where there are no nearby gas power plants or pipelines.